Research and development of γ detectors for neutron scattering at electron Volt energies on VESUVIO spectrometer

by

Antonino Pietropaolo,

PhD Dissertation

Presented to the Physics Department

Universita' degli Studi di Roma "Tor Vergata"

for the Degree of

Doctor of Philosophy

15 December 2004

To my wife Manuela and my daugther Sofia

Acknowledgments

First of all I desire to acknowledge professor Carla Andreani.
She gave me the possibility, four years ago, to join her group, beginning an interesting and important activity on neutron detectors development. During these four years she fully enrolled me in the research activity of the group, under her constant and patient supervision. Her physical intuition and great experience in condensed matter physics have been a continuous stimulus and guide for my research activity.
Together with professor Andreani, I desire to greatly acknowledge professor Annalisa D'Angelo.
Her great experience and knowledge of particle detectors have been of great help in finding and understanding proper experimental strategies to employ during the experiments, while her interest and availability to scientific discussion have been very important to stimulate a thorough comprehension of particle detection techniques.
I desire to warmly acknowledge Dr. Roberto Senesi who, starting from the first day of work together, gave me his friendship and collaboration, transmitting his great professional skills and his deep knowledge on neutron instrumentation and scattering techniques, teaching me the basis of the VESUVIO′s data

analysis procedures.

A special thank is directed to Dr. Alessandra Filabozzi for great help and collaboration during Monte-Carlo simulations, suggestions for the development of a Fortran code for data fitting and for precious and interesting scientific discussions.

I desire to further acknowledge Dr. Marco Tardocchi, from the University of Milano-Bicocca, for his great help during the experiments on detectors in setting up the electronic chains and for important and stimulating discussions which have been of paramount importance in writing experimental papers together. Together with Marco my personal acknowledgement is directed to professor Giuseppe Gorini from Milano-Bicocca for precious indications and discussions during the experiments.

Last but not least, Dr. Nigel Rhodes and Dr. Erik Schooneveld of the ISIS detectors group, for their active, continuous, professional and friendly collaboration during all the experiments.

Antonino Pietropaolo

15 December 2004

Contents

Chapter 1

Introduction

The advent of the pulsed neutron sources has opened up new fields of investigation in condensed matter. In fact the intense fluxes of epithermal neutrons (above 500 meV) available at these facilities allow the achieving of energy, ω, and wavevector, q, transfers unaccessible to steady state reactors.

The investigation of condensed matter at small scales of time ($\leq 10^{-15}$ s) and distances (≤ 1 Å) is very attractive, as information on the single particle dynamics, namely momentum distribution $n(p)$ and mean kinetic energy $\langle E_K \rangle$, can directly be accessed [1,2]. Deep inelastic neutron scattering (DINS) technique is the more effective experimental tool for the direct determination of the single particle momentum distribution, through a measurement of the incoherent double differential scattering cross section [3, 4]. This quantity is directly and simply related, within the impulse approximation (IA) [1,5,6], to $n(p)$. The IA assumes that for high q values ($q \gg \frac{2\pi}{d}$, d being the nearest-neighbor of the probed sample) and high ω ($\omega \gg \omega_M$, being the maximum excitation energy of the system) the scattering process can be considered as occurring incoherently (each scattering center scatters independently from the

others) off freely recoiling masses (the neutron-scatterer interaction time is much shorter than the characteristics dynamical response time scale in the system). The DINS technique is similar (once the difference in nature of the interaction is accounted for) to hard X-ray scattering off electrons [7–10], high energy electron and nucleons scattering off nuclei [11–14], deep inelastic scattering (DIS) of leptons off nucleons [15,16], where the momentum distributions of the atomic electron, of the nucleons and of the partons are probed, respectively.

DINS regime is experimentally accessed if $\omega \geq 1$ eV and $q \geq 20$ Å^{-1}are achieved and the higher the energy and wavevector transfers, the higher is the degree of accuracy of the IA.

These kinematical constraints are effectively fulfilled by inverse geometry spectrometers operating at spallation sources.

On the other hand, epithermal neutrons allow access to the kinematical region of the (q, ω) space characterised by $\omega \geq 1$ eV and $q \leq 10$ Å^{-1}. This kinematical region defines the high energy inelastic neutron scattering (HINS) regime [17], which would allow experimental studies in areas such as the dispersion relations of high energy excitations in metals, semiconductors and insulators, high lying molecular rotational-vibrational states, molecular electronic excitations and the electronic level in solids [18–21]. In this case the only effective way to fulfill the HINS conditions is to use the inverse geometry configuration, detecting scattered neutrons well above 1 eV at small angles [22, 23]

Intense epithermal neutron fluxes are routinely exploited on the VESUVIO inverse geometry spectrometer, operating at ISIS spallation source, to perform DINS experiments on condensed matter, ranging from quantum systems [24–26] to molecular fluids and solids [27–29].

The experimental configuration employed on this instrument is known as Resonance Filter (RF) spectrometer and relies upon the use of metallic foils (analyser filters) of selected materials for final energy analysis, and ^{6}Li-glass scintillation detectors for neutron counting. The RF configuration has been employed on eVS [30], which pioneered the electron Volt neutron spectroscopy at ISIS since the mid 80$'$s, and it is still used as standard technique on VESUVIO as well [31].

A severe limitation to the employment of VESUVIO for HINS measurements is due to the $\frac{1}{v}$ dependence of the ^{6}Li neutron absorption cross section, v being the neutron velocity. As a matter of fact this characteristic determines heavy detection efficiency loss above 10-15 eV. Furthermore the original layout of the spectrometer allows to access reliably scattering angles higher than 15°.

This has motivated an important research and development activity on neutron detectors and instrumental components, in order to extend electron Volt neutron spectroscopy on VESUVIO to the HINS regime. For this purpose a modification of the original structure of VESUVIO was requested, incorporating the very low angle detector (VLAD) bank [32].

In order to perform neutron detection in the range 10-100 eV, the most effective configuration is the Resonance Detector (RD) spectrometer. In this set up metallic foils (analyser foils) of selected isotopes are coupled to γ detectors. In this way the final neutron energy analysis is performed by nuclear resonances, while neutron counting is provided by the detection of the prompt γ-ray cascade produced by (n, γ) resonance reactions in the analyser, with an efficiency almost independent from neutron energy.

The RD configuration was first proposed between the end of 1970$'$s and the beginning of 80$'$s [33–43]. First pilot experiments, performed with liquid and

solid scintillators [44] or high purity germanium (HpGe) detectors [41], despite showing the potential capabilities of the technique, have shown limitations mostly due to the background sensitivity of big scintillators and to the radiation damage effects in HpGe. Together with a series of explorative experiments, mostly devoted to the study of the detector performances, few interesting measurements on samples of some physical interest are reported in the literature [33, 37, 45]. Thus it can be concluded that the RD configuration has not routinely and systematically been employed for eV neutron spectroscopy, as it happened for the RF one [46–52].

The RD configuration has been revised on VESUVIO, employing different γ detectors (both scintillators and semiconductors) [53–65]. The aim of this experimental activity was to improve the RD performances, as compared to previous measurements, demonstrating its real capability in operating on inverse geometry time of flight spectrometers, reaching a higher efficiency and signal to background ratio with respect to the RF set up.

Beginning in the year 1999, within the European Union funded TECHNI project, and continuing on from 2002, within e.VERDI project, the RD configuration has been extensively tested on VESUVIO and has been demonstrated to be an effective technique for electron Volt neutron spectroscopy, so as to envisage its routine use for both DINS and HINS measurements on this spectrometer.

This dissertation aims to illustrate my research activity on detectors and instrument components development, carried out at the University of Rome Tor Vergata and in collaboration with the University of Milano-Bicocca and the Rutherford Appleton Laboratory.

The performed experimental work can be divided in different tasks, sum-

marised as follows:

- Recognition of suitable analysers for the RD configuration through a detailed study of their physical characteristics.

- Study of the physical characteristics of different γ detectors (scintillators and solid state) recognising the suitable ones for the RD configuration.

- Design, preparation and realisation of the first DINS experiment in the RD configuration on eVS spectrometer, on a Pb sample and a $^4He - H_2$ mixture:
  1- characterisation of the γ detector (a sodium iodide scintillator) with calibration sources;
  2- characterisation and optimisation of the detector$'$s electronics;
  3- choice of the analyser thickness for counting efficiency optimisation;
  4- choice of the overall experimental set-up;
  5- participation in the experiment, data analysis and upgrade of a Monte-Carlo code for the simulation of the DINS experiment with NaI(Tl).

- Design, preparation and realisation of the DINS experiments with Cadmium-Zinc-Telluride (CZT) semiconductor detectors:
  1- characterisation of the detectors with calibration sources;
  2- characterisation and optimisation of the detector$'$s electronics;
  3- participation in the experiment and data analysis;

- Design, preparation and realisation of biparametric measurements with CZT detectors:

1- characterisation of the electronics;

2- participation in the experiment and data analysis.

- Design, preparation and realisation of DINS and biparametric measurements with Yttrium-Aluminum-Perovskite (YAP) scintillators:
  1- characterisation of the detector$'$s electronics;
  2- participation in the experiment and data analysis.

- Data analysis of DINS measurements on liquid H_2O performed in the RD and RF configuration:
  1- development of a Fortran 77 code for data fitting employing a model independent approach.

- Participation in the design of the Very Low Angle Detector bank:
  1- study of feasibility;
  2- choice of the spectrometer$'$s configuration;
  3- choice of the proper detection system.

- Design, preparation and realisation of the first HINS measurement on VLAD prototype for the determination of the stretching mode energy density of states of polycrystalline Ice-Ih at 270 K.

As far as the results are concerned, DINS measurements demonstrated the effectiveness of the RD technique in accessing higher final neutron energies as compared to the RF one, and allowed for collecting useful indications to compare the efficiency and signal to background ratio achievable with the two

configurations.

The biparametric measurements made possible the background and the signal components recognition, finding experimental strategies for signal to background ratio improvement.

As interesting application of the RD configuration on VESUVIO spectrometer, the DINS experiment on a H_2O molecular system and the HINS measurement on polycrystalline Ice-Ih sample will also be discussed.

The DINS measurements, performed in both RD and RF configuration, provided an experimental determination of the proton momentum distribution in water and its mean kinetic energy. Furthermore, the employment of two different spectrometer$'$s set up allowed for a direct comparison of the obtained results. The RD experiment represents the first measurement of proton dynamics by means of this configuration, up to final neutron energies of about 70 eV.

The HINS experiment, devoted to the measurement of the O-H stretching mode density of states, aimed of demonstrating the feasibility of HINS on VESUVIO by testing the performances of the RD detection system on VLAD equipment. A comparison with a previous measurement of the same quantity on a direct geometry spectrometer will be briefly discussed. This will show the complementarity of the HINS on inverse geometry instruments with respect to inelastic neutron scattering on direct geometry spectrometers, in accessing higher ω values maintaining low q.

This experiment has to be considered as a benchmark for future measurements in a still unexplored region of the (q, ω) kinematical space. In fact the capability of the RD configuration to access final neutron energy well above 1 eV is a key issue in order to access higher ω and lower q values as compared to direct

geometry spectrometers, opening up new fields of investigation on condensed matter.

Chapter 2

Sources and instrumentation

2.1 Pulsed neutron sources

Intense pulsed neutron fluxes are mainly produced by means of both electrons and protons accelerated beams.

Electrons in a linear accelerator (LINAC) source, are emitted by a "gun" and injected into a LINAC which accelerates them up to energies in the order of 100 MeV. Then the electrons, packed into bunches, are directed toward a target material where they produce neutrons in a two-step electromagnetic process: 1) production of *bremsstrahlung* radiation [66], 2) photo-neutron ($\gamma - n$) production. The whole process is not highly efficient and only a few percent of the incident electrons give rise to a neutron. Furthermore few thousand of MeV of energy are dissipated for each neutron produced, with serious practical problems of heat removal.

In the proton-induced neutron production (spallation), negative hydrogen ions are accelerated in a LINAC up to several tens of MeV. Electrons are removed

Figure 2.1: Schematic of the ISIS spallation source at the Rutherford Appleton Laboratory (UK)

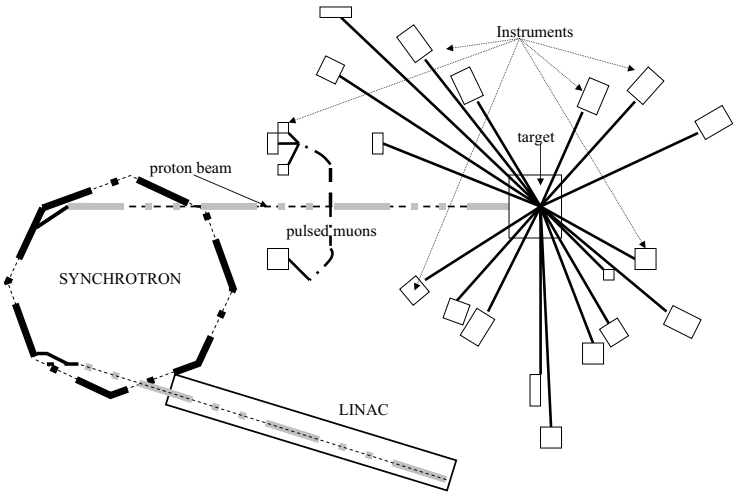

by a stripper, before injection into a synchrotron, and the protons are accelerated and packed into bunches with energy up to about 10^9 eV. The proton bunches are then directed in short bursts towards a target where neutrons are produced by spallation reactions, the neutron yield (*i.e.* the number or neutrons produced per proton) depending on proton energy and on the target material. Detailed description of the spallation reactions can be found in Refs. [67–73].

Figure 2.1 represents a schematic layout of the ISIS spallation source at the Rutherford Appleton Laboratory (RAL) in UK.

An ion source produces H^- ions at 17 keV energy. The ion beam kinetic energy is increased up to about 700 keV by means of a Cockroft-Walton accelerator before the injection in a LINAC, where they are further accelerated

up to 70 MeV. In the synchrotron the protons are then accelerated up to 800 MeV, with a bunch rate of 50 Hz. The neutron pulse produced by spallation is very short (typically few hundreds of nanoseconds) and peaked at high energy. A complex system of moderators, reflectors and coolers surround the spallation target (a set of thin tantalum sheets). The purpose of the moderators is to scatter the fast neutrons (1 MeV) from the target to slow them down to the energies required for the neutron instruments (typically between about 1 meV and 100 eV). By employing water moderators at room temperature, it is possible to obtain undermoderate neutrons in order to preserve the narrow pulse width and a high epithermal neutron flux. The presence of an intense epithermal tail in the energy spectrum is a key characteristics of pulsed neutron sources and is important for a series of experimental studies, as it will be briefly explained later.

All around the target station there are neutrons beam lines (see Fig. 2.1) feeding different instruments (spectrometers and diffractometers) where neutron scattering is employed for both structural and dynamical investigations on condensed matter systems.

In addition to neutron production, ISIS is the world's most intense source of pulsed muons for condensed matter research. Muon spectrometers are used to perform muon spin rotation, relaxation and resonance (μSR) experiments.

The pulsed nature of the source allows for using the time of flight (henceforth called TOF) technique for the kinematic reconstruction of the scattering process (*i.e.* to define energy and wavevector transfer). In the following section a brief description of the TOF technique is presented.

Figure 2.2: Schematic of an instrument: L_0 is the primary flight path (moderator-sample distance), L_1 is the secondary flight path (sample-detector distance). The t_{start} and, t_{stop} are provided by the proton beam monitor and the detector, respectively.

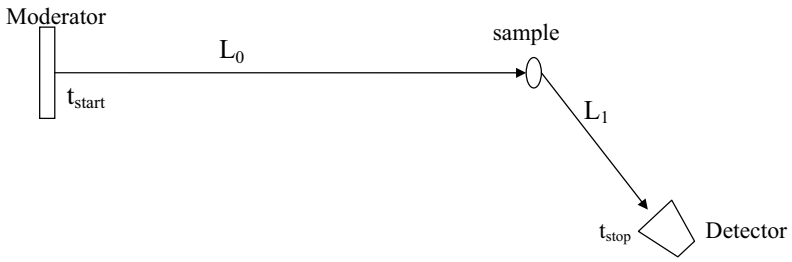

2.2 Basic principles of the time-of-flight technique

The total neutron TOF t is the time a neutron takes to travel from the moderator to the detector. It can be written as:

$$t = t_0 + \frac{L_0}{v_0} + \frac{L_1}{v_1} \tag{2.1}$$

where t_0 is a fixed electronic time delay, L_0 and L_1 are the incident and scattering flight paths of the instrument, while v_0 and v_1 are the initial and final neutron energy, respectively. Figure 2.2 represents a schematic drawing of an instrument, where the geometrical parameters are clearly indicated. TOF technique requires the knowledge of L_0, L_1, the scattering angle ϑ and of the initial or the final neutron energy (E_0 or E_1) to reconstruct the kinematic of the scattering process. By knowing the initial (final) energy, the total neutron TOF allows for the measurement of the final (initial) one, while the detector$'$s

angular position (ϑ) allows for the determination of the wavevector transfer, q, as it will be briefly explained in the next section.

The TOF acquisition chain can briefly be described as follows: before the proton bunch impinges on the heavy metal spallation target, a proton beam monitor, placed close to the target, triggers the opening of a time gate ($t = t_{start} = 0$) of fixed duration $\Delta t \simeq 20$ ms. During Δt the acquisition electronics of an instrument is enabled to process the electric signals provided by neutron detection system (neutron counters). Each signal is stored in a time channel of a Time to Digital Converter (TDC), its value being the time difference between the initial time of the gate t_{start} (approximatively corresponding to the instant the neutron leaves the moderator) and the detection instant (t_{stop}). A fixed time delay t_0 (see eq. 2.1) of about 5 μs is electronically provided, allowing for the recovery of the detectors of all instruments from the saturation induced by the "γ-flash", produced in the spallation process.

A more detailed description of the data acquisition electronic will be presented in Chapter 3.

2.3 Direct and inverse geometry inelastic spectrometers

To reconstruct the kinematics in an inelastic scattering measurement, the initial and final neutron energies (wavevector) have to be calculated. The wavevector, q, and energy transfer, ω, can be then calculated imposing wavevector and energy conservation:

$$\overrightarrow{q} = \overrightarrow{k_0} - \overrightarrow{k_1} \tag{2.2}$$

$$\omega = \frac{\hbar^2}{2m}(k_0^2 - k_1^2) = E_0 - E_1 \tag{2.3}$$

k_0 and k_1 being the initial and final neutron wavevectors, and m the neutron mass, respectively. The conservation laws apply rather stringent limitations to the values of q and ω which may be observed. The relation linking q and ω can be found starting from the relation:

$$q^2 = k_0^2 + k_1^2 - 2k_0k_1cos\vartheta \tag{2.4}$$

or in energy units:

$$\frac{\hbar^2q^2}{2m} = E_0 + E_1 - 2\sqrt{E_0E_1}cos\vartheta \tag{2.5}$$

In the direct geometry configuration E_0 is selected. Thus equation (2.5) becomes:

$$\frac{\hbar^2q^2}{2m} = 2E_0 - \omega - 2\sqrt{E_0(E_0-\omega)}cos\vartheta \tag{2.6}$$

For an inverse geometry instrument E_1 is selected and the relation (2.5) becomes:

$$\frac{\hbar^2q^2}{2m} = 2E_1 + \omega - 2\sqrt{E_1(E_1+\omega)}cos\vartheta \tag{2.7}$$

From a kinematical point of view, the main difference between the direct and inverse configuration is that in the direct geometry the maximum energy loss is limited to E_0, while there is no limit to the energy loss in the inverse geometry instruments. This can be argued in Figures 2.3 and 2.4, where contour plots of equal scattering angles are plotted as a function of wavevector and energy transfers for fixed initial (Fig. 2.3) and final (Fig. 2.4) neutron energy of 6.67 eV.

Figure 2.3: contour plot of iso-angular loci as a function of wavevector and energy transfers for a direct geometry instrument with $E_0 = 6.67$ eV

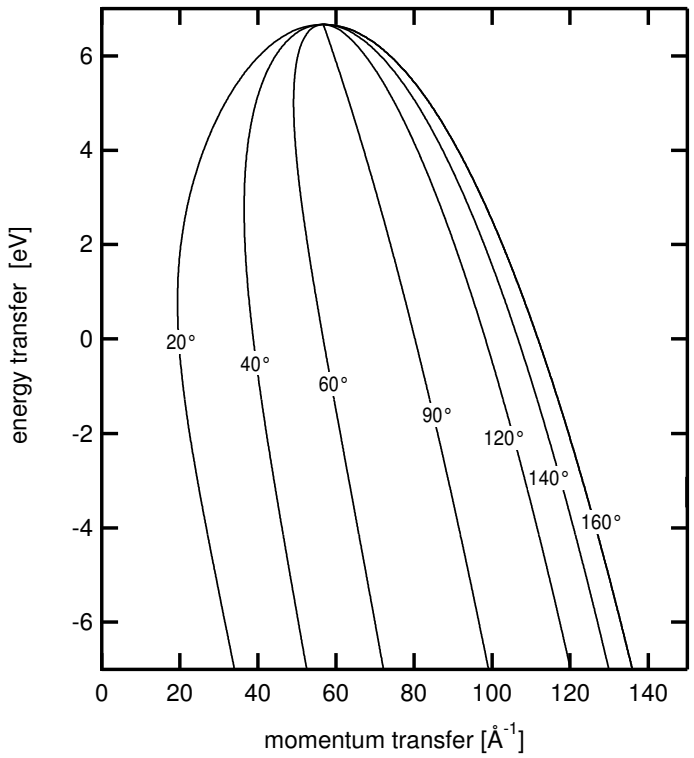

Figure 2.4: contour plot of iso-angular loci as a function of wavevector and energy transfers for an inverse geometry instrument with $E_1 = 6.67$ eV

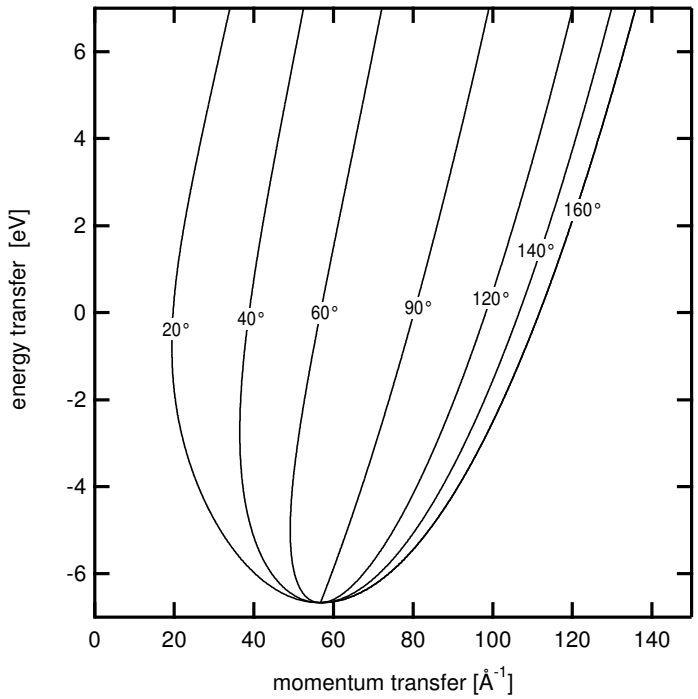

2.4 The VESUVIO inverse geometry spectrometer

VESUVIO is an inverse geometry neutron spectrometer operating at ISIS spallation source [31]. On this instrument the incident neutron beam is characterised by a white energy spectrum, resulting from the use of a water moderator at 295 K. The spectrum, shown in Figure 2.5, exhibits a peak at about 0.03 eV and a $E_n^{-0.9}$ tail in the epithermal region, E_n being the incident neutron energy. The main instrumental parameters of the spectrometer are listed in Table 2.1, while Figures 2.6 and 2.7 represent schematic drawings of VESUVIO. From

Table 2.1: Main instrumental parameters of the VESUVIO spectrometer at ISIS

Geometry configuration	Inverse
Energy analysis method	nuclear resonance
Neutron detectors	^{6}Li-glass
L_0	11.055 m
L_1	$\sim$ 0.7 m
Forward angular range	30°-70°
backward angular range	120°-170°
(q,ω) range accessed	$q \geq 30$ Å^{-1}, $\omega \geq 1$ eV

fig. 2.6 it can be noticed that VESUVIO can perform scattering measurements in both backward and forward directions, by employing two different banks of detectors. Furthermore, employing nuclear resonances to select final neutron energy, this spectrometer can be set up in the Resonance Filter (RF) or in the Resonance Detector (RD) configuration. These two different configuration are described in details in the following sections.

2.4.1 VESUVIO as a Resonance Filter spectrometer

The Resonance Filter (RF) spectrometer is an inverse geometry instrument that performs the scattered neutrons energy analysis using nuclear resonances. The neutron absorption cross sections of isotopes such as ^{238}U, ^{197}Au or ^{139}La are characterised by the presence of intense and narrow resonances in the electron Volt energy region. Figures 2.8 and 2.9 show the absorption cross section of two isotopes, namely ^{238}U and ^{197}Au, which are commonly used as energy filters. The principle of the measurement in such configuration is very simple. The physical signal is provided by the difference between two measurements: the first with the analyser filter inserted in the scattered neutron beam (the

Figure 2.5: Incident neutron energy spectrum of the VESUVIO spectrometer.

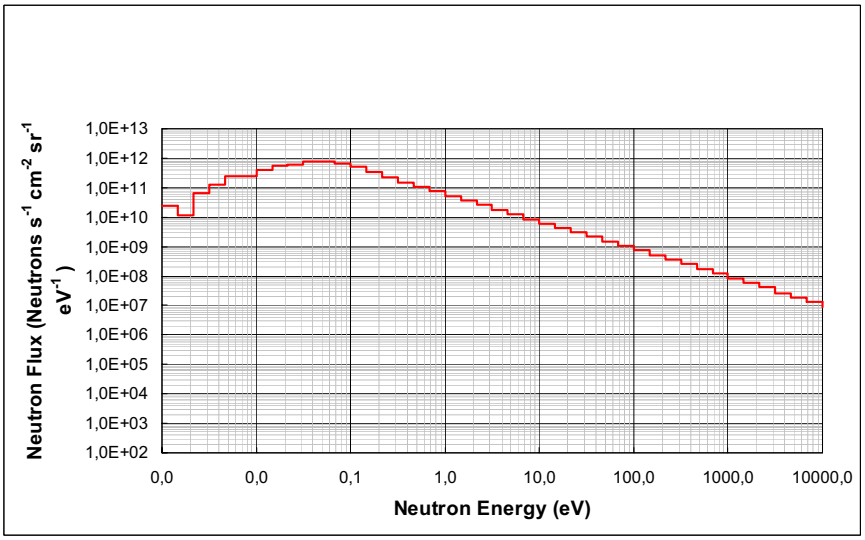

so-called *foil-in* measurement), the second with the foil removed (*foil-out* measurement). This procedure is known as the Filter Difference (FD) method [74]. The neutron counting is provided by an array of ^{6}Li-glass scintillation detectors which respond to all energies with an efficiency depending on $\frac{1}{v}$, v being the neutron velocity.

The energy analyser can be described as a pass-band filter as it selects neutron energy within a region corresponding, at a first approximation, with the total width of one of the resonances. The overall response of a RF spectrometer can be described as a convolution of the filter's transmission function with the one describing the geometrical contribution to the total instrument resolution.

The energy dependent transmission function of the filter is given by:

$$T(E) = exp[-\rho\sigma_{eff}x\overline{f}(E)] \tag{2.8}$$

Figure 2.6: Schematic layout of the VESUVIO spectrometer.

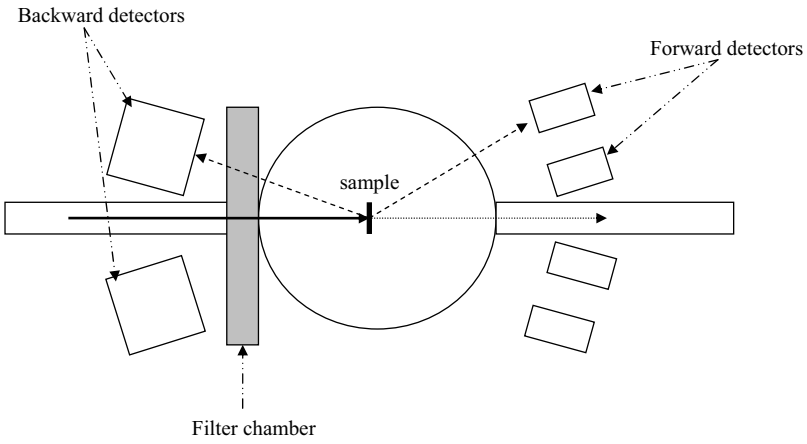

where $\overline{f}(E) = \frac{f(E)}{f(E_r)}$ is the normalised nuclear absorption profile, σ_{eff} is the effective total cross section at the peak of the resonance, x the thickness and ρ the nuclear density of the filter, respectively. The shape of the single nucleus resonance cross section, neglecting the $\frac{1}{v}$ tail and the Doppler broadening can be described, with good degree of a accuracy, by a lorentzian function:

$$L(E) = \frac{1}{\pi} \frac{\Gamma_r}{\Gamma_r^2 + (E - E_r)^2} \ , \tag{2.9}$$

E_r being the resonance energy ($E_1 \equiv E_r$) and Γ_r, independent of E, the half width at half maximum (HWHM). This expression is assumed to represent the free-nucleus nuclear absorption profile. The latter is broadened due to the thermal motion of the nuclei bound in the lattice, so that the overall lineshape is given by the convolution of the function (2.9) with a gaussian function, representing the Doppler broadening, providing an overall Voigt profile [75,76]. By defining the dimensionless parameter $\tau = \rho\sigma_{eff}x$, the transmission function

Figure 2.7: Schematics of the rotating filter chamber of the VESUVIO spectrometer.

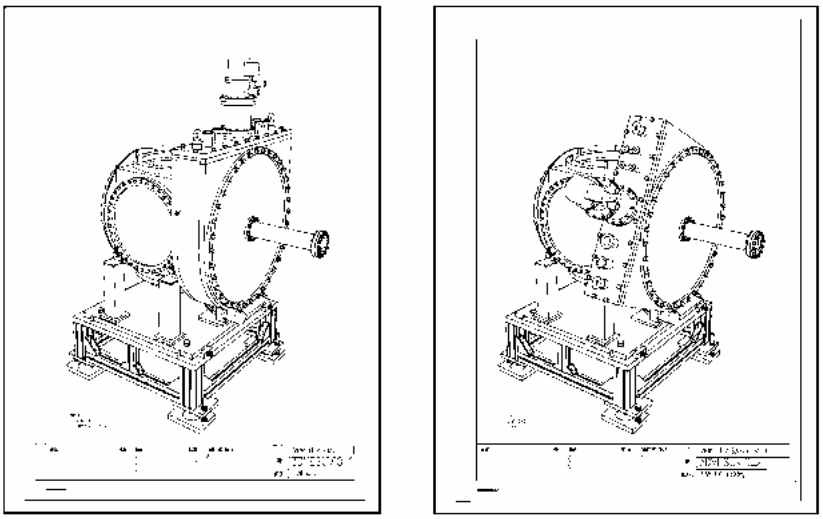

can be written as:

$$T(E) = exp[-\tau \overline{f}(E) \tag{2.10}$$

so that the analyser$'$s transfer function is given by:

$$X(E) = 1 - T(E) \; . \tag{2.11}$$

The transfer function contributes to the overall spectrometer's resolution, $R(E)$, which can formally be written as:

$$R(E) = X(E) \otimes G(E) \; , \tag{2.12}$$

$G(E)$ being a gaussian function which represents the geometrical component of the resolution. In general the energy component $X(E)$ dominates the resolution in a wide energy range. Anyway this contribution can be lowered by cooling the filter and/or employing the Double Difference Method (DDM) [75],

Figure 2.8: the neutron absorption cross section of ^{197}Au in the energy range 0.1 - 100 eV

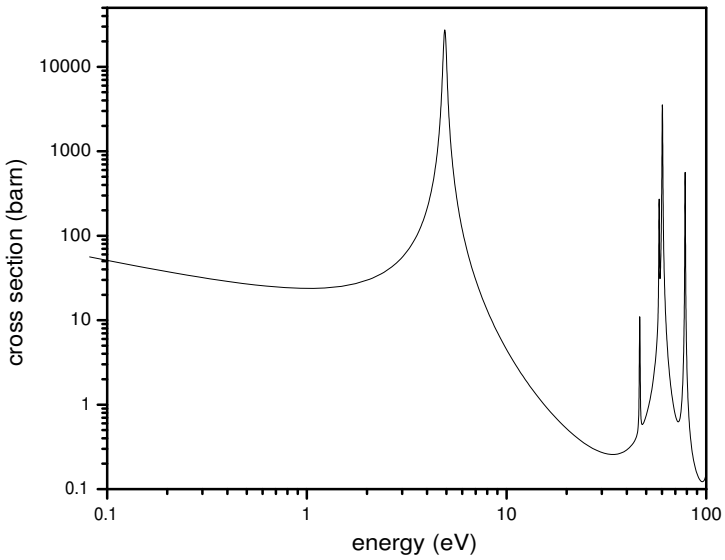

whose main features are briefly described in the following.

In the DDM two filters of different thickness, t_1 and t_2 with $t_2 = t_1 \cdot \alpha^{-1}$ ($0 \leq \alpha \leq 1$), are employed. The transfer function results from a linear combination of the form [76]:

$$X_{DD}(E) = X_{SD}^{t_1}(E) - \alpha X_{SD}^{t_2}(E) = [1 - e^{-\tau \overline{f}(E)}] - \alpha[1 - e^{-\tau \overline{f}(E)\alpha^{-1}}] \quad (2.13)$$

i.e. the difference between two standard FD measurements. Referring to [76] for a detailed discussion of the analytical calculations, it has to be stressed that the main advantages of the DDM are an appreciable reduction of the contribution of the energy component to the overall resolution and an appreciable change in the shape of the lorentzian wings of the transmission function. In

Figure 2.9: the neutron absorption cross section of ^{238}U in the energy range 1 - 100 eV

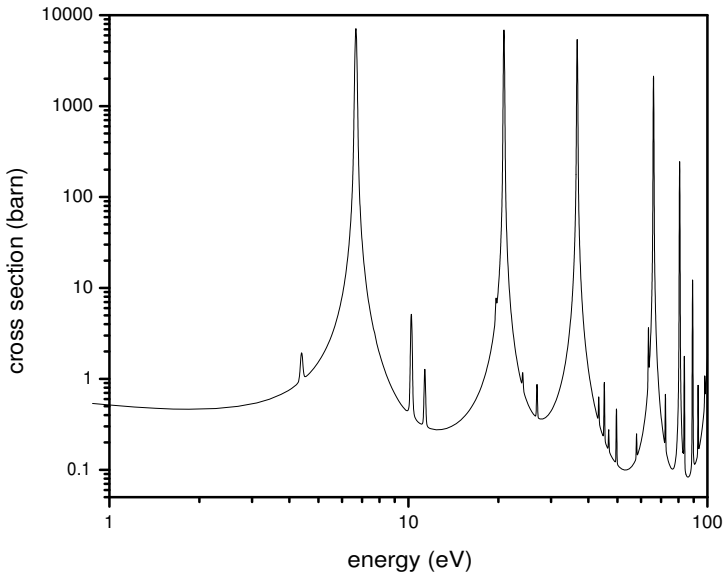

facts the lorentzian wings of $X_{SD}(E)$ approximatively scale with the thickness of the analyser filter, and the weighted difference (2.13) allows a consistent reduction of the $X_{DD}(E)$ wings.

As a matter of fact the main limitation of the VESUVIO spectrometer configured in the RF set up, is the decreasing counting efficiency of the ^{6}Li-glass detectors with increasing neutron velocity. At high neutron energies (above 10-15 eV) the detection efficiency loss of these neutron counters and their neutron and γ background sensitivity becomes the main limiting factor for their effective employment in scattering measurements.

In the standard RF configuration for forward scattering, VESUVIO operates

with four banks of ^{6}Li-glass scintillation detectors, placed at an average distance of about 70 cm from the sample, covering the angular range between 30° and 70°. In the backward direction (fig. 2.7) the detection system is composed by a rotating device (filter chamber), allocating analyser filters of different thickness, and by a fixed aluminum hexagonal frame where ^{6}Li-glass detectors are placed at an average distance of about 80 cm from the sample position. The sample tank and the filter chamber have been constructed by the RMP-Costruzioni Meccaniche (Acilia-Italy) and may operate under vacuum. In the filter chamber a closed-cycle refrigerator may cool down the analyser filters to liquid nitrogen temperature (about 10 K). This allows lowering the Doppler contribution to the energy component of the resolution function. Furthermore the rotation of the filter chamber allows for scattering measurements employing the DDM, with an improvement of the instrument resolution as already discussed before. The performances of the cryogenic filter chamber have been tested using both gold and uranium filters and a lead calibration sample, providing appreciable enhancement of the resolution and a sensitive reduction of the lorentzian wings [77] as compared to previous measurements on the eVS spectrometer.

VESUVIO operates since the 2002 with the overall set up described before, accessing a region of the (q,ω) kinematical space characterised by high energy ($\omega \geq 1$ eV) and high wavevector ($q \geq 30$ Å^{-1}). Many interesting experiments devoted to the study of condensed matter, ranging from quantum systems [78–83] to molecular fluids and solids [84–87], have been performed on both eVS and VESUVIO, witnessing a growing interest for electron Volt neutron spectroscopy.

2.4.2 VESUVIO as a Resonance Detector spectrometer

The Resonance Detector (RD) spectrometer is an inverse geometry instrument employing nuclear resonances to select final neutron energy. The neutron counting is not provided by standard neutron counters, as it applies in the RF, but by photon detectors which reveal the prompt γ-ray cascade produced, via (n,γ) reactions, by scattered neutron absorption by an analyser foil. In this way the instrument responds mainly to the analyser's resonances, differently from what happens in the RF where the neutron counters reveal all neutron energies with different efficiency. Furthermore it has to be outlined that, differently from what happens for the RF, the experimental signal for a RD is provided directly from the *foil-in* measurement an thus there is no need to employ the FD method.

The RD spectrometer was first been proposed as an experimental configuration for neutron spectroscopy between the end of 1970$'$s and the early 80$'$s [33–37, 39, 40, 45]. Early experimental works was performed with different radiation detectors such as solid state detectors [40, 41] or scintillators [42, 44]. The main limiting factor of this technique was the need of heavy shielding around the γ detectors due to their high sensitivity to background or because of the radiation damage effects due to the high fluence of fast neutrons. This experimental configuration has been revised by our group starting in the year 2000 and several experimental tests have been performed on eVS and VESUVIO spectrometers, employing different detectors in order to improve the performances of the RD for neutron spectroscopy.

A detailed description of the operational mechanism of the RD configuration is presented in the following. Figure 2.10 is a schematic of the RD set up. The

Figure 2.10: Schematic of the Resonance Detector spectrometer configuration

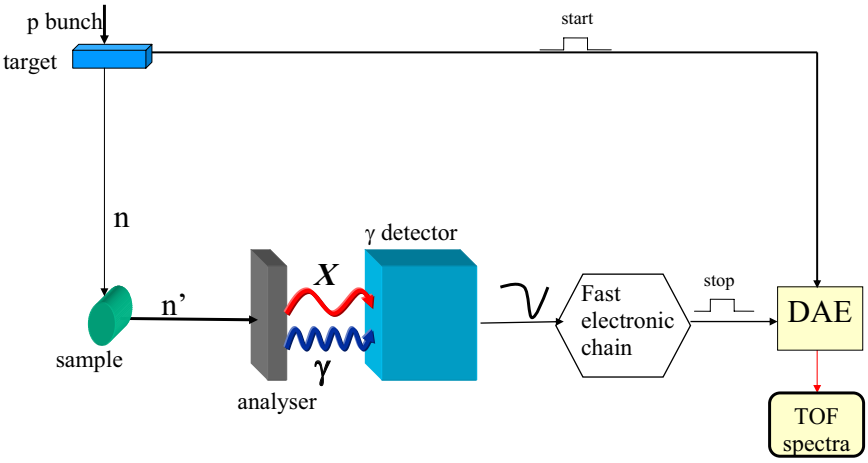

RD counting procedure relies upon two main steps, which will be examined in detail. In the first step the scattered neutron beam impinges onto the analyser foil which provides energy analysis by means of resonant absorption. The energy selection is really effective given that the foil's thickness is generally chosen to be in the order of one interaction length, λ, for resonant neutrons ($E = E_r$):

$$\lambda = \frac{A}{N_A \rho \sigma(E_r)} \tag{2.14}$$

A being the atomic weight, N_A the Avogadro's number, ρ the mass density of the analyser and $\sigma(E_r)$ the peak value of the resonance cross section. A neutron having an energy within the width of the resonance is strongly absorbed while an off-resonance neutron is less likely to suffer and interaction. For these off-resonance neutrons the interaction probability can be approximated by $\frac{t}{\lambda}$. As in general the ratio of the peak value of the resonance to the off resonance

cross section is in the range 10^3-10^4, the ratio $\frac{t}{\lambda}$ lies in the same range as well. The resonant neutrons, on the other hand, are absorbed with an efficiency given by:

$$\varepsilon(E_r) = 1 - e^{-\frac{t}{\lambda(E_r)}} \tag{2.15}$$

for $t \simeq \lambda$ (at the resonance energy) $\varepsilon(E_r) \simeq 0.63$.

The radiative capture reaction can be described as follows:

$$A + n \rightarrow (A+1)^* \rightarrow (A+1) + \sum_i^N \gamma_i + K \tag{2.16}$$

where a nucleus A absorbs a neutron n and an excited compound nucleus $(A+1)^*$ is formed which decays within a short time ($\leq 10^{-16}$ s) with the emission of a γ cascade $\sum_i^N \gamma_i$, arising from nuclear single particle de-excitations. The last term K in (2.16) is the nucleus recoil energy which can be neglected for any practical case. In the medium and heavy nuclei, neutron resonances are found at low energies (1-100 eV for ^{238}U) if compared to the typical values of the nuclear interaction potential (in the order of tens of MeV) and the partial wave expansion of the cross section can be truncated at l=0 (s-wave) [88]. The resonance lineshape can thus be described with good approximation by the typical Breit-Wigner dispersion formula [89, 90]:

$$\sigma_\gamma(E) = \frac{\lambda_D^2}{4\pi} \frac{2J+1}{2(2I+1)} \frac{\Gamma_n \Gamma_\gamma}{(E-E_r)^2 - (\frac{\Gamma}{2})^2} \tag{2.17}$$

where λ_D is the De Broglie's wavelength of the particle, I and J are the spins of the target nucleus and of the compound nucleus, respectively. The term Γ_n is the partial neutron line width (related to the rate for formation of the compound nucleus state) while Γ_γ is the partial width for decay of resonance by γ emission and Γ is the total resonance width.

In the second step the prompt γ's are detected to assign the total neutron

TOF. Referring to fig. 2.10, the γ detection produces a voltage signal which is processed by a fast electronic chain, providing the stop signal for the acquisition electronics.

It has to be stressed that the γ detector is used as a counter. For each absorbed neutron into the analyser there is a production of a γ-ray cascade. It is enough that one photon among the whole cascade is detected, even by a partial release of its energy in the detection medium, to trigger a stop signal for the TDC. This stop signal is practically produced at the same time the neutron is absorbed into the analyser, with a fixed time delay produced by the signal processing (generally less than 1 μs). Once the detector, the foil area and their relative distance have been chosen, the total detection efficiency depends on the (n,γ) cross section, the γ detection efficiency and on the probability of γ self-absorption in the analyser.

One important difference with respect to the RF configuration is that the neutron counting efficiency, η_d, is mostly independent of neutron energy in the RD configuration. This will be explained in some detail in Chapter 3.

2.5 Experimental techniques

On VESUVIO spectrometer inelastic neutron scattering measurements are routinely performed at high-ω (above 1 eV) and high-q (above 20 Å^{-1}), while the new instrumentation equipment described in Chapter 5, the very low angle detector bank (VLAD), will allow neutron scattering and at high-ω (above 0.3 eV) and low-q (below 10 Å^{-1}).

Next Sections are devoted to a brief description of the DINS and HINS experimental techniques.

Figure 2.11: Behaviour of the dynamic structure factor $S(\overrightarrow{q}, \omega)$ from collective to single particle dynamics (Source: R. Simmons [91])

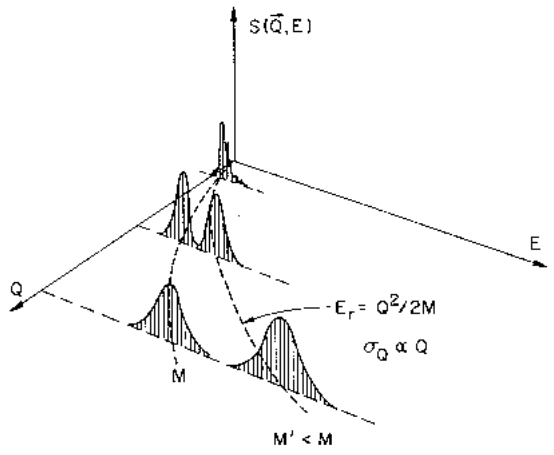

2.5.1 Deep Inelastic Neutron Scattering (DINS)

Neutron scattering is often regarded as a sensitive probe of collective properties in condensed matter; however, when the magnitude of energy and wavevector increases, short-scale single-particle properties are probed. The scattering occurs so rapidly, compared to the time-scales of atomic motion in the sample, that the measured response is rather simply related to the equilibrium momentum distribution of the atoms.

Momentum distributions are usually measured by scattering experiments in which the energy and momentum transferred are very high compared to the energies and momenta characteristic of ground-state properties and collective behavior. In this limit, the scattering law may be related to the momentum distribution within the framework of the impulse approximation (IA),

which assumes that a single particle of the system is struck by the scattering probe, and that this particle recoils freely from the collision. Neutron scattering at energies above 1 eV is used to measure atomic momentum distribution $n(p)$ in condensed matter, photon scattering at energies of tens of keV is used to measure electronic $n(p)$ in condensed matter, electron scattering at tens-hundreds of MeV energies is used to measure $n(p)$ of nucleons and inside nuclei. The experimental method described here is known as neutron Compton scattering (NCS) or Deep Inelastic Neutron Scattering (DINS). The information obtainable through DINS is to some extent complementary to the one from diffraction experiments. The latter measures the Fourier transform of a time-averaged density; the former measures the instantaneous momentum density. This last information is of particular interest if the motion of atoms is well described by an effective (Born–Oppenheimer) potential, or adiabatic energy surface. An example may be found in molecular solids where a proton is bound in a heavy lattice at thermal energies (*i.e.* temperatures) well below the energy of the neutron. In this case, the momentum distribution is given by the squared amplitude of the Fourier transform of the proton wave function, and from it, the potential energy function can be extracted [92].

The quantity which can be determined in a neutron scattering experiment is the partial differential cross section by a system of atomic nuclei.

Focusing on the behaviour of $\frac{d^2\sigma}{d\Omega dE_r}$ in the high wavevector and energy transfers regime, the theory of "low energy" neutron scattering states [1]:

$$\frac{d^2\sigma}{d\Omega dE_1} = \frac{k_1}{k_0}\sigma_t S(\overrightarrow{q},\omega) \tag{2.18}$$

where k_0 and k_1 are the initial and final neutron wavevectors and $\sigma_t = \sigma_{coh} + \sigma_{incoh} = 4\pi(|\overline{b}|^2 + \delta_{jj'}(\overline{|b|^2} - |\overline{b}|^2))$ (b being the scattering length) is the total

scattering cross section, and $S(\overrightarrow{q},\omega)$ is the dynamic structure factor. For $\omega \geq \omega_M$ and $q \leq \frac{2\pi}{d}$, ω_M being the maximum excitation energy of the system and d the nearest-neighbor distance, the scattering can be described within the framework of the IA [1] and the dynamic structure factor assumes the form:

$$S(\overrightarrow{q},\omega)_{IA} = \frac{1}{4\pi\hbar}\int_{-\infty}^{\infty} d\overrightarrow{p}\ n(\overrightarrow{p})\ \delta(\omega - \frac{\hbar\, q^2}{2M} - \frac{\hbar}{M}\overrightarrow{q}\cdot\overrightarrow{p})\ , \tag{2.19}$$

$\omega_R = \frac{\hbar^2 q^2}{2M}$ being the free-atom recoil energy.

Considering. for instance, a single atom at rest, then the scattering will be represented by $\delta(\omega - \frac{\hbar\, q^2}{2M})$, *i.e.* a peak in the dynamic structure factor at the recoil energy ω_R (see Figure 2.11). Not all the target atoms will be at rest, and a probability distribution function (pdf) of atomic momentum will weight the peak of $S(\overrightarrow{q},\omega)$ to account for the spread of atomic momenta. The determination of the extent and the nature of this "spread" is the objective of DINS measurements in the IA.

In eq.(2.19), the dynamic structure factor in the IA limit, the scattering is no longer a function of the energy and wavevector transfer separately. Since ω and $\overrightarrow{q}$ are closely related, it is useful to introduce a new variable, y, which couples wavevector and energy transfer [93]:

$$y = \frac{M}{\hbar^2 q}(\omega - \omega_R) \tag{2.20}$$

so that

$$\delta[\frac{\hbar\, q}{M}(y - \overrightarrow{p}\cdot\widehat{q})] = \frac{M}{\hbar q}\ \delta(y - \overrightarrow{p}\cdot\widehat{q}) \tag{2.21}$$

Considering an isotropic system and choosing the z-axis along the scattering vector, then $\overrightarrow{p}\cdot\widehat{q} = p_z = y$ and the dynamic structure factor can be written as [1]:

$$S(\overrightarrow{q},\omega)_{IA} = \frac{M}{4\pi\hbar^2\, q} 2\pi \int_{|y|}^{\infty} dp\ p\ n(p)\ . \tag{2.22}$$

Defining $J(y)$ as:

$$J(y) = \frac{2\pi\hbar^2 q}{M} S(\overrightarrow{q},\omega)_{IA} = \int_{|y|}^{\infty} dp\ p\ n(p) \tag{2.23}$$

one obtains an equation relating, in the IA, the dynamic structure factor $S(\overrightarrow{q},\omega)$ to the momentum distribution of an isotropic system along the scattering direction. $J(y)$ is called the Neutron Compton Profile (NCP) or Longitudinal Compton Profile (similarly to photon-electron scattering and electron-nucleon scattering techniques), and represents the probability distribution function of atomic momentum along $\widehat{q}$, *i.e.* $n(y)$. From the general moment relations for the incoherent response functions [1], it is possible to derive the single-atom mean kinetic energy, $\langle E_K \rangle$:

$$\langle E_K \rangle = \frac{3\hbar^2}{2\ M} \int_{-\infty}^{\infty} y^2\ J(y) dy \tag{2.24}$$

where, by definition of probability distribution function $\int_{-\infty}^{\infty}\ J(y)dy = 1$ and zero first moment. Kinetic energy and momentum distributions are quantities difficult to measure and DINS is a unique probe for this purpose.

As a general comment, from a kinematical point of view to achieve the experimental conditions allowing to apply the IA with increasing degree of accuracy, high energy neutrons in the initial and final state are needed.

2.5.2 High energy Inelastic Neutron Scattering (HINS)

Epithermal neutrons can effectively be employed to access a still unexplored region of the kinematical space (q, ω), namely $q \leq 10$ Å^{-1}coupled to $\omega \geq$ 1 eV. These kinematical conditions define the high energy inelastic neutron scattering (HINS) regime. From a kinematical point of view to access this

region of the (q,ω) space, high energy neutrons in the final state have to be detected at small scattering angles. This can be argued by Figure 2.12 where a contour plot of iso-q loci as a function of final energy and scattering angle is shown for a fixed reference energy transfer $\omega = 1.5$ eV. Accessing the HINS

Figure 2.12: Contour plot of iso-q loci as a function of the final neutron energy and the scattering angle, for a fixed energy transfer $\omega = 1.5$ eV.

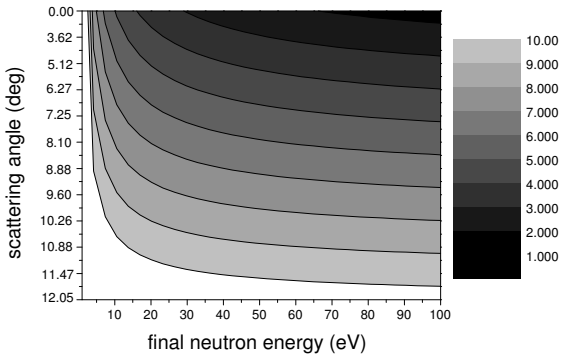

regime will allow new experimental studies in condensed matter.

By considering the nuclear interaction of neutrons with atomic nuclei, HINS provides information on the dynamical structure factor $S(\overrightarrow{q},\omega)$, depending on the density of states $g(\omega)$ and on the vibration amplitude $\langle u^2 \rangle$ of each atom in the molecule, weighted by its neutron scattering cross section. In a hydrogenated sample, the large incoherent cross sections and the low mass of the proton ensure that the contribution to $S(\overrightarrow{q},\omega)$ coming from molecular vibrations involving hydrogen, dominate the scattering intensity [94]. In the kinematical region at low momentum (q <10 Å^{-1}) and high energy transfers ($\omega \geq 0.3$ eV), HINS measurements allows to access the one-phonon compo-

nent, $S_{M,\pm1}(\overrightarrow{q},\omega)$ of hydrogen-projected scattering function, $S_m(\overrightarrow{q},\omega)$. The expression of the cross section in this case is given by [95]:

$$S_{m,\pm1}(\overrightarrow{q},\omega) = \frac{\hbar q^2}{4m}\exp\left(-\frac{1}{3}q^2\langle u^2\rangle_m\right)\frac{g(\omega)}{\omega}\left[\coth\left(\frac{\omega}{2k_BT}\right)+1\right] \tag{2.25}$$

where $g_m(\omega)$ is the density of states, projected on the hydrogen atoms of the unit cell and $\langle u^2\rangle_m$ is the nuclear mean squared displacement, averaged over the hydrogen atoms of the unit cell. This equation is derived within the isotropic approximation, where contributions from all atoms are considered equivalent and described by a simple harmonic model. The relatively low wavevector transfers enable the extraction of a reliable density of states [95].

On the other hand, HINS can be induced by the neutron magnetic interaction (through its magnetic moment) with the electron spin of the unpaired electrons. In such cases the theory [96–102] states that the double differential scattering cross section is given by:

$$\frac{d^2\sigma}{d\Omega dE_0} = \frac{k_1}{k_0}|f(\overrightarrow{q})|^2\delta(E_0 - E_1 - \omega) \tag{2.26}$$

where $\overrightarrow{q} = \overrightarrow{k_0} - \overrightarrow{k}_1$ is the neutron scattering vector and $\omega = E_0 - E_1$ is the energy transfer. The $f(\overrightarrow{q})$ term is the magnetic form factor, which for dipolar transitions sharply falls from its maximum value at $q = 0$, while for nondipolar transitions (which have zero intensity at $q = 0$) exhibits a maximum in the range 5-15 Å^{-1}as shown in Figure 2.13 for Praseodymium. From a kinematical point of view, HINS accesses a region of the kinematical (q,ω) space which is complementary to that accessed by chopper direct geometry spectrometers. As a specific example, the high energy transfer (HET) direct geometry spectrometer at ISIS spallation source is optimised to study the high energy magnetic excitations above 50 meV. Anyway, being a direct geometry

Figure 2.13: magnetic from factors for dipolar and non-dipolar electronic transitions in Praseodymium (source: A. Taylor et al. [103])

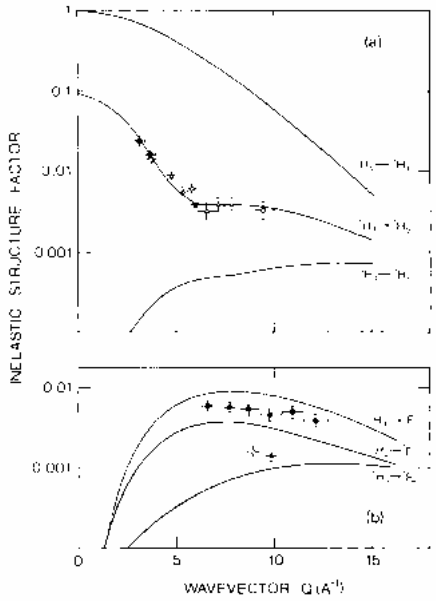

instrument, the maximum energy loss is limited to the value of the maximum initial neutron energy (about 2 eV).

This is a limitation for the study of high-lying excitations ($\omega \geq 1$ eV). In fact as it can be argued from Figures 2.12 and 2.14 and final neutron energies and small scattering angles are needed to access higher energy transfers, maintaining low q. The kinematical constraints are determined by the q dependence of the magnetic form factor $f(\overrightarrow{q})$ as sketched in Figure 2.15 where $f(q)$ is plotted for Ho^{3+} and Cr.

Extending the energy transfer scale above 800 meV - 1 eV with an associated low value of q, would allow a significant advance in the study of crystal field levels in rare earth intermetallic compounds and magnetic materials, or the inter-band electronic transitions, to be observed as a function of q, in insulator and semiconductors. On HET, intermultiplet transitions with energies up to about 800 meV have been observed in Praseodymium [103], just to mention an example, employing monochromatic incident neutron beams up to about 1.7 eV. In order to observe higher lying transitions (*e.g.* the $^3H_4 \rightarrow {}^1G_4$ expected at about 1.2 eV) higher incident and final neutron energies are required.
On the other hand, for experiments involving still larger excitation energies (2-6 eV) epithermal neutrons can be used a direct probe of the electronic band structure of materials such as semiconductor or insulators.

Figure 2.14: contour plots of iso-q loci as a function of final energy E_1 and energy transfer ω for three different scattering angles, namely 1° (a), 3° (b) and 5° (c)

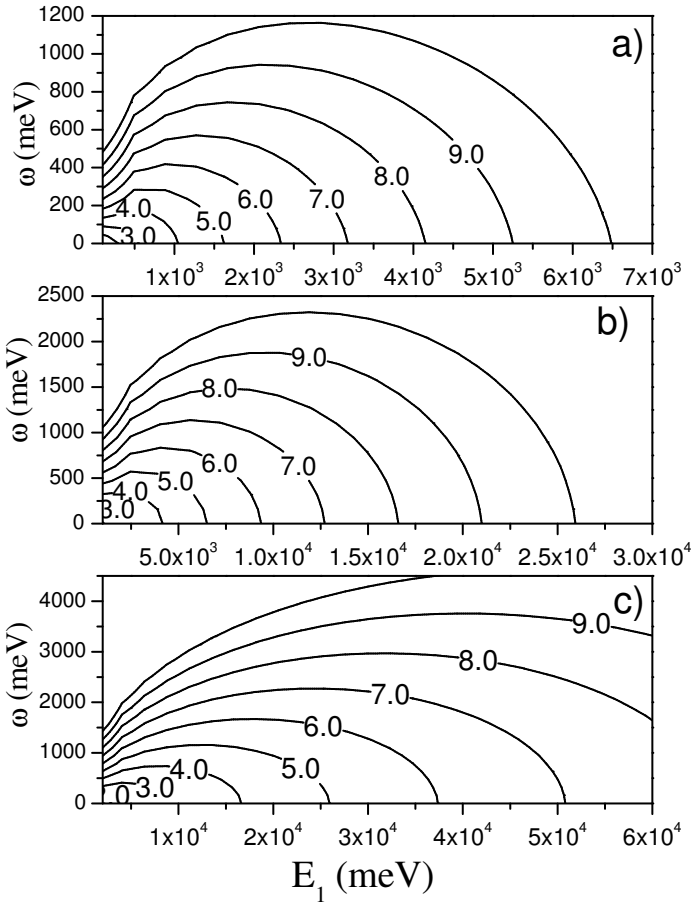

Figure 2.15: magnetic form factors of Ho^{3+} and Cr

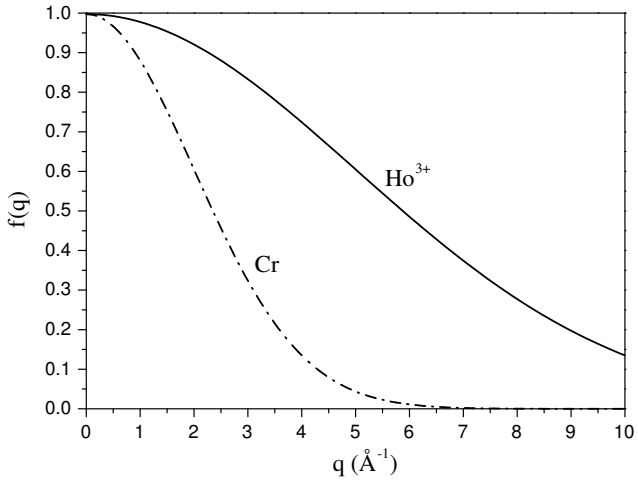

Chapter 3

An overview on the resonance detector spectrometer configuration

Most of the experimental work on detectors, presented in this dissertation, has been devoted to find the best detection system (analyser-γ detector) to perform HINS measurements VESUVIO spectrometer, by means of the VLAD equipment.
A lot of work has been done in order to revise the RD configuration on VESUVIO through a series of experiments described in the next Chapter.
A very important task of my overall experimental activity before the measurements on the spectrometer, relied upon a series of preliminary studies that can be summarised as follows:

- bibliographic research on the RD configuration and study of the previous experiments and results;

- detailed research of suitable materials to be used as analyser foils for the RD configuration on VESUVIO;
- study of the characteristics of different γ detectors in order to choose the most suitable ones for the experiments on VESUVIO.

These items allowed an almost thorough comprehension of the experimental technique, through the recognition of the role played by each component of a RD spectrometer.
The role of the analyser and of the γ detector and the choice criteria of these RD components are discussed in Sections 3.2 and 3.3, while some considerations on the RD efficiency are presented in Section 3.4.

3.1 Neutron detection techniques in the eV region: ^{6}Li-glass detectors versus Resonance Detectors

The detection of the neutrons employed for condensed matter studies (from ultra-cold to epithermal) is based on nuclear reactions, where a neutron is absorbed and charged particles are produced and then detected by energy release.
The main nuclear reactions employed for neutron detection are listed in Table 3.1. Since the Q-value of all these reactions is positive, they may be triggered by neutrons of all kinetic energies always releasing the same energy to the detector$'$s active medium. The direct spectroscopic measurement of neutron energy based on these reactions is not possible in the energy range of interest

Table 3.1: list of the nuclear reactions useful for neutron detection

Reaction
n + ^{3}He $\rightarrow^{3}$H + ^{1}H + 0.764 MeV
n + ^{6}Li $\rightarrow^{4}$He + ^{3}H + 4.80 MeV
n + ^{10}B $\rightarrow^{7}$Li* + ^{4}He $\rightarrow^{7}$Li + ^{4}He + γ (0.480 MeV) + 2.3 MeV (br 0.93)
n + ^{10}B $\rightarrow^{7}$Li* + ^{4}He $\rightarrow^{7}$Li + ^{4}He + 2.8 MeV (br 0.07)
n + ^{155}Gd $\rightarrow$ Gd* $\rightarrow$ γ-rays $\rightarrow$ conversion e^{-}
n + ^{157}Gd Gd* $\rightarrow$ γ-rays $\rightarrow$ conversion e^{-}
n + ^{235}U $\rightarrow$ fission fragments + 160 MeV
n + ^{239}Pu $\rightarrow$ fission fragments + 160 MeV

for condensed matter, because the intrinsic kinetic information is lost in the large amount of energy released in the reaction. To perform a neutron scattering measurement it is necessary to select neutron energy before counting. Once the charged particles has been produced by the one of the nuclear reactions listed in tab. 3.1, they can be revealed employing suitable detectors such as proportional chambers, ionization chambers, scintillators or semiconductor detectors.

While reactions involving ^{6}Li are effectively employed on VESUVIO$'$s detectors for neutrons up to about 10 eV, their use for epithermal neutrons in the range 10-100 eV (useful for DINS and HINS as discussed in Chapter 2) is not reliable due to the fast decrease of the absorption cross section as sketched in Figure 3.1. To ensure a good detection efficiency at high neutron energies the thickness of the crystals should be scaled proportionally to the variation of the neutron absorption cross section (typical crystals employed on VESUVIO are 1-2 cm thick). This represents both a technical problem, mostly related to crystal growth techniques (maximum thickness commercially available in the order of 5 cm), and a physical one related to the enhanced background sensi-

Figure 3.1: neutron absorption cross sections of ^{6}Li and ^{3}He

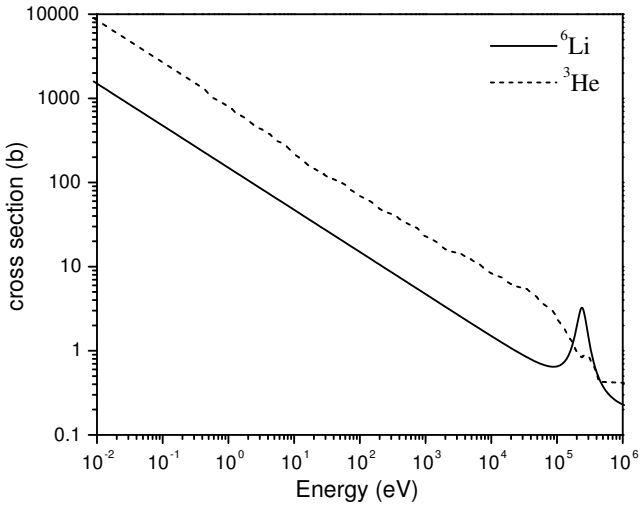

tivity of big volume ^{6}Li-glass detectors which have good γ detection efficiency as well.

The aim of accessing the HINS regime and to improve the performances for DINS measurements on VESUVIO, has motivated an important experimental activity for the development of high energy neutron detectors. In this context the RD configuration seems the most effective for these purposes for a series of physical and technical characteristics that are described in the following sections.

3.2 Choice of the analysers in the RD configuration

As explained in Chapter 2, the RD neutron counting concept relies upon a combination of an analyser (n-γ converter) and a photon detector which is employed as a neutron counter. The analyser foil has to fulfill some important requirements: *i*) the radiative capture cross section has to show isolated and intense resonances in the energy region of interest (E_r = 1-100 eV), *ii*) these resonances should have small widths as compared to E_r, *iii*) the emitted γ-ray spectrum should contain lines with appreciable relative intensities in a wide energy range. The first two requirements are important in order to properly select the scattered neutron energy and to ensure a low contribution to the energy component of the spectrometer's resolution function, respectively. The third requirement allows selecting γ energies to improve the signal to background ratio (S/B), as it will be shown in Chapter 4.

A detailed study of many isotopes has been carried out in order to find the materials fulfilling the proper characteristics for the RD configuration [54]. This detailed investigation allowed to recognise a number of suitable isotopes which are listed in Table 3.2, together with their main physical characteristics. These parameters are the resonance energies E_r, the peak value of the resonance cross section σ_0 and the half width at half maximum Γ_0.

According to the single level theory of Breit and Wigner [90] for an isolated nucleus, the neutron resonance absorption cross section is a lorentzian function of the neutron energy in the laboratory frame where the nucleus is at rest (see eq. (2.17)). In an actual experiment the absorbing nucleus is embedded in a solid. In this case the resonance absorption profile departs from a pure lorentzian

Table 3.2: Main physical parameters of different nuclear resonances which can be employed in the RD configuration

Isotope	E_r (eV)	σ_0 (b)	Γ_0 (meV)
$^{113}In_{49}$	14.6	9965	67
$^{139}La_{57}$	72.2	5969	96
$^{150}Sm_{62}$	20.7	56207	109
$^{160}Dy_{66}$	20.5	16165	124
$^{168}Er_{68}$	79.7	11203	121
$^{178}Hf_{72}$	72.6	16838	112
$^{182}W_{74}$	21.1	46800	104
$^{190}Os_{76}$	91.0	6777	105
$^{197}Au_{79}$	4.96	36592	60
$^{238}U_{92}$	6.67	23564	25
$^{238}U_{92}$	20.8	37966	34
$^{238}U_{92}$	36.6	42228	57
$^{238}U_{92}$	66.0	20134	48

due to the effect crystal lattice [104] and of the chemical bonding [105]. It can be shown that in the case of weak binding between absorbing atoms, defined by the condition [105]

$$\Gamma_0 + \sqrt{RK_BT_{eff}} \gg K_B\Theta_D, \tag{3.1}$$

where Θ_D is the Debye temperature of the solid, K_B is the Boltzmann's constant and R is the recoil energy of the absorbing nucleus, the absorption cross section is given by

$$\sigma = \sigma_0 \cdot \Psi(\xi, x), \tag{3.2}$$

with

$$\Psi(\xi, x) = \frac{\xi}{2\sqrt{\pi}} \int_{-\infty}^{\infty} dy \frac{exp[-(\frac{\xi}{2})^2(x-y)^2}{1+y^2} \tag{3.3}$$

where $x = \frac{E-E_r-R}{\Gamma_0}$ and $\xi = \frac{\Gamma_0}{2\sqrt{RK_BT_{eff}}}$. In the weak binding approximation, the effect of the temperature and chemical bonding on the resonance profile is

described by the effective energy spread:

$$K_B T_{eff} = \frac{1}{2} \int_{\infty}^{\infty} dE\ E\ f(E)\ coth(\frac{E}{2K_B T})\ , \tag{3.4}$$

T being the thermodynamic temperature and $f(E)$ the phonon density of states in the solid.

The neutron absorption probability approaches 1 in the limit of very thick absorbers, however an increase in the absorber$'$s thickness produces an increase of the resonance absorption profile width, thus worsening the resolution of a RD spectrometer and leading to self-shielding effects. An acceptable compromise between high absorption probability and energy resolution is given by the condition $N_d \sigma_0 = 1$, N_d being the number density of resonant absorbing atoms per unit area perpendicular to the neutron beam.

The resonance neutron absorption in the analyser produces a prompt emission of γ-rays up to energies in the order of the neutron binding energy in the absorbing nuclide (several MeV) [106–108]. Due to the high atomic number Z of the typical analysers (Z=92 for ^{238}U) the γ-rays have a finite probability to interact with the innermost orbital electrons and, as a result, the energy of the photons is transferred to the electron which is ejected from the atomic shell. Then the outer electrons drop to a lower energy state to fill the vacancies and this process is followed by the emission of characteristic X-rays [110,111]. This process is known as internal conversion mechanism and it is responsible for an appreciable X-rays emission from the analysers together with the nuclear γ cascade. As it will be shown in Chapter 4, both γ and X-ray emission can be used for neutron counting and TOF determination in the RD configuration.

In figures 3.2 and 3.3 histograms representing the relative intensities as a function of the γ line energy, for both ^{197}Au and ^{238}U taken as examples, are

plotted.

Figure 3.2: Relative intensity vs γ energy for the discrete radiative capture γ emission of ^{238}U

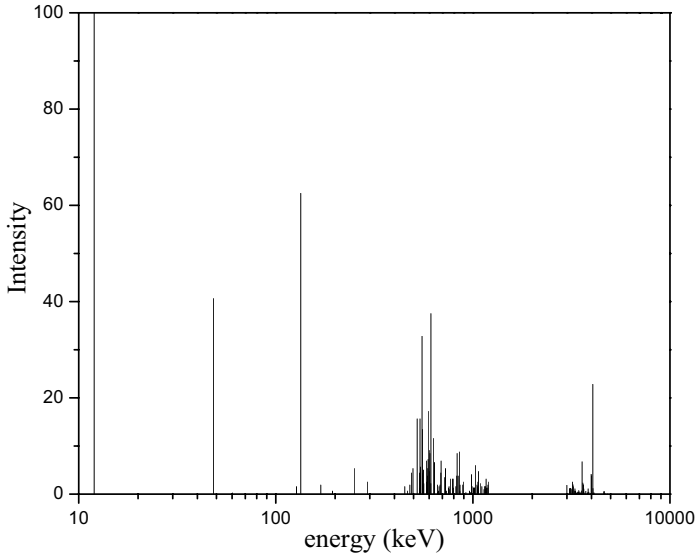

3.3 Choice of the γ detectors for the RD configuration

The role of the γ detector in the RD configuration is the neutron counting. As described in the previous section, the resonance absorption of scattered neutron into the analyser produces a prompt emission of γ-rays, whose detection is also used to assign the neutron TOF through a proper signal processing procedure, as it will be shown in the following.

The spectrometer$'$s efficiency in the RD configuration depends on the neutron

Figure 3.3: Relative intensity vs γ energy for the discrete radiative capture γ emission of ^{197}Au

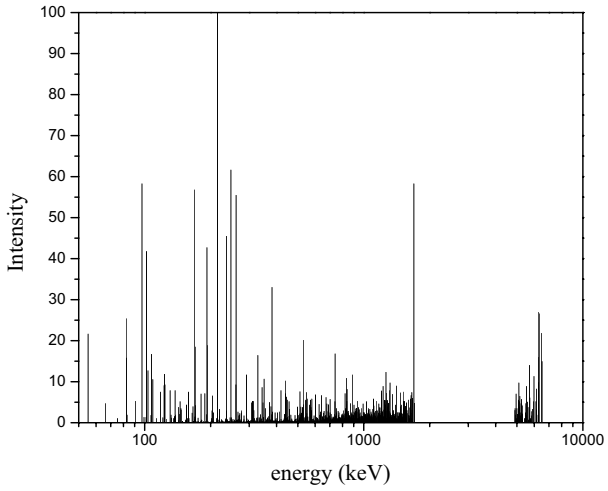

absorption probability in the analyser and on the efficiency of the γ detector as it will be explained below.

The physical characteristics of the detector$'$s active medium are of paramount importance in order to combine good efficiency and low background sensitivity. In fact the environmental operation conditions of a spectrometer are characterised by the presence of heavy neutron and photon background.

The first background component is due to the neutrons scattered off the sample and off the surrounding walls, impinging isotropically onto the detector. The second component is mostly produced by the neutron absorption in the walls of the spectrometer$'$s experimental hall and in the beam dump, both composed of hydrogenated materials, for neutron moderation, and ^{10}B for thermal neutron absorption. Both H and ^{10}B emit characteristic γ-rays, after neutron

absorption, at 2.2 MeV and 480 keV, respectively. Furthermore the neutrons scattered off the walls impinge onto the analyser, where they can be absorbed, inducing (n,γ) reactions, thus contributing a time structured γ background component.

The first requirement of a γ detector is the absence, in the active medium, of isotopes possessing neutron resonances in the 1-100 eV. These resonances produce a beam correlated background with the consequent worsening of the signal to background ratio. Furthermore, the presence of resonance could activate the detector$'$s medium, jeopardizing its detection performances.

The choice of the detector size is related to the energy range of the photons to be detected. Big volume detectors, despite having good efficiency for high energy photons (*e.g.* the typical γ rays from nuclear de-excitations) and providing a good counting efficiency, may have an enhanced background sensitivity and thus need heavy shielding around. Small volume detectors have less background sensitivity, may provide a still good counting efficiency, thanks to the wide energy range of the photons coming from the analyser, and have a higher spatial resolution.

Due to the particular environmental conditions of a neutron source, radiation hard detectors are required for a routine operation on a spectrometer where high fluences of fast neutrons onto the detectors are expected.

Being employed for neutron TOF reconstruction, timing characteristics are important and fast detectors are preferred for rate capability purposes also.

Among the different detectors commercially available, inorganic scintillators and semiconductor detectors have been chosen to perform the experiments presented in the next Chapter.

Inorganic scintillators, commonly used for γ-ray spectroscopy, can be suitably

employed in the RD configuration because of their good efficiency and their timing properties. The possibility to have crystals of different sizes allows to use them in different photon energy ranges. Despite these useful characteristics, radiation damage effects may be important and can cause reduction of transparency due to color centers formation which absorb the scintillation light.

Semiconductor detectors such as high purity germanium or silicon are commonly used for energy resolved photon spectroscopy because of their excellent energy resolution combined with good efficiency.

Even for semiconductors the radiation damage effects are a limiting factor for their routine use for the RD configuration. Furthermore due to a small bandgap energy, these devices operate at low temperature in order to maintain a low leakage currents level. A different class of solid state detectors are the compound semiconductors such as Cadmium-Telluride (CdTe) and Cadmium-Zinc-Telluride (CZT). These materials are characterised by bigger bandgap energies (in the order of 1-2 eV) as compared to Ge and Si, allowing their room temperature operation. The greater atomic numbers provide an higher photoelectric absorption probability and a higher efficiency for high energy $\gamma^{'}$s with respect to intrinsic semiconductors.

The experiments devoted to test the RD configuration on VESUVIO have been performed employing both inorganic scintillators (sodium-iodide and yttrium-aluminum-perovskite) and compound semiconductor detectors (CdZnTe). In Chapter 4 brief descriptions of the specific detectors employed are made.

3.4 Considerations on the detection efficiency for the RD configuration

The RD counting efficiency is mostly independent of neutron energy, differently from what happens in the RF configuration, and it will be shown, from an experimental point of view, in the next Chapter.

This feature can be explained on a physical ground by referring to the simplified picture shown in Figure 3.4. It is well known that transitions probabilities

Figure 3.4: schematic picture describing primary and multi-step radiative transitions following resonance neutron capture

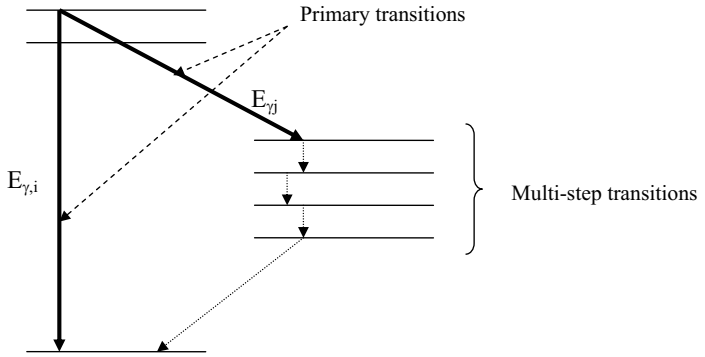

from states that are excited by the neutron capture, to different final states depend on the incoming neutron energy, the corresponding primary γ emission width, $\Gamma_{\lambda f}$, following a Porter-Thomas distribution [109]. The secondary transitions, however, proceed from states that are fed by *multi-step* transitions from the capturing state, and are less dependent on neutron energy. Indeed, the spectrum of low energy transitions is largely independent of capturing states for target spin $I = 0$ and s-wave neutrons. This argument is made

plausible by considering that low energy lines represent depopulation of levels that are fed by many transitions; hence, their distribution is characterised by a variance $\frac{2}{\nu_{eff}}$, ν_{eff} being the effective number of contributing channels, which for a heavy nucleus such as ^{238}U is in the order of several hundreds. In such a case the line strength is closely proportional to the capture cross section. The appreciable fluctuations of the relative intensity with incoming neutron energy of the primary γ transitions [112] do not appreciably affect the detection efficiency as the counting is provided by an integrated detection over a wide energy range, where secondary *multi-step* transitions are highly predominant. The efficiency η_d can be affected by the self-absorption of the γ-rays within the analyser. This effect depends on the γ energy and is negligible, at a first approximation, due to the small thickness of the foils (in the order of few tens of microns, depending on the resonance cross section) and to the high energy of the $\gamma^{'}$s (from few hundred of keV to MeV).

To estimate the detection efficiency η_d, let consider a simplified situation, sketched in Figure 3.5. In the figure n represents a scattered neutron of energy $E = E_r$ impinging normally to the analyser foil surface of thickness t. In a first order approximation (single neutron interaction) the neutron is absorbed after travelling a distance x into the analyser. At the absorption point a single γ-ray of energy E_γ is promptly emitted and may be enter into the photon detector, placed very close to the analyser. In a very simple way it can be argued that the detection probability is given by $\eta_d = P_n(E_r) \cdot \overline{P}_\gamma(E_\gamma) \cdot I_r(E_\gamma) \cdot \varepsilon_d(E_\gamma)$, where $P_n(E_r)$ represents the neutron absorption probability in the analyser, $\overline{P}_\gamma(E_\gamma)$ is the escape probability for the γ-ray, $I_r(E_\gamma)$ is the relative intensity of the γ line and $\varepsilon_d(E_\gamma)$ is the detector efficiency for the line E_γ. The overall detection efficiency can be written, with the very simple assumption described

Figure 3.5: Illustration describing the variables employed to evaluate the detection efficiency of a RD, in the simple case of normal incident neutrons onto the analyser and forward emission of photons toward the detector

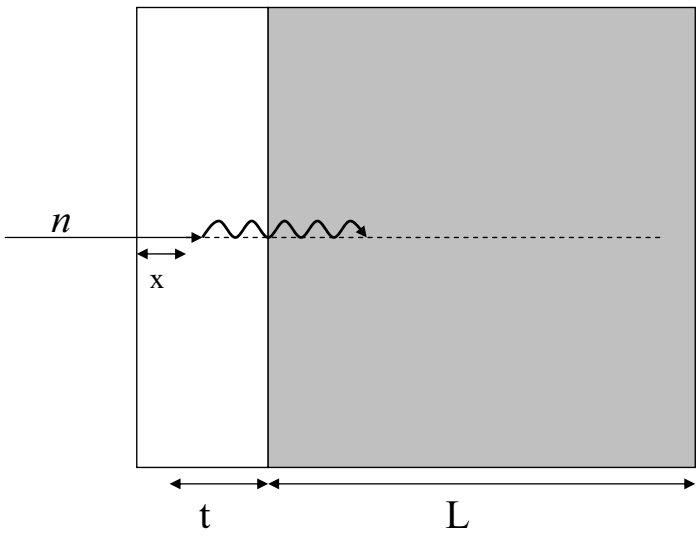

above, as:

$$\eta_d = I_r(E_\gamma) \cdot \varepsilon_d(E_\gamma) \cdot 0.5 \int_0^t \frac{1}{\lambda_n(E_r)} \cdot exp[-\frac{x}{\lambda_n(E_r)}] \cdot exp[-\frac{t-x}{\lambda_\gamma(E_\gamma)}] \cdot dx \quad (3.5)$$

where integration over x indicates that the escaping probability of the photon depends on the absorption point of the neutron, while the 0.5 factor takes into account the geometrical efficiency due to forward γ emission. The result, after simple integration calculations, is:

$$\eta_d = \frac{e^{-\frac{t}{\lambda_\gamma(E_\gamma)}}}{\lambda_n(E_r)} \cdot \{\frac{\beta^2}{\widetilde{\lambda}} \cdot [e^{\frac{\widetilde{\lambda}}{\beta^2}} - 1]\} \cdot I_r(E_\gamma) \cdot \varepsilon_d(E_\gamma) \quad (3.6)$$

In Equation (3.6) $\lambda_\gamma(E_\gamma)$ is the attenuation length for the γ in the analyser, $\lambda_n(E_r)$ is the interaction length for the resonant neutron in the analyser, $\beta^2 = \lambda_\gamma(E_\gamma) \cdot \lambda_n(E_r)$ and $\widetilde{\lambda} = \lambda_\gamma(E_\gamma) - \lambda_n(E_r)$. In order to make a numerical

evaluation of the detection probability, let consider a neutron energy of 6.671 eV and a ^{238}U analyser, assuming that a 138 keV γ-ray (see Fig. 3.2) is emitted. In this case the $\lambda_n(E_r) \simeq 30$ μm, while $\lambda_\gamma(E_\gamma) \simeq 160$ μm. Considering a relative intensity $I_r(E_\gamma) = 0.65$ and a detector efficiency $\varepsilon_d(E_\gamma) = 1$ a value $\eta_d \simeq 0.18$ is obtained. This calculation does not take into account the whole isotropic γ-ray cascade and the homogenous distribution of scattered neutrons onto the analyser$^{'}$s surface, however gives an order of magnitude for η_d. Despite the very raw assumptions it can be argued that, due to the difference between $\lambda_n(E_r)$ and $\lambda_\gamma(E_\gamma)$, the self-absorption probability is not a dominant effect, being in the order of 12% for a 138 keV γ-ray in uranium.

By varying the neutron resonance energy, the radiative capture cross section also varies and thus the penetration depth of the neutron in the analyser. Anyway by properly tuning the analyser thickness to the cross section intensity, and considering that the γ emission is mostly independent of neutron energy, a neutron energy independent η_d is obtained.

3.5 Description of the data acquisition electronics

The standard data acquisition electronics (DAE) operating on VESUVIO for TOF spectra recording is common to RD and RF set up and is described in the following.

The standard electronic chains for standard TOF measurements in the RF (upper chain) and RD (lower chain) configurations are schematically drawn in Figure 3.6. The overall electronics can be divided into three main parts: the

Figure 3.6: schematic of the RF (upper) and RD (lower) electronic chains

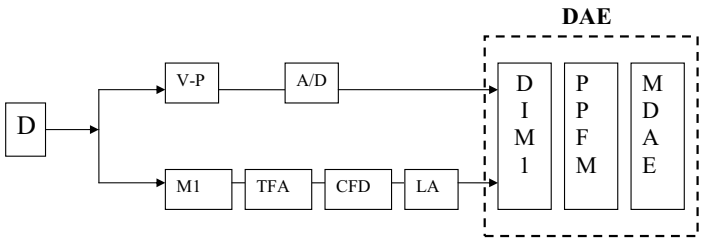

detector and its electronics, the signal processing electronics and the DAE.

For the upper chain (RF configuration) D represents a ^{6}Li-glass scintillation medium, connected to a Photomultiplier tube (PMT) by means of a light guide. The first electronic component (V-P) is the voltage divider and the preamplifier. The voltage divider provides the correct high voltage to the PMT dynodes, while the preamplifier is used before sending the signal to the cable reducing the effect of noise pick-up. The second electronic component is made of an amplification-discrimination stage. The amplifier also integrates the signal and makes it smoother. Then it is sent to the discriminator/comparator which generates a digital signal for the DAE, indicating that a neutron has been detected, if the signal is above the discrimination level.

For the lower chain (RD configuration), where a scintillator or a semiconductor detector can be used as γ detectors, the first electronic component (M1) may be composed by a voltage divider and a preamplifier (for a scintillator connected to its PMT) or by a high voltage module and a preamplifier (for the semiconductor detectors). The electronic chain for signal processing is composed by a Timing Filter Amplifier (TFA), a Constant Fraction Discriminator (CFD) and a Level Adapter (LA). These modules provide a fast signal

processing for the TOF acquisition.

The DAE is made of three main modules (see Figure 3.6): the DIM1, the Ping Pong Frame Memory (PPFM) and the main DAE crate (MDAE) and it can be regarded as a multi-stop TDC. The start signal is provided the ISIS proton beam monitor, while the stop signals are given by the DIM1 modules. The DIM1, performing the so called *time-stamping*, is the input unit of the DAE. It has 8 separate inputs and a clock which is cleared (reset) at the t_{start} pulse. If there is a signal at the input of the DIM1 (detection of a neutron), the time indicated by the clock is stored in a local memory, called the FIFO (First In First Out). This FIFO is a buffer and can hold a certain number of events without loosing data, but when the memory is full, it simply can store new events and data is lost. After storing the data into the FIFO, the DIM1 sets a flag to indicate the DAE main crate that it has data. The PPFM reads data from the DIM1 units that are connected to the different detectors, following a fixed order called priority. Data is stored in one half of PPFM memory (frame) and at the arrive of a new stop signal, PPFM stores the new DIM1 data in the second half of its memory while sending data from the first half to the DAE main crate.

The DAE accepts many stop pulses per start pulse for all the detectors and builds the TOF spectra by means of a big "histogramming" memory, which can be seen as a two dimensional array with the spectrum number on the x-axis and the TOF bins on the y-axis.

Due to the high count rates, saturation effects could be present. There are three reasons for DAE saturation to occur. First a FIFO of a DIM1 can be full because the data transfer between the DIM1 and PPFM is too slow. This saturation produces pronounced drops in the TOF spectra at early times (high

rate). The saturation can also vary a lot from detector to detector, depending on the priority and size of the FIFO memory. The second possibility for saturation to occur is when the data storage area of the PPFM is full. If this happens, the dashboard will increment the false frame count and all the data of the whole frame is lost. A third reason for saturation is when the main DAE crate does not have enough time between two frames to read all the data from the PPFM. The maximum data rate for this transfer it has been measured to be 1 MHz.

3.6 TOF spectra in the RD configuration

The experimental signal recorded in the RD configuration is a TOF spectrum, representing the number of counts collected in a time channel of width δt centered in t. It can be shown that the exact expression for the count rate per time bin [113] can be approximated, with good degree of accuracy, by the simple expression [76]:

$$C(t) = A(E_0, L_0, L_1)\delta t N_s \frac{d^2\sigma}{d\Omega dE_1}\Delta E_1 \eta_d \tag{3.7}$$

where N_S is the number of scattering centers in the sample, $\frac{d^2\sigma(E_0,E_1,\vartheta)}{dE_1 d\Omega}$ is the sample's double-differential scattering cross section, ΔE_1 is the total width of the nuclear resonance and η_d represents the overall detection efficiency.
The quantity $A(E_0, L_0, L_1)$ is given by:

$$A(E_0, L_0, L_1) = \frac{\phi(E_0) A_d E_0^{3/2}}{L_0^3 L_1^2 4\pi} 2\sqrt{\frac{2}{m}} \tag{3.8}$$

where $\phi(E_0)$ is the spectrum of the incident neutrons at the energy E_0, A_d is the analyser$'$s foil area which determines the geometrical acceptance of the

detector. L_0, L_1 are the primary and the scattering flight paths respectively, while m is the neutron mass.

As already quoted in Chapter 2, the double differential scattering cross-section is related to the dynamic structure factor $S(\overrightarrow{q},\omega)$ via eq. (2.18). Due to the large values of wavevector and energy transfers accessed in the DINS measurements presented in Chapters 4 and 5, the experimental data have been analysed within the IA framework [1,93]. When in the IA regime, the dynamic structure factor is related to the single particle momentum distribution, $n(\overrightarrow{p})$, by eq. (2.19) [93]. The $n(\overrightarrow{p})$ is usually expressed in terms of the West scaling variable y, defined by eq. (2.20), introducing the longitudinal Compton profile $J(y)$ (see eq. (2.23)). From the definition of $J(y)$ the experimental response function for one detector can be formally approximated by the convolution:

$$F(y) = J(y) \otimes R(y) \tag{3.9}$$

where $R(y)$ is the overall spectrometer$'$s resolution function. In terms of $J(y)$ and $R(y)$, the count rate per time bin of eq. (3.7) can ultimately be written, for a single recoiling mass, as:

$$C(t) = A(E_0, L_0, L_1)\delta t \Delta E_1 \Delta\Omega N_s b^2 M J(y) \otimes R(y) \tag{3.10}$$

Thus from a collected TOF spectrum in the RD configuration it is possible, through a TOF $\mapsto y$ mapping procedure, to obtain $F(y)$ for each detector and hence $J(y)$. From the Compton profile the momentum distribution can be obtained by:

$$n(p) = [-\frac{1}{2\pi y} \cdot \frac{dJ(y)}{dy}]_{y=p} \tag{3.11}$$

while the mean kinetic energy can be calculated by calculated through eq. (2.24).

For HINS measurements the TOF spectrum is represented by eq. (3.7) and through a TOF $\mapsto \omega$ mapping procedure, the dynamic structure factor for each fixed-angle detector, $S(\vartheta, \omega)$, is obtained, allowing to achieve information on the spectrum in the $q \leq 10$ Å^{-1}and $\omega \geq 1$ eV range, typical of the HINS regime.

Chapter 4

Experiments with γ detectors

The aim of this Chapter is to present the experiments carried out on eVS and VESUVIO spectrometers to test the RD configuration, employing different γ detectors and analyser foils.

4.1 Experiments with a Sodium Iodide scintillator

This section is dedicated to the discussion of the first detector test, performed on eVS spectrometer, employing a sodium-iodide (NaI) scintillator and uranium analysers [53].

Thallium doped sodium-iodide, NaI(Tl), is the most widely used scintillation material. NaI(TI) is used traditionally in nuclear medicine, environmental measurements, geophysics, medium-energy nuclear physics. The greatest light output among scintillators, convenient emission range coincident with the maximum efficiency region of photomultiplier (PMT) with bialkali photocathodes,

the possibility of large-size crystals production, and their low prices compared with other scintillation materials compensate to a great extent for the main NaI(TI) disadvantage, namely, the hygroscopicity, on account of which NaI(TI) can be used only in hermetically sealed assemblies. The general characteristics of NaI(Tl) are listed in Table 4.1

Table 4.1: main physical characteristics of NaI(Tl) scintillator

Effective atomic number	50
Density ($\frac{g}{cm^3}$)	3.67
Melting point (°C)	651
Maximum emission (nm)	410
Refractive index at λ_{max}	1.85
Light yield ($\frac{photons}{MeV}$)	4 10^4
Decay time (ns)	230
Hygroscopic	yes

4.1.1 DINS measurements

The detector test with NaI(Tl) has been carried out during DINS experiments on a polycrystalline Pb sample (100 cm^2 area and 1 mm thickness) and on a $^4He - H_2$ mixture [53], employing the instrument set up shown in Figure 4.1. The NaI scintillator was a 3" × 3" cylindric crystal and was placed at a scattering angle $\vartheta \simeq 38°$, at a distance of about 60 cm from the sample. Two different uranium foils have been used, namely 10 cm × 10 cm × 30 μm and 10 cm × 10 cm × 120 μm, in order to perform both single and double difference measurements (SD and DD, see Section 2.4.1). Due to the heavy γ and neutron background contamination, shielding was needed around the detector. The shielding consisted of lead blocks (5 cm thick) placed around the detector assembly and borated wax (15 cm thick) on the outside. Lead

Figure 4.1: Experimental set up for the DINS experiment on a Pb sample in the RD configuration on eVS.

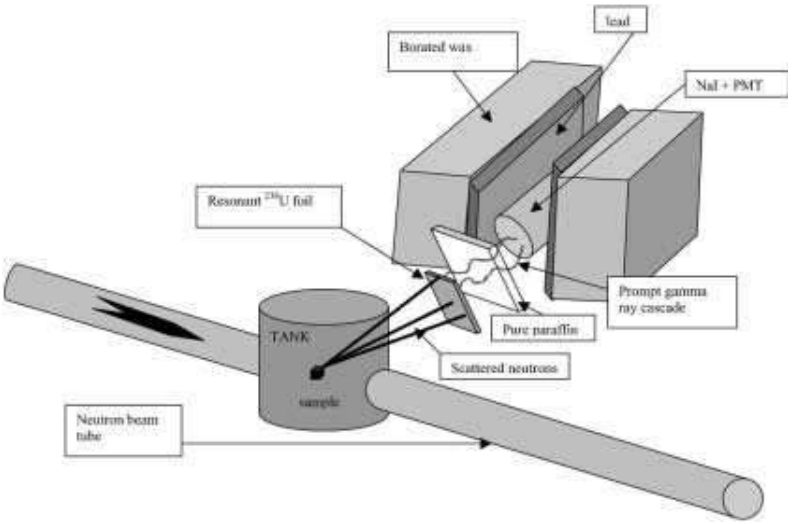

blocks were used to shield the scintillator from the γ rays produced by (n,γ) reactions in the borated wax around the detector and on the walls of the experimental hall (isotropic background). Due to the presence of elements such as the isotopes of the antimony (in the lead) and the isotopes of the iodine (in the scintillator), which have neutron resonances in the range 1-100 eV, a paraffin slab ($15 \times 15 \times 5$ cm^3) was placed between the analyser and the detector. The paraffin front shield was effective in attenuating the direct epithermal neutron flux onto the detector and lead shield, allowing for the suppression of the resonant neutron absorption peaks coming from iodine and impurities present in the Pb shield and the NaI scintillator (see fig. 4.2). In parallel to DINS measurements in the RD configuration, measurements

Figure 4.2: Background spectra for a Pb sample recorded with a NaI scintillator under different shielding and energy discrimination conditions. The open circles correspond to the case where a front paraffin shielding and a 0.8 MeV discrimination threshold have been used. No front shield and no discrimination correspond to full circles.

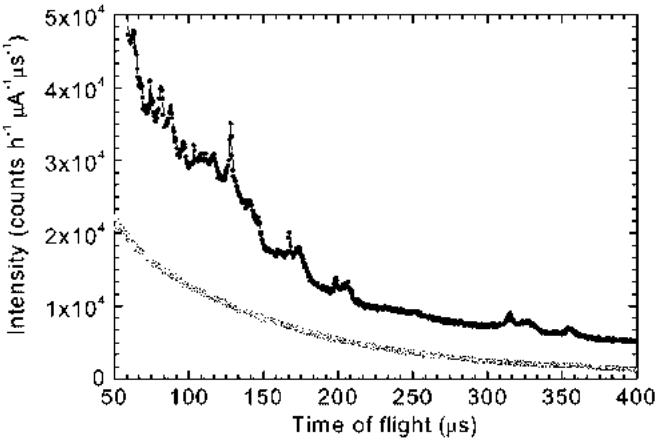

employing the standard RF configuration have been carried out employing the electronic set up shown in Figure 3.6.

4.1.2 Results for Pb sample

Referring to [53] for the description of data reduction and analysis, here the main results are presented. First of all, it is interesting to compare the background sensitivity of the NaI scintillator with that of the conventional ^{6}Li-glass scintillator. In Figure 4.3 the normalised TOF spectra from the Pb sample are shown for NaI and ^{6}Li-glass, using the same 30 μm thick uranium foil. The peak (top) and the dip (bottom) are associated to the Pb recoil peak measured at the final neutron energy of 6.67 eV (^{238}U resonance). The peak intensity

is lower in the NaI case, indicating a lower overall efficiency due to the non optimised detector set-up. More interesting is the signal to background ratio, which is similar in the two spectra. It has to be stressed that the continuous line in the upper spectrum of fig. 4.3 is a guide for the eye, describing the γ background level shown in fig. 4.2 (open circle), while the continuous line in the lower spectrum of fig. 4.3 shows the *foil-out* scattering spectrum. An

Figure 4.3: Neutron TOF spectra from a Pb sample recorded using a 30 μm thick uranium foil in the experimental set-up of Figure 4.1. The NaI spectrum (top) has a peak corresponding to the Pb recoil peak at a final neutron energy of 6.67 eV. The same resonance gives rise to the absorption dip in the ^{6}Li-glass spectrum (bottom).

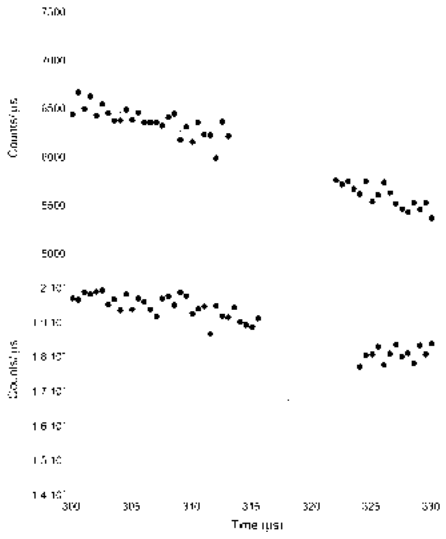

example of the resulting (background subtracted) TOF spectra from Pb are shown in Figure 4.4 for the case of a 30 μm ^{238}U foil, for both the NaI and the ^{6}Li-glass detectors. Both spectra are normalised so that the area under the 6.67 eV peak amounts to one count. In fig. 4.4(a) additional peaks are

Figure 4.4: (a) Background corrected TOF spectrum from Pb recorded by the NaI with a 30 μm ^{238}U foil. The spectrum is normalised so that the area under the 6.67 eV peak amounts to one count; (b) Same as (a) but recorded by the ^{6}Li glass scintillator. Normalisation is the same as for case (a).

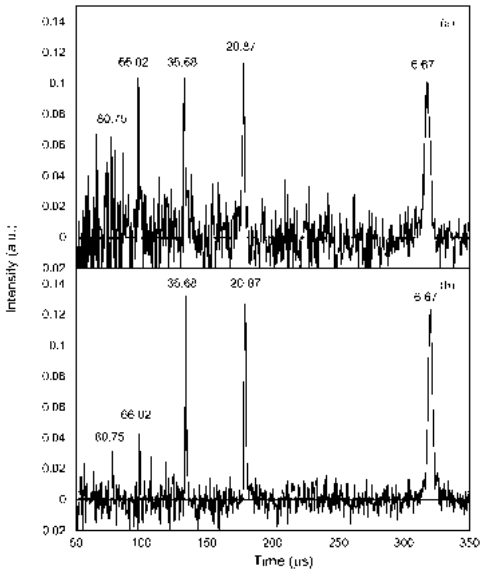

clearly visible, corresponding to scattering signals from Pb recoil at final neutron energies defined by the higher ^{238}U resonances, *i.e.* 20.9, 36.7, and 66.0 eV [114]. Above 80 eV the statistical noise is too large and the identification of additional peaks is not possible. The area under the peaks decreases with increasing resonance energy; it is only 0.20 at 66.0 eV. In fig. 4.4(b) the time of flight spectrum recorded by the ^{6}Li-glass scintillator shows a stronger decrease of peak intensities with increasing resonant energy: the area under the 66.0 eV peak is only 0.08, *i.e.* about 2.5 times lower, in relative terms, than the corresponding peak in the NaI spectrum. This is mainly due to the inverse velocity dependence of the ^{6}Li neutron absorption cross section.

From the collected TOF spectrum (fig. 4.4), which represents the count rate per time bin, it is possible to extract the information on the Compton profile $J(y)$ as already explained in Section 3.6. A standard calibration procedure [115] allowed the transformation of $C(t)$ given by eqs. (3.7) and (3.10) into $F(y)$ (see eq. (3.9)).

The experimental response function $F(y)$ corresponding to the recoil peak at $t \simeq 320$ μs in fig. 4.4 is plotted in Figure 4.5. TOF spectra have also been

Figure 4.5: Experimental response function $F(y)$ from the NaI scintillator for the 30 μm uranium foil for a final neutron energy of 6.67 eV. Continuous line is the Voigtian fit.

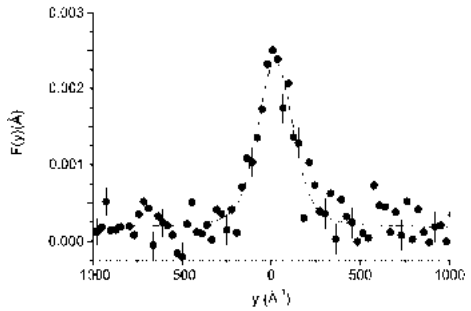

collected with the 120 μm thick ^{238}U foil in order to apply the DD method (see Section 2.4.1). In Figure 4.6 (a) the experimental response function $F(y)$ obtained through SD and DD methods are shown, while in fig. 4.6 (b) the corresponding voigtian fits and the theoretical Pb Compton profile $J(y)$ are shown. The $F(y)$ functions were fitted (see continuous and dashed lines in Figure 4.6(b)) by a profile given by the convolution of the function $J(y)$ with the Voigt instrument resolution profile, $R(y)$, using a normalisation factor as a free parameter. In Figure 4.7 (a) the open circles represent the $F(y)$ ob-

Figure 4.6: (a) Experimental response function $F(y)$ from the NaI for the 30 μm uranium foil at a final neutron energy of 6.67 eV obtained through the Single Difference (full dots) and Double Difference (open dots) methods. (b) Dashed line is the fit to the SD $F(y)$, continuous line is the fit to the DD $F(y)$, dotted line is the Compton profile $J(y)$ of the Pb sample.

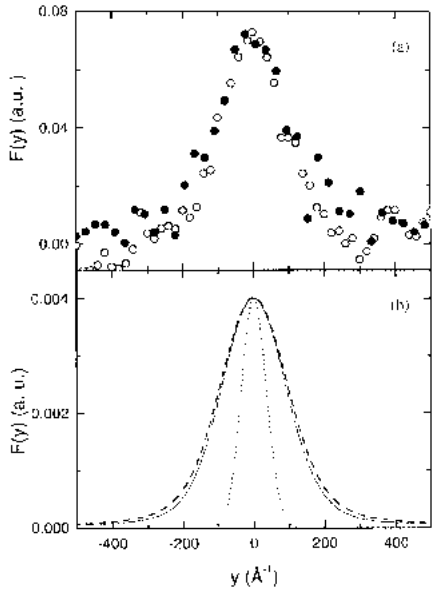

tained with thick analyser, the triangles represent the $F(y)$ obtained with the thin analyser and the full dots represent the $F(y)$ obtained applying the DD method. In fig. 4.7 (b) the corresponding voigtian fits are shown. In this figure it is well visible the enhancement of the resolution and an appreciable reduction of the lorentzian tails as already discussed in Section 2.4.1. In figure 4.7 (c) the same plot of fig. 4.5 is shown for a more direct comparison.

Figure 4.7: (a) TOF spectra from NaI in the 6.67 eV peak region acquired with thin foil (triangle), thick foil (open circle) and DD (solid circle). The spectra are normalised so that their gaussian fits have unit intensity (height); (b) Voigt curves fitting the spectra in (a), *i.e.* thin foil (continuous line), thick foil (dashed line) and DD (dotted line). (c) Thin foil spectrum in (a) fitted with a Voigt lineshape (continuous line from (b)).

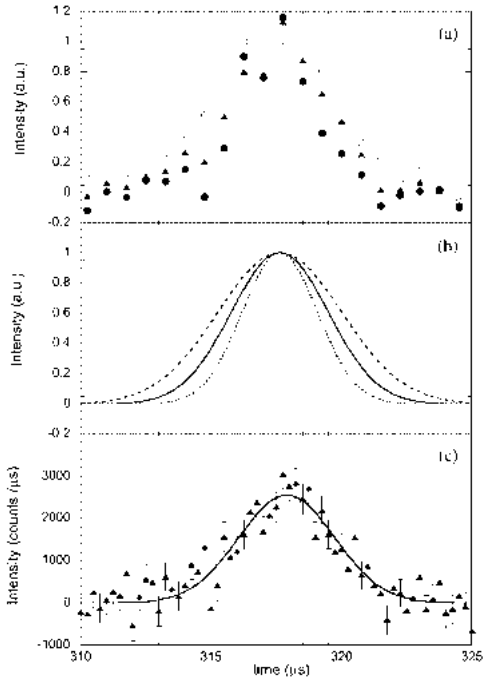

4.1.3 Monte-Carlo simulation

In order to test the effectiveness of a complete DINS experiment on eVS, starting from the instrument configuration up to the data acquisition and analysis, a simulation of the experiment with NaI(Tl) has been carried out using a Monte-

Carlo approach. The Monte-Carlo code employed for the simulation has been properly developed starting form the DINSMS code described in [116]. This code was specifically developed to simulate the performance of the eVS spectrometer for DINS from condensed matter, and has been successfully applied to evaluate single and multiple scattering contributions from solid samples in conventional SD experiments. In the original version, DINSMS code simulates only an inverse geometry RF spectrometer, taking into account the specific features of neutron source, filters and detectors of eVS and assumes the scattering process to be described within the framework of the IA.

In the new Monte-Carlo code, the original neutron detection process through ^{6}Li-glass has been substituted, accounting for the γ-ray production in the absorber and photons detection by means of the NaI(Tl) scintillator.

The output of the Monte-Carlo is a TOF spectrum corresponding to a detector at a fixed secondary flight path and scattering angle and for a well defined analyser foil thickness (all these parameters are known from the experimental set up). As far as the signal intensity is concerned, a unitary and energy independent efficiency for the γ cascade production was assumed, so that the number of produced cascades equals the number of scattered neutrons absorbed in the ^{238}U foil. This assumption is reasonable, considering that the radiative channel branching ratio is the highest around E_r and that it varies less than 5% within the width of the resonance, $2\Gamma_0 \simeq 50$ meV at room temperature, as shown in Figure 4.8. The correct count of the absorbed neutrons number depends on the number of γ cascades effectively revealed by the scintillator and then on the efficiency $\eta(E_\gamma)$ of the NaI (E_γ being the γ energy). In this context, as no γ spectroscopic investigation was needed, the scintillator has been considered as a calorimeter, so that the mean total energy

Figure 4.8: Branching Ratio (BR) of the radiative channel in an energy interval centered around the ^{238}U resonance at 6.67 eV.

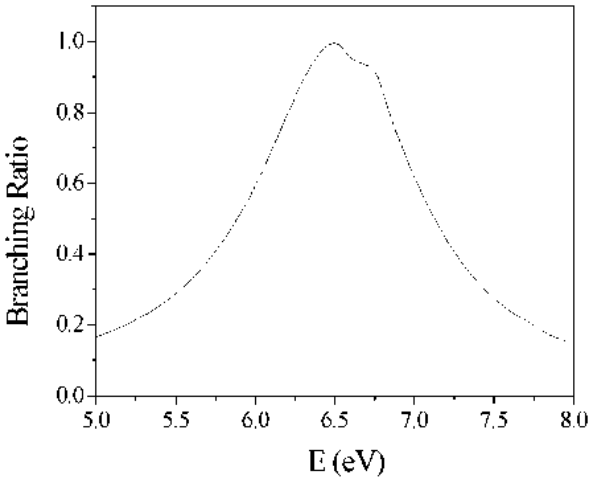

deposit of each cascade within the detector volume is the important quantity for the complete determination of the number of absorbed neutrons. In our simulation a constant effective efficiency, $\eta = 1$; has been considered. In fact, any proportional change in the number of scintillation photons produced in the NaI(Tl), would result in a scale factor in the final TOF spectrum, without changing the lineshape. This can be originated by a partial detection of the γ cascade energy deposit, resulting from an energy-dependent detector efficiency $\eta(E_{\gamma,i})$ or a finite size detector geometrical acceptance. The neutron TOF from the moderator to the ^{238}U foil has been determined by using the γ detection as stop signal, assumed coincident with neutron absorption in the analyser foil (reasonable assumption, since the γ cascade is prompt). An overall time offset $t_{off} \simeq 1$ μs, mostly due to the acquisition electronics (NaI-Photomultiplier

tube-transmission cables, electronic modules-computer) has been introduced. In Figures 4.9 and 4.10 the SD and DD recoil spectra for lead, both simulated (continuous line) and experimental (open dots), obtained with a ^{238}U foil at room temperature are shown in the TOF region corresponding to 6.67 eV scattered neutrons. In both cases, the simulated data have been corrected for an estimated time offset of 1 μs due to the signal processing electronics. As it can be argued from these figures, the agreement between experimental data and simulations appears satisfactory, in spite of the low data statistics.

Figure 4.9: Simulated (full line) and experimental (open circles) SD recoil spectra of Pb relative to the 6.67 eV resonance of the ^{238}U analyser at room temperature.

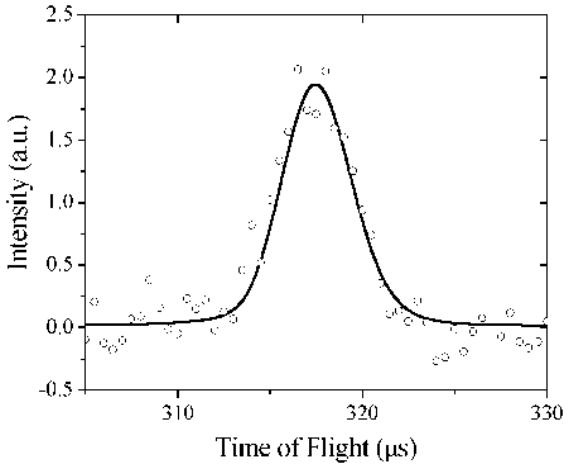

Figure 4.10: Simulated (full line) and experimental (open circles) DD recoil spectra of Pb relative to the 6.67 eV resonance of the ^{238}U analyser at room temperature.

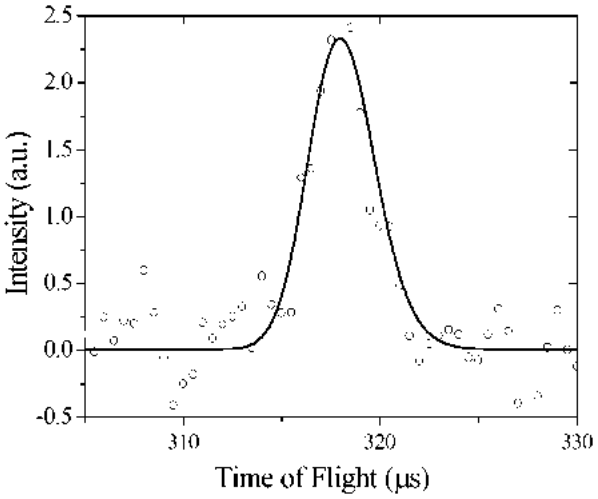

4.1.4 Results for $^4He - H_2$ mixture

Neutron TOF spectra from a $^4He - H_2$ mixture were recorded using both a thin and thick ^{238}U foil, as a test of the performance of the present RD apparatus for samples of low atomic mass. An independent measurement of the background signal, with *foil-out*, was also performed. In Figure 4.11(a) and (b) the *foil-in* signal and the background-corrected spectra are shown. From Figure 4.11(b) it can be seen that the relevant scattering from hydrogen and sample container (aluminum) occur in the TOF region $t \leq 325$ μs. In Figure 4.11(c) ratio of the $foil - out$ spectrum (fig. 4.11(b)) to the signal spectrum (fig. 4.11(a)) is also shown. The narrow peaks in fig. 4.11, due to neutrons scattered from the Al sample holder, are marked in the figure by

Figure 4.11: (a) Neutron TOF spectra from a 50% $^4He-H_2$ mixture measured with 120 μm thick ^{238}U foil; (b) difference spectrum; (c) ratio of the difference spectrum (b) to the spectrum in (a).

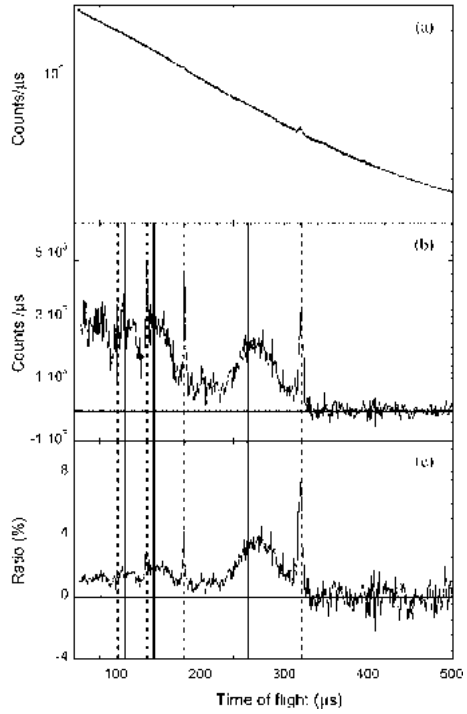

dashed lines. The recoil peak at a final energy of 6.67 eV (t = 320 μs) can be clearly identified, while the other H peaks coming from the higher ^{238}U resonances are less defined. Due to the poor statistics, the non optimised set up and to the smaller scattering cross section, the ^{4}He recoil peak, expected at an intermediate TOF, is not observed. For this sample the analysis in y space performed for lead was not attempted.

The results obtained from this first test provided a useful empirical basis for ongoing investigations of the RD configuration using different combinations of

analyser foils and γ detectors in order to exploit the RD in the neutron energy range 10-100 eV.

The background sensitivity of a big detector such as the NaI employed for the test, indicated to consider smaller detectors which, however, can only detect low energy γ with adequate efficiency.

4.2 Experiments with a Cadmium-Zinc-Telluride semiconductor detector

This section is dedicated to the presentation of the experimental results obtained during tests on Cadmium-Zinc-Telluride (CZT) semiconductor detectors [55].

Commercially the ternary semiconductor compound $Cd_{1-x}Zn_xTe$ has a blending fraction x of $CdTe$ in $ZnTe$ [117] ranging between 5% and 13%. This corresponds to an energy band gap of 1.53 eV and 1.48 eV, respectively. The high band-gap values determine a low leakage-current level, thus allowing room-temperature operation [118]. The ability to operate at room temperature without the need for liquid nitrogen cooling, allows the construction of compact devices. The resolution of CZT is intermediate between scintillators and germanium devices. Recent advances in the understanding of crystal growth and detector fabrication using CZT hold the promise of providing low cost high resolution detectors. CZT detectors can be fabricated into a variety of shapes and sizes making it possible to produce detectors capable of meeting the requirements of a wide assortment of applications unsupported by the other detector types.

4.2.1 DINS measurements

In order to test the performances of the CZT detectors for the RD configuration, a DINS experiment has been carried out on VESUVIO. For this measurement, a slab-shaped Pb (10×10 cm^2 and 1.0 mm thick) was placed at the sample position, while a ^{238}U analyser foil, with 10×10 cm^2 area and 50 μm thickness, was attached outside the lateral flange of the VESUVIO sample tank and both ^{6}Li and CZT detectors were placed with their axis perpendicular to the foil (Figure 4.12).

For this experimental test, two CZT detectors have been tested (labelled CZT1 and CZT2), having a crystal thickness of 2 mm and 5 mm, respectively (see Table 4.2). For both devices the efficiency for γ detection was estimated to

Table 4.2: main physical characteristics of the two CZT employed for DINS experiments on Pb

Characteristic	CZT1	CZT2
Producer	EURORAD	eV Product
Housing	Pure aluminium	Anodised aluminium
Size (mm^3)	$5 \times 5 \times 2$	$5 \times 5 \times 5$
Efficiency at 100 keV	86.5 %	99.3 %
Rise time (ns)	200	35
decay time (μs)	200	700
Energy resolution (FWHM) at 122 keV (keV)	6	4
Peak/valley	2	7

be 70% and 90% for energies around 130 keV, respectively [119]. In particular, the thicker crystal, CZT2, shows a better photon-energy resolution ΔE_γ (with $\Delta E_\gamma = 4$ keV at $E_\gamma = 122$ keV) coupled with a shorter rise time ($t_{rise} = 35$ ns).

Thus the experiment was intended to test the RD configuration employing

Figure 4.12: schematic of the experimental set up for the DINS experiment with CZT on VESUVIO

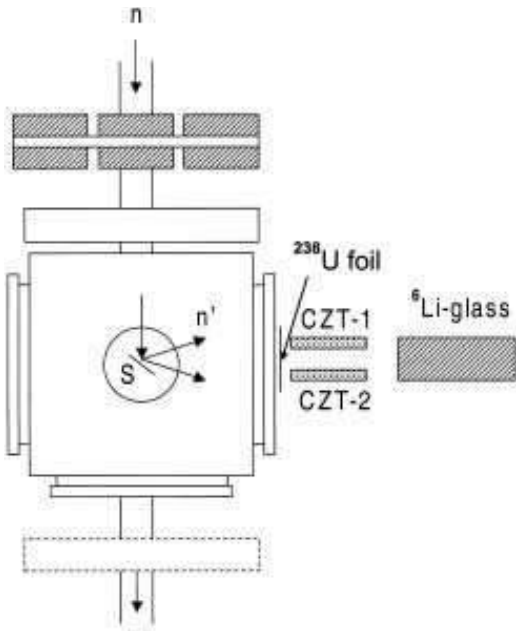

smaller detectors as compared to the NaI(Tl), detecting γ energies below 250 keV.

4.2.2 Results

In Figure 4.13 the experimental DINS signal, collected with CZT1 from the polycrystalline Pb sample, is shown in the whole TOF for a total integrated proton current of about 5000 μAh. Below 1200 μs the Pb recoil peaks can clearly be identified. The plot on the top right side of fig. 4.13 is a blow-up of the time spectrum in the range 2000 μs $\leq t \leq$ 18000 μs. Due to the pulsed nature of the neutron source, epithermal neutrons reach the analyser foil within

Figure 4.13: TOF spectrum acquired with CZT: the insert is a blow up of the very high TOF (thermal region)

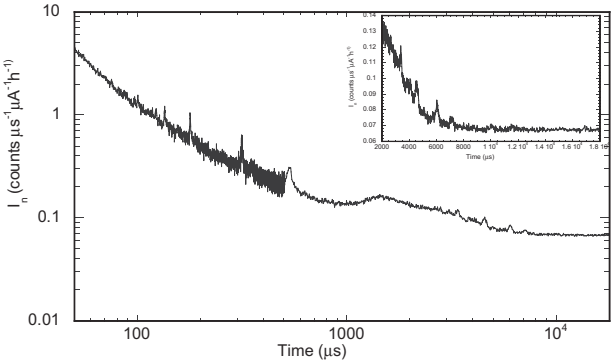

a time scale of about 0.1 ms, whereas thermal neutrons are detected in the active medium, via (n,γ) reactions in ^{113}Cd, on a time scale well in excess of 1 ms. Therefore this time separation is a key issue which allows the simultaneous detection of DINS and diffraction spectra with the CZT detector shown in fig. 4.13. Figure 4.14 shows the experimental signal from the Pb sample recorded with CZT1 (fig. 4.14(a)) and the corresponding *foil-in* spectrum recorded with the ^{6}Li-glass detectors (fig. 4.14(b)) in the TOF range 50 μs $\leq$ t $\leq$ 500 μs. The experimental signal for both detection systems in the time interval 2000 μs $\leq$ t $\leq$ 18000 μs is reported in Figure 4.15, and the diffraction pattern from the Pb sample can be appreciated. An estimate of the S/B ratio has also been carried out for the DINS spectra recorded with the two CZT$'$s and ^{6}Li-glass detector. This was accomplished by defining this ratio as the recoil peak area divided by the subtended area in the background measurement of figs. 4.13(a) and 4.13(b), respectively. The results are shown in Figure 4.16. Better S/B ratio is clearly found for both CZT detectors with respect to the ^{6}Li-glass

Figure 4.14: TOF spectra acquired with CZT (top) and ^{6}Li-glass (bottom)

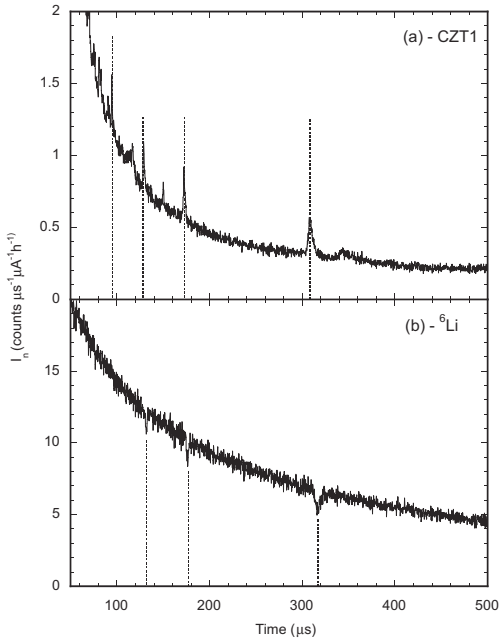

scintillators. In the case of the highest-energy resonance the ^{6}Li-glass data were of insufficient statistical quality to allow for a meaningful determination. The recoil scattering peaks for four different values of the final energy have been analysed in the IA framework (see Chapter 2). In the present measurements a total of four experimental response function $F(y)$ were analysed, for both CZT1 and ^{6}Li-glass detectors, employing four different final neutron energy values which correspond to the first four ^{238}U resonances, *i.e.* $E_r = 6.671$ eV, $E_r = 20.870$ eV, $E_r = 36.680$ eV, and $E_r = 66.020$ eV respectively. The four experimental $F(y)$ functions obtained through the CZT1 detector are reported in Figure 4.17. The experimental $F(y)$ functions were fitted individually with a non-linear least squares routine, using a Voigt model function plus a parabolic

Figure 4.15: diffraction patterns recorded by CZT (upper plot) and ^{6}Li-glass (lower plot)

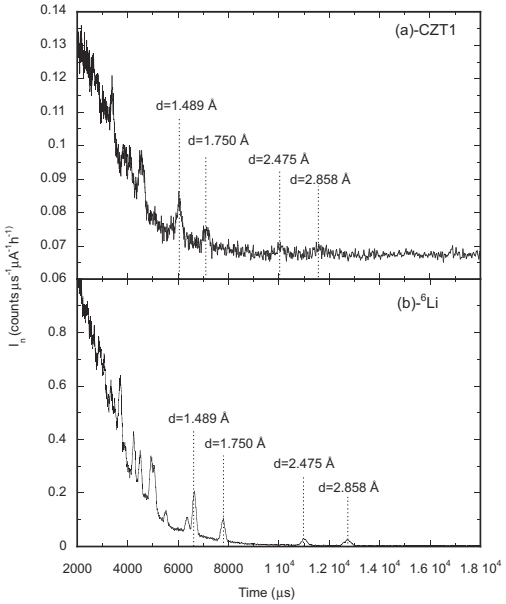

background. The $F(y)$ functions, resulting from the fitting procedure, are plotted as dashed lines in fig. 4.17 and the parameters are summarised in Table 4.3 together with the theoretical estimates [115]. Figure 4.17 shows that the DINS spectra recorded with the CZT1 detector can be satisfactorily analysed up to the final resonance energy $E_1 = 66.02$ eV. The results of the fit are in overall agreement with the estimated values, apart for the second recoil peak, corresponding to $E_1 = 20.87$ eV, which exceeds the theoretical σ_g value (see tab. 4.3). The same fitting procedure was also applied to the $F(y)$ functions obtained with the ^{6}Li-glass detectors, and the resulting parameters are reported in tab. 4.3. It can be noted that in this case only the analysis of the first two recoil peaks provides reliable σ_g values which well compare with

Figure 4.16: Values of the signal to background ratio for CZT1, CZT2 and ^{6}Li-glass measured for four Pb recoil peaks corresponding to the four uranium resonances

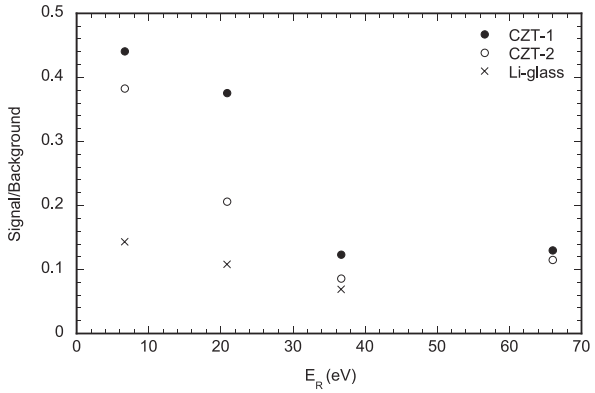

Table 4.3: Summary of the fitting results for the $F(y)$ obtained with RD and RF configurations

E_r [eV]	σ_g^{exp} CZT [Å^{-1}]	σ_g^{th} [Å^{-1}]	σ_g^{exp} ^{6}Li-glass [Å^{-1}]	σ_g^{th} [Å^{-1}]
6.6	39.6 ± 5.9	37.3	40.7 ± 2.4	45.6
20.8	78.8 ± 13.0	45.8	51.7 ± 14.2	54.2
36.6	85.1 ± 24.8	82.6	45.2 ± 30.8	73.3
66.0	102.6 ± 16.9	93.6	17.0 ± 1206.0	107.4

the theoretical estimates. This finding was expected given the poor ^{6}Li-glass detection efficiency for energies above 10 eV.

The most important improvement with respect to the first test with NaI was that the RD configuration with CZT is effective up to final neutron energies of about 70 eV with an improved S/B ratio, achieved without any shielding around the detection system. A clear indication was that the use of small volume detectors provide reduced background sensitivity and an improved signal detection efficiency by detecting γ energies below 250 keV.

Figure 4.17: Experimental response function $F(y)$ from CZT1 and corresponding Voigt fits, obtained through a simultaneous fitting procedure.

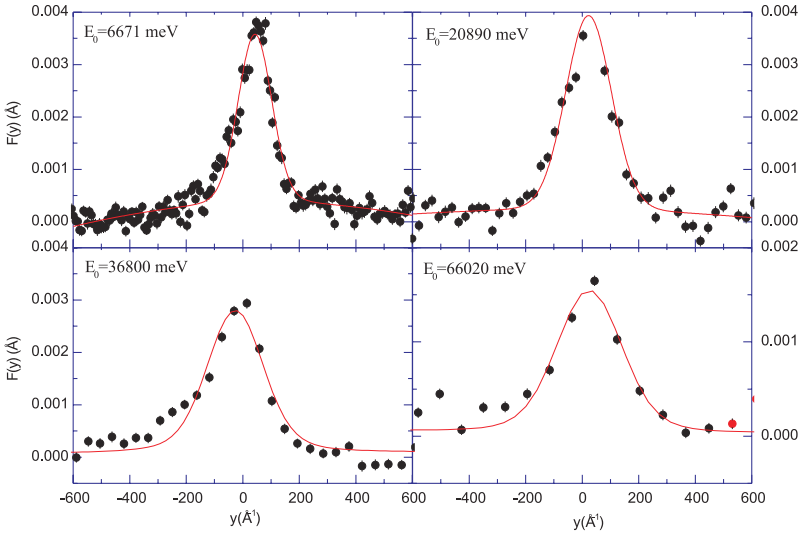

4.3 Biparametric measurements

After the DINS measurements, another experimental test has been carried out with CZT detectors in order to characterise their response to the prompt photon emission from both ^{197}Au and ^{238}U analysers. To this aim, the analyser was placed at the sample position and the CZT detector outside the aluminum tank in order to maximise the flux of neutrons onto the analyser and the solid angle for γ collection. The set up, slightly different from the one shown in Section 3.5, is shown in Figure 4.18. A dedicated data acquisition system was developed for the simultaneous measurements of the neutron TOF and pulse height (γ energy) spectra, by modifying the standard DAE. In order to obtain a suitable lineshape sampling of the TOF spectrum around the time positions of the different nuclear resonances, the time bin of the modified DAE has been

Figure 4.18: Experimental set up for the biparametric measurements

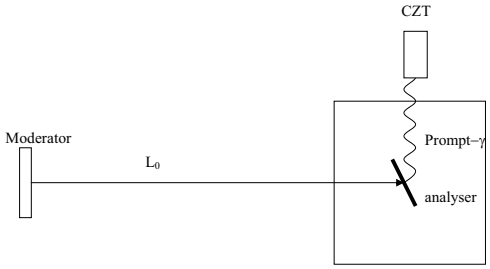

set with two different configurations. In the case of ^{238}U, data were collected with a 1 μs constant time bin to match the narrow intrinsic widths of the different resonances listed in tab. 3.2. In the case of ^{197}Au, broader resonances are expected and a 5 μs constant time bin was chosen. In both cases, data in the TOF region above 500 μs were recorded with a variable time bin. The main elements of the signal processing and data acquisition are sketched in Figure 4.19. The analog signal from the CZT was amplified and shaped by

Figure 4.19: electronic chain for biparametric acquisition

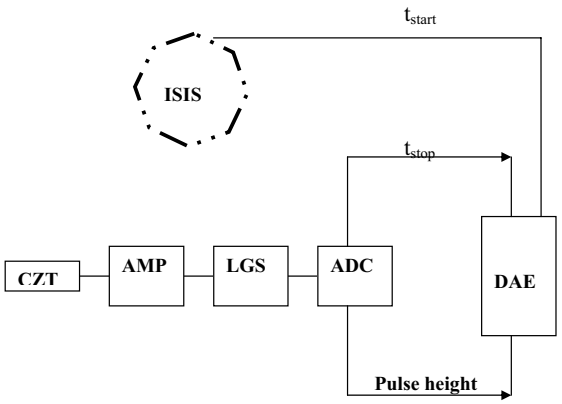

a spectroscopy amplifier (AMP). Further signal shaping was provided by a Linear Gate Stretcher (LGS) before sending the signal to a 12 bit Analog to Digital Converter (ADC), of the Wilkinson type, with up to 12 μs variable conversion time. The digital output from the ADC was fed into the modified DAE resulting in the biparametric measurement (TOF vs Energy).

The ADC conversion time depends on the pulse height of the analog signal, and the stop signal is not sent until the ADC has entirely processed. Thus the stop signal is delayed by the conversion time, $t(E_\gamma)$.

The biparametric data presented in this paper refer to two runs acquired with the CZT2 detector for 10 h (^{238}U) and 16 h (^{197}Au) at an average proton beam current of 180 μAh.

Typical raw biparametric spectra relative to the ^{238}U and ^{197}Au analysers are shown in Figures 4.20 and 4.21, respectively. These figures represent contour plots of signal intensity versus energy (x-axis) and neutron TOF, t_{exp} (y-axis). In fig. 4.20 the spectral intensity is shown from a threshold value of 10 counts in step of 5. The horizontal stripes, occurring at a well define time values, correspond to ^{238}U resonances. The effect of the γ energy dependent ADC conversion time results as a stripes tilting in fig. 4.20 (a). The effect can be corrected providing the plot in fig. 4.20 (b). Besides the mentioned neutron resonances, there is an intensity distribution corresponding to a broad range of neutron TOF and energies. This feature is related to the energy spectrum associated with the radiative capture of non-resonant neutrons, which arrive at all times. The bidimensional plots relative to the ^{197}Au analyser foil are shown in fig. 4.21, where the contour graphs are plotted from a threshold of 50 in steps of 50. In this case, the effect of the stripes tilting is much less evident due to the coarser time bin used (5 μs). The two visible horizontal

Figure 4.20: bidimensional contour plot of uranium

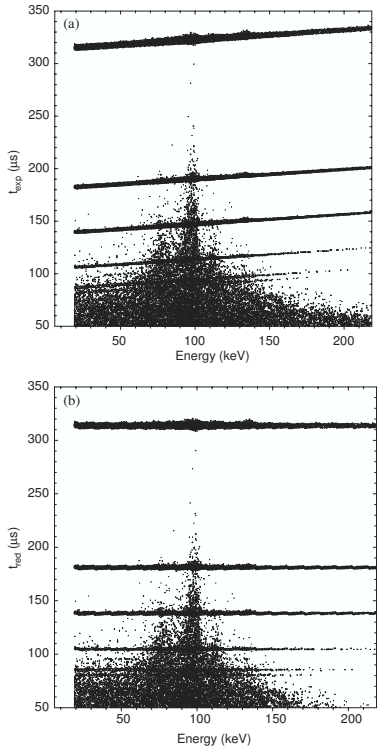

stripes correspond to the 4.906 and 60.3 eV neutron resonances.

In order to extract the information from the biparametric spectra, two different calibrations, namely energy and time calibrations, were performed for each chain of the biparametric signal processing and data acquisition system.

4.3.1 Energy calibration

Absolute calibration of the pulse height values recorded by the ADC in the biparametric data acquisition system was performed by measuring the spec-

Figure 4.21: Bidimensional plot of gold

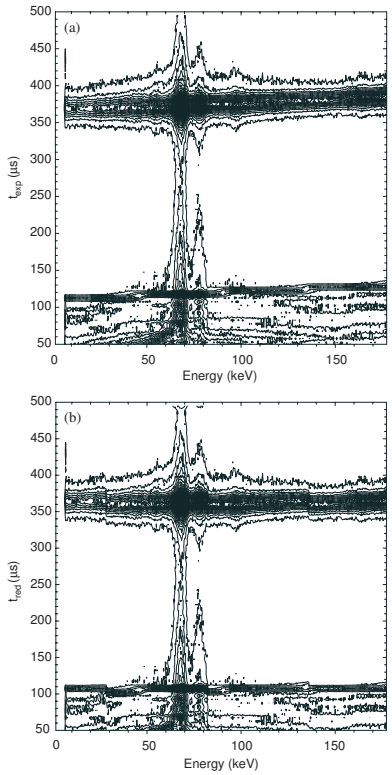

trum from a ^{57}Co source, which provides two well identifiable decay lines at 122 keV and 136 keV. An example of a ^{57}Co calibration spectrum acquired in the VESUVIO experimental hall is shown in Figure 4.22 for each CZT. The two highest energy peaks, present in both pulse height spectra, represent the ^{57}Co decay lines. The measured energy resolution at 122 keV, expressed as Full Width at Half Maximum (FWHM), is poorer for the CZT1 thin detector, (FWHM = 6 keV) than for the CZT2 (FWHM = 4 keV). It is also evident that the pulse height response of CZT1 degrades below about 100 keV, where the spectrum shows a low peak to valley ratio and a pronounced low energy tail.

Figure 4.22: calibration spectra of ^{57}Co acquired with CZT1 and CZT2

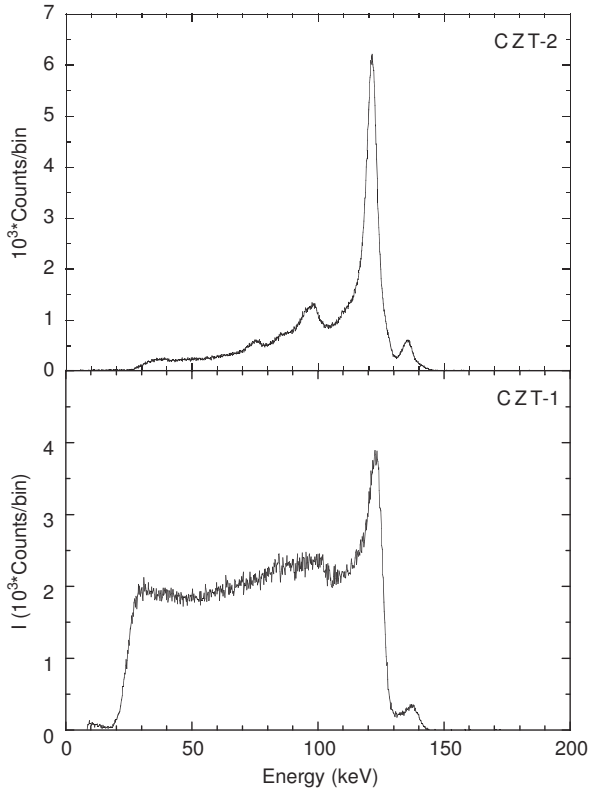

Both effects can be ascribed to an incomplete charge collection. The pulse height spectrum of CZT2 shows two peaks at energies below 100 keV which, due to the poorer detector response, are not visible in the CZT1 spectrum. They can be associated with characteristic X-ray escape peaks of Cd and Te isotopes. For instance, the peak located at 97 keV is due to the contribution of Te (K_α =27 keV) and Cd (K_α = 23 keV) X-ray photons which escape the detector. The Compton edge associated with the 122 keV full-energy peak, which is expected at 39 keV, is barely visible just above the ADC lower level

discrimination (LLD) threshold, set at 30 keV. Due to its higher detection efficiency and energy resolution, only data recorded with CZT2 have been selected for presentation in this section.

4.3.2 Time calibration

In the DAE the stop signal is measured with a certain delay caused by the electronic signal processing. In the case of the biparametric data acquisition system, the main contribution to such delay comes from the ADC conversion time, t_{ADC}. The latter is written as a sum of two main contributions, *i.e.* $t_{ADC} = t^{'} + t(E_\gamma)$, where $t^{'}$ has a constant value of about 12 μs while $t(E_\gamma)$ depends on the energy E_γ deposited in the detector. This term introduces a linear distortion in the data (see fig. 4.20(a)) which can be corrected knowing the energy calibration. The slope is 9,33 $\times$ 10^{-2} $\frac{\mu s}{keV}$ (the same for all stripes), so that the measured t values, t_{exp}, can be corrected to obtain the reduced values $t_{red} = t_{exp} - t(E_\gamma)$. The results obtained have an accuracy better or equal to 1 bin (1 μs) as reported in fig. 4.20(b).

In an ideal acquisition, the measured neutron TOF represents the difference $t_{stop} - t_{start}$. The TOF, t_r, of a neutron of energy E_r can be precisely calculated from the relation:

$$t_r = \frac{L_0}{v_r} \tag{4.1}$$

where v_r the velocity of the neutron with kinetic energy equal to the resonance energy, E_r. Since in the RD configuration it is the photon which is detected, one should add the term $\frac{L_1}{c}$ on the right hand side of Equation (4.1), representing the photon TOF in the secondary path L_1 (analyser foil-detector distance). However, such a term, which is of the order of 1 ns, can be neglected

if compared to typical values for t_{res} which are of the order of tens to hundreds of microseconds for neutron resonances in the 1-200 eV range. The calculated t_r values are shown in the second column of Table 4.4. In the real acquisition,

Table 4.4: List of the resonance energies of ^{238}U and ^{197}Au analyser and calculated time positions of the resonance peaks

E_r (eV)	t_r [μs]
^{238}U analyser	
6.671	309.5
20.80	175.0
36.60	132.0
66.00	98.37
80.73	88.95
102.5	78.94
116.9	73.92
189.7	58.03
208.5	55.22
^{197}Au analyser	
4.906	360.9
60.30	102.9

the reduced time values, t_{red}, need to be calibrated against the calculated t_r as described below. In this experiment the start signal is provided by the spallation source with a fixed time delay, t_{delay}, while the stop signal is also measured with a time delay, t_{ADC}. The reduced measured time of flight values, t_{red}, can thus be expressed as:

$$t_{red} = t_{stop} - t_{start} + t_0 \tag{4.2}$$

where t_0 is an offset value equal to $t^{'} - t_{delay}$. The time calibration procedure thus consists of determining the best value of t_0.

From the reduced biparametric spectrum one can introduce a selection window

on the x-axis (energy axis) of fig. 4.20, for instance, and project the data along the y-axis (time axis). The obtained spectrum is the neutron TOF spectrum corresponding to the selected energy window. This is shown, for instance, in Figure 4.23 for the ^{238}U reduced data. Here the spectrum was produced without any energy selection, *i.e.* accepting photons of all energies on the x-axis of fig. 4.20, above the discrimination value. The different neutron TOF values, shown on the x-axis of fig. 4.23 with 1 μs time bin, correspond to different incident neutron energies. Nine peaks can be identified, corresponding to the observable ^{238}U resonances, where the intensity was normalised to the integrated proton beam current. The time was corrected for the offset value, t_0, as determined by fitting the measured positions in time of each resonance to the calculated values, indicated with dashed lines in fig. 4.23. This calibration procedure yields an average value of $t_0 = 6.1 \pm 0.1$ μs. This gives good agreement between the calculated and measured position for all the observed resonances.

A similar analysis performed on ^{197}Au data yielded the TOF spectrum of Figure 4.24. The data were obtained by integrating over the full ADC energy range above a threshold value of 7 keV. The two peaks, corresponding to the resonances located at 4.906 eV and 60.3 eV, allowed the determination of t_0=(9 $\pm$ 1) μs.

4.4 Results

Information that can be extracted from the collected biparametric data is dual: by introducing a selection window on the time (energy) axis and projecting the data along the other axis one obtains the energy (neutron TOF) spectrum

Figure 4.23: TOF spectrum showing the calibrated position of the resonance peaks of ^{238}U

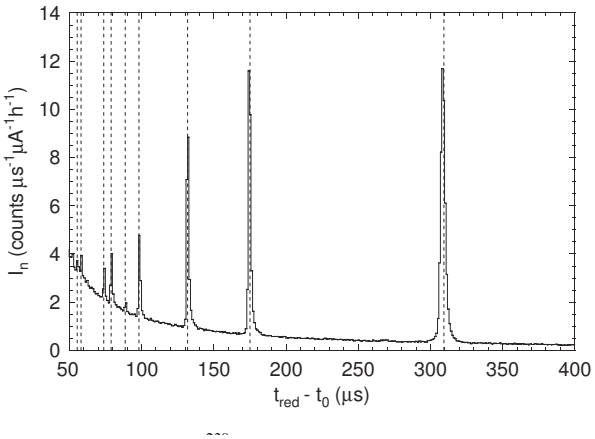

corresponding to the selected neutron TOF (energy) window.

4.4.1 Energy spectra

The CZT pulse height response to neutron absorption in the analyser foil is given by the energy spectra associated with resonant and non-resonant neutron energy intervals. An example of such spectral analysis performed on the first four ^{238}U resonances, is illustrated in Figure 4.25. In each panel two spectra are shown corresponding to the resonance (continuous line) and off-resonance (dashed line) energy spectra. Each pair of spectra have been produced selecting narrow time windows around each neutron resonance and broad windows in the off-resonance regions. The resonance and off-resonance energy spectra were thus obtained projecting the biparametric data associated with the chosen time windows along the energy axis. For instance, the pair of energy spectra of fig. 4.25 (a) were generated by selecting in fig. 4.23 an 8 μs wide

Figure 4.24: TOF spectrum showing the calibrated position of the resonance peaks of ^{197}Au

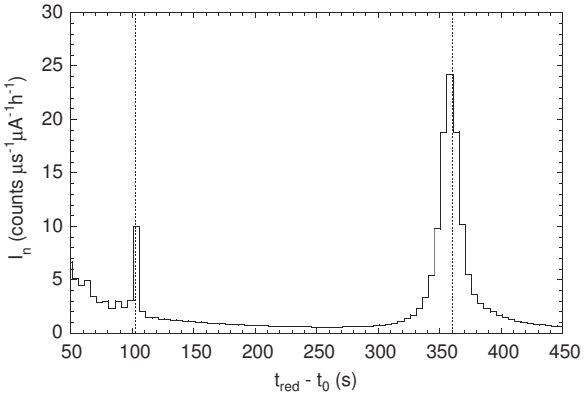

time window centered around $t = 309.5$ μs, *i.e.* the 6.671 eV resonance, and the region 193.4 - 293.4 μs, *i.e.* an off-resonance interval. Similar time windows were chosen for the pairs of spectra shown in figs. 4.25(b), (c) and (d) associated with the resonances located at $t = 175$ μs ($E_r = 20.87$ eV), $t = 129$ μs ($E_r = 36.68$ eV) and $t = 99$ μs ($E_r = 66.02$ eV) respectively. In each panel the two spectra have been normalised to the same number of total counts, with the exception of a 16 keV wide region around the peak located at 133.8 keV. Each pair of resonance and off-resonance spectra essentially contains the same features within statistics. Exceptions are the peak located at 133.8 keV and a slightly higher intensity in the tail at the high-energy region of the spectrum, both components being present in the on-resonance spectra only. The 133.8 keV peak is a prompt radiative capture γ, its broadening (4.5 keV) being entirely due to the CZT energy resolution while the tail the high energies can be ascribed to Compton events induced by high energy radiative capture γ's.

Figure 4.25: projection on the energy axis of the bidimensional plot shown in fig. 4.20 for different on- and off-resonance time windows

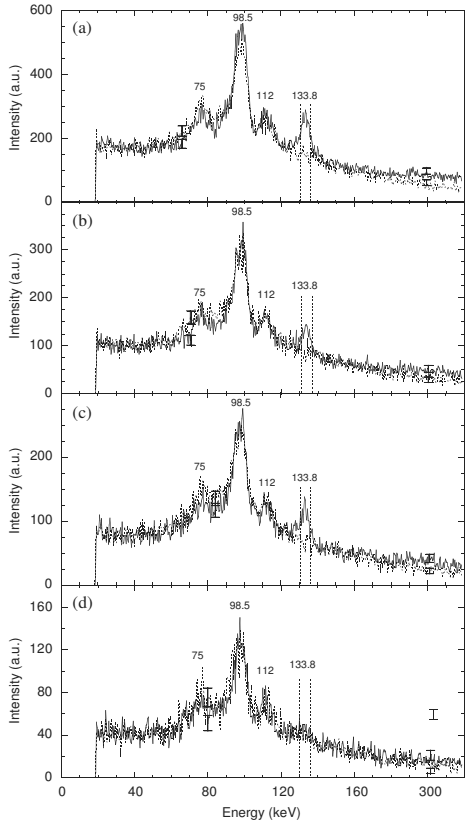

The most intense peak, located at about 99 keV, and its neighbor peak at 112 keV are present in both energy spectra and can be identified as K-shell X-ray lines from uranium atoms. The broad energy resolution of the CZT at these energies (3.5 keV) does not allow a clear separation of the contribution of several uranium X-ray lines which are too close to be distinguished. For instance, the most prominent peak, located at 98.5 keV with a broadening of 7 keV, is due to the contribution of the 94.7 keV ($K_{\alpha 2}$) and 98.4 keV ($K_{\alpha 1}$) lines, where

the latter is the most intense one [120]. The peak at 112 keV is due the $K_{\beta 2}$ = 111.3 keV line, of lower intensities with respect to K_α lines. These X-ray lines comes from de-excitation of uranium atomic levels induced by absorption of both resonant and non-resonant neutrons; the most likely generating mechanism is believed to be internal conversion of the radiative capture γ's in the ^{238}U converter itself. The peak located at approximately 75 keV can be univocally ascribed to the decay of the ^{239}U nuclei which are continuously formed via ^{238}U(n,γ)^{239}U. The isotope ^{239}U decays via β^- with a half-life of about 24 min into an excited state of ^{239}Np which, in turn, radiatively decays to the ground state emitting the most intense line at 74.7 keV. Such a line is therefore not directly associated with X-ray or prompt emission following neutron absorption and must be included in the background.

Similarly, selecting narrow time windows in fig. 4.21 around the ^{197}Au resonances and wider off-resonance intervals, the energy spectra of Figure 4.26 are obtained. The energy spectra, after normalisation to the same number of counts in the energy region 10-50 keV, show similar features to those observed for ^{238}U resonances. The most intense peaks, located at 69.0 and 78.0 keV, can be ascribed to K_α and K_β X-ray lines of Au, respectively, while the two lower intensities peaks at 55.15 and 91.19 keV are present in the resonance spectra only. Such lines correspond to the expected γ emission following thermal neutron absorption on ^{197}Au (see fig. 3.3). The most intense prompt γ emitted by ^{197}Au is at 75 keV but the low CZT energy resolution prevents its separation from the X-ray lines of fig. 4.26. It can also be observed that the resonance and off-resonance normalised energy spectra differ in the high-energy region of the spectrum ($E \geq 110$ keV). This is due to the prompt high energy photons (energy up to 6.5 MeV) emitted by ^{198}Au which still have a finite probabil-

Figure 4.26: projection on the energy axis of the bidimensional plot shown in fig. 4.21 for different on- and off-resonance time windows

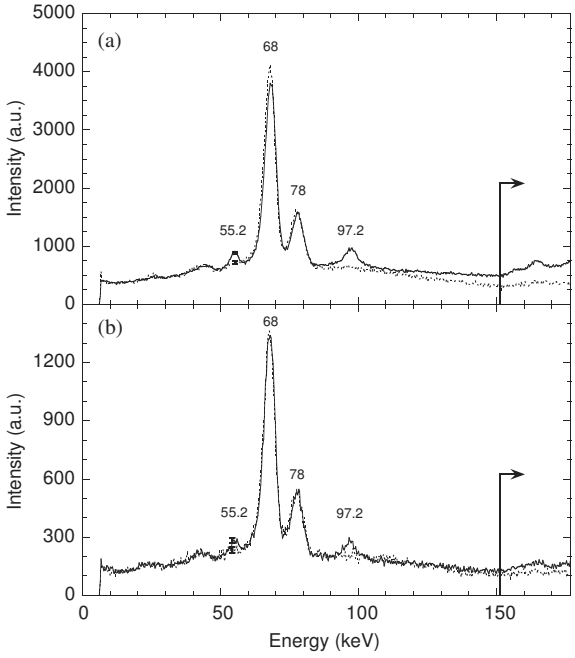

ity of being detected in the CZT2 crystal (about 20 % at 1 MeV). At such energies, Compton contribution is dominant over photoelectric full energy absorption, due to the relative weights of the photon cross sections combined with the small size of the detector. These Compton events are characterised by a partial photon energy release in the detector and therefore give rise to a continuous broad distribution in the energy spectrum. This feature is particularly evident in the measurements with ^{197}Au due to the presence of several intense lines in the energy range 150-700 keV in the radiative capture emission spectrum. For ^{238}U resonances (fig. 4.25) the effect is less pronounced due to the low relative intensity of the radiative capture lines in the energy range

above 150 keV (see fig. 3.2).

4.4.2 TOF Spectra

The measured resonance energy spectra have shown that the radiative prompt γ's are indeed a clear signature of resonance reactions and could be used to tag the absorption of resonant neutrons, with the aim of improving the S/B ratio of the measurement. Such a possibility has been investigated by introducing a narrow energy window ($130.5 \leq E \leq 135.7$ keV) around the 133.8 keV line of ^{238}U (fig. 4.23) and generating the corresponding TOF spectrum. The obtained result is compared in a semi-log plot (Figure 4.27(a)) with the TOF spectrum obtained without any energy selection.

The result indicates that a small S/B improvement can be obtained but with a strong intensity reduction, as can be argued from the statistical fluctuations on the data obtained with the narrow energy window.

The measured energy spectra of ^{197}Au seem to suggest that the best S/B can be obtained by choosing a LLD threshold at about 150 keV, as indicated in fig. 4.27. The TOF spectrum obtained with this LLD threshold setting (fig. 4.27(b)) shows that an improvement in S/B of about 1.8 can be obtained by accepting an intensity reduction of about 1/6. This shows that energy discrimination can be used as a method to improve the quality of the measurement.

The measured energies and relative intensities of the γ lines of ^{238}U and ^{197}Au energy spectra, for resonant neutron absorption, are in good agreement with the available database for thermal neutron absorption. The only exception to this is the line at 48.2 keV which is expected in the ^{238}U emission spectrum with a relative intensity $I = 40$ %, while the measured resonance spectra (fig.

Figure 4.27: TOF projection of the bidimensional plot shown in Figures 4.20 and 4.21 for different γ energy windows

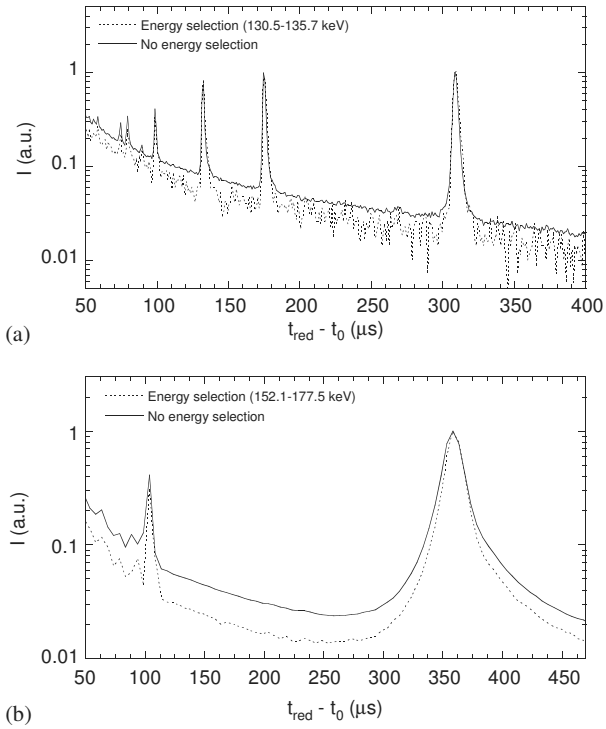

4.25) do not show any peak in that an energy range. The 133.8 keV line is indeed expected to be the most intense one (relative intensity $I = 60$ %) in the energy range covered by the detector. In fact, the 12 keV line (I = 100 %), is both heavily attenuated by self-absorption in the foil analyser and strongly absorbed by the aluminium window of the vacuum chamber. This seems to indicate a suppression of the 48.2 keV line or at least a significative variation of its relative intensity for resonant neutron absorption as compared to thermal neutron absorption. Considering the higher attenuation lengths in aluminum and uranium of a 48.2 keV as compared to the one for a 133.8 keV,

the absence of the 48.2 keV line in the measured energy spectra, provides an upper limit, given by the statistics, for its relative intensity of $I \leq 30$ %. The measured neutron TOF spectra have shown that S/B of these measurements is very high for many of the resonances. For instance, S/B evaluated at the resonance peak is in the range 30-40 for the two lowest-energy resonances of the ^{238}U and ^{197}Au analyser foils. The measurements have shown that nine resonances can be observed, in the data from ^{238}U, up to a neutron energy of 208.5 eV. However, the experimental set up of the biparametric measurements is different from the one that is used in DINS experiments employing the RD configuration. DINS measurements on a lead sample have shown that there is an increase of the background level caused by scattered neutrons and environmental photons present in the experimental hall. Data showed that neutron resonances up to 66 eV can be analyzed, whereas the background is preventing the analysis of higher energy resonances. The aim of the biparametric measurements was to investigate the possibility of improving the S/B of the measurements via energy discrimination. The result is that an improvement of S/B can be obtained by lowering statistics (fig. 4.27). The method is most effective for ^{197}Au resonances due to a higher difference between the resonance and off-resonance energy spectra in the energy region above 150 keV. This increasing difference in the energy spectra in the high energy region suggested that a detector optimised to observe a broader energy range, might have better performances. This has motivated further tests on new detectors

4.5 Experiments with Yttrium-Aluminum-Perovskite scintillators

This section is dedicated to the experimental tests performed with Yttrium-Aluminum-Perovskite (YAP) scintillators.

YAP is a fast, mechanically and chemically resistant scintillation material, with mechanical properties enabling precise machining to many different shapes. The inorganic scintillator is nonhygroscopic, glasslike, with a high density 5.55 g·cm^{-3} but a low effective atomic number Z=36. Main characteristics of this scintillation material are a good light yield (18000 photons/MeV) and a short decay time (t_d = 27 ns) at a wavelength of maximum emission (λ = 350 nm).

The material is relatively stable over a wide temperature range. Its chemical composition is such that no neutron resonances are present in the energy range of interest (1-200 eV). In Table 4.5 the main characteristics of the detector are summarised.

Table 4.5: main physical characteristics of YAP(Ce) scintillator

Effective atomic number	36
Density ($\frac{g}{cm^3}$)	5.55
Maximum emission λ (nm)	350
Refractive index at λ_{max}	1.94
Light yield ($\frac{photons}{MeV}$)	18 10^4
Decay time (ns)	27
Hygroscopic	no

4.5.1 DINS measurements

The first experiment with YAP scintillator has been carried out during standard DINS measurements on Pb and ZrH_2 samples. The YAP crystal used in these experiments was manufactured with a cylindrical shape (35 mm diameter by 6.4 mm thickness). The crystal was glued to a standard 51 mm photomultiplier tube with a bialkali photocathode. The crystal thickness was somewhat arbitrary but represented a compromise between the need for good detection efficiency of the γ emission, following neutron capture in the analyser foil, and low neutron scattering in the crystal. In Figure 4.28 the total absorption probability curve for a 6.4 mm thick YAP crystal is plotted in the 10-1000 keV photon energy range. Below 100 keV photoelectric interaction

Figure 4.28: Photon absorption probability curve as a function of energy for the YAP crystal described in the text.

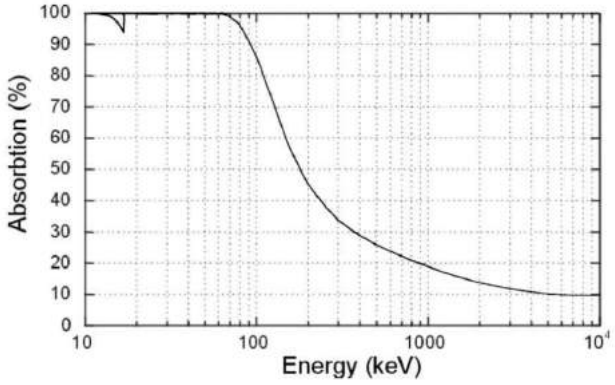

is the dominant process for energy deposition in the crystal and guarantees 100% total absorption probability. The edge in the absorption efficiency located at 17 keV corresponds to the K_α edge of yttrium. Above about 200 keV

Compton interaction becomes the dominant mechanism for energy deposition in the crystal, providing a still significant absorption probability (about 10% above 1 MeV).

As far as the DINS experiment on the Pb sample is concerned, the spectrometer′s geometrical set up was similar to that employed for DINS measurements with CZT (see fig. 4.12). The YAP was at $\vartheta \simeq 90°$ and coupled to a ^{238}U analyser. In Figures 4.29 and 4.30, the TOF spectra relative to Pb sample acquired with

Figure 4.29: DINS spectrum from a Pb sample acquired with YAP, employing a 40 keV LLD

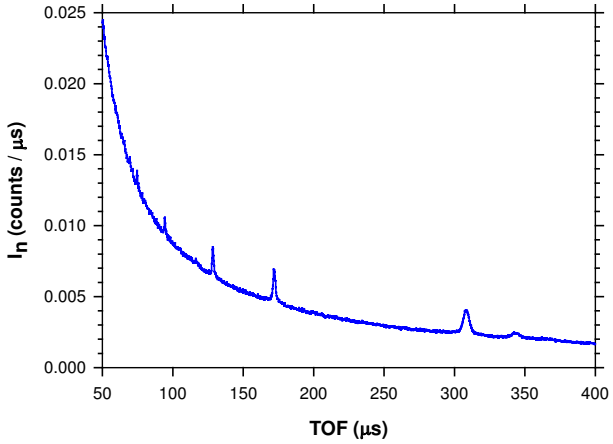

a LLD threshold of 40 keV and 600 keV are shown, respectively. The main difference between the lower and the higher LLD threshold spectra is a very impressive improvement of the S/B ratio. For instance, for the peak at 310 μs (Pb recoil peak corresponding to $E_1 = 6.671$ eV) in fig. 4.30 the background is 20 times lower and the peak intensity 2.5 times lower as compared to the same peak and background intensities of the same peak in fig. 4.29. A further

Figure 4.30: DINS spectrum from a Pb sample acquired with YAP employing a 600 keV LLD

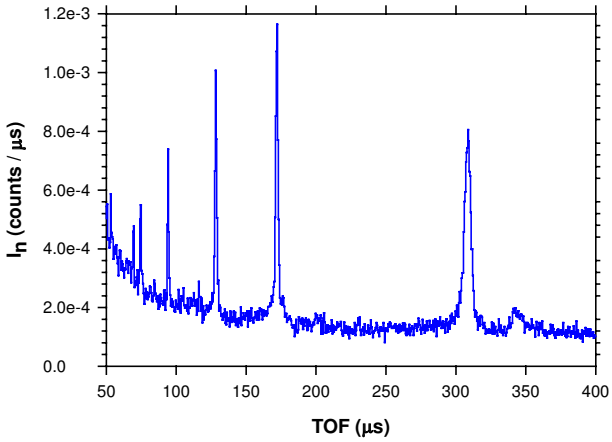

comparison can be made with ^{6}Li-glass scintillation detectors, by considering Figure 4.31 where the RF and RD spectra are shown in the same TOF region. For all the recoil peaks in the spectrum the S/B ratio is better for YAP than for ^{6}Li-glass. Table 4.6 shows the S/B ratio values for YAP and ^{6}Li-glass, calculated for several recoil peaks in the spectrum. DINS measurements on ZrH_2 have been performed in both RD and RF configuration in order to compare the different instrumental performances for DINS on light nuclei. Figure 4.32 shows the TOF spectra acquired with ^{6}Li-glass and YAP in the 100-500 μs TOF region. The narrower peaks (dips) at about 320 μs, 180 μs and 140 μs are the Zr recoil peaks, while the broader ones (on the left of the Zr peaks) are the H recoil peaks. In figure 4.33 the Filter Difference (FD) spectrum acquired with ^{6}Li-glass is shown together with the spectrum acquired with YAP. Referring to the intense H recoil peak at about 290 μs, the signal intensities for RD and RF spectra are quite similar (about 5×10^{-2}) but the associated

Figure 4.31: DINS spectra from Pb sample acquired with a ^{6}Li-glass detector (upper plot) and YAP scintillator (lower plot) placed at the same scattering angle

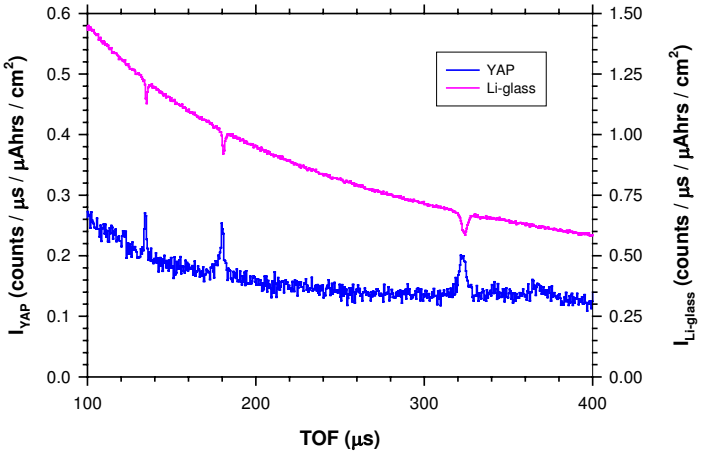

statistical error is a factor of 1.5 smaller for RD (2×10^{-3}) as compared to the RF one (3×10^{-3}). It has to be stressed that the YAP detector is a factor of 6 smaller as compared to the ^{6}Li-glass.

Table 4.6: List of the S/B ratios for YAP and ^{6}Li-glass: the first column indicate the time positions of the Pb recoil peaks considered, the second is the corresponding final neutron energy (resonance energy), while the third is the S/B value

recoil peak t position [μs]	$E_1[eV]$	S/B
YAP (LLD = 40 keV)		
310	6.67	0.60
180	20.8	0.40
135	36.6	0.15
90	66.0	0.13
70	80.3	0.09
55	102	0.07
YAP (LLD = 600 keV)		
310	6.67	4.00
180	20.8	6.25
135	36.6	4.00
90	66.0	2.72
70	80.3	1.24
55	102	0.71
^{6}Li-glass		
310	6.67	0.12
180	20.8	0.09
135	36.6	0.07

Figure 4.32: DINS spectra from a ZrH_2 sample acquired with a ^{6}Li-glass detector (upper plot) and YAP scintillator (lower plot) placed at the sample scattering angle

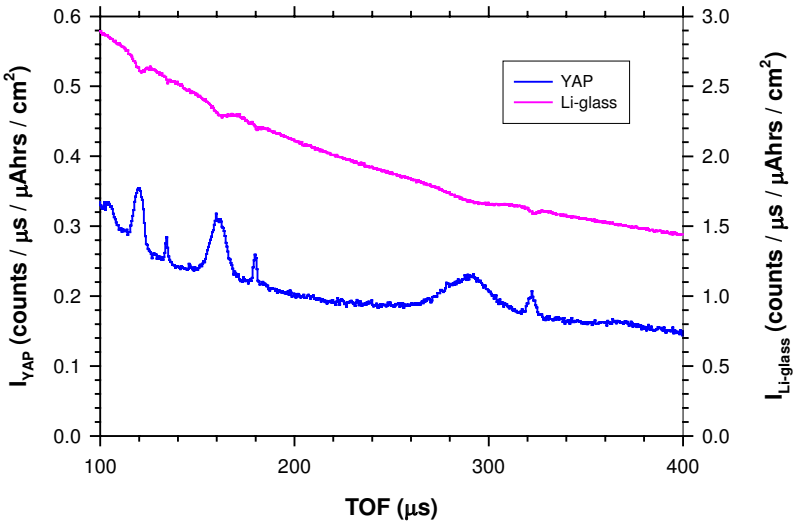

Figure 4.33: RD TOF spectrum (same as fig. 4.32) and background corrected RF spectrum.

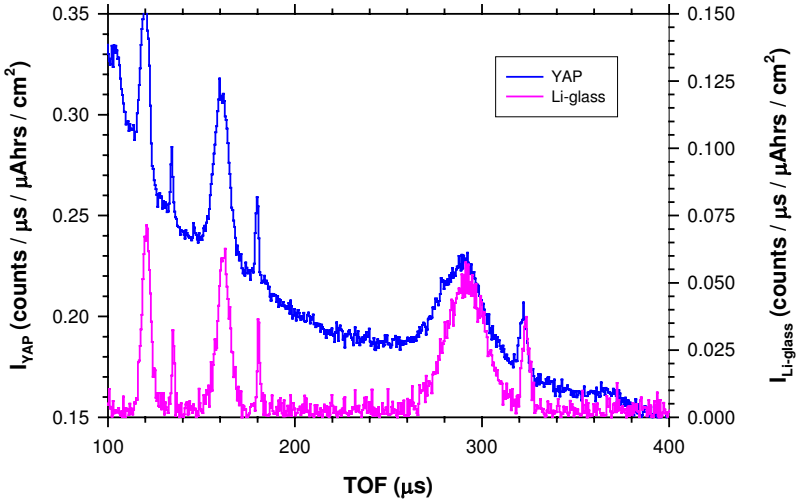

4.6 Biparametric measurements

Differently from CZT, the YAP biparametric measurements presented in this section, have been carried out during DINS experiment on a Pb sample. For these measurements the detection system was located on the secondary flight path at a distance $L_1 = (0.30 \pm 0.01)$ m from the sample and a scattering angle $\vartheta = 90° \pm 5°$. A schematics of the experimental set up of the measurement is shown in Figure 4.34. In the present experiment the sample was a 1 mm

Figure 4.34: Experimental set up for the biparametric DINS measurements with YAP on VESUVIO

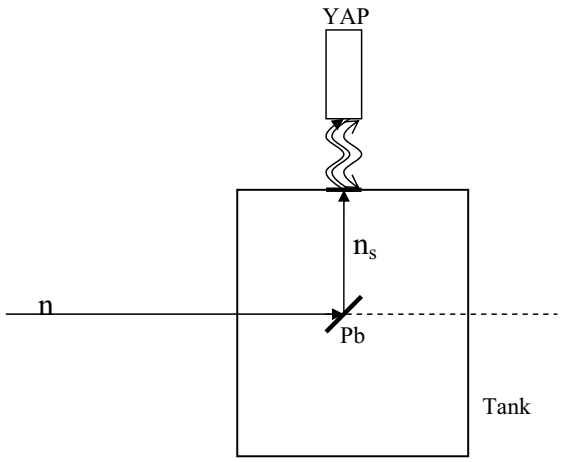

thick Pb metallic slab 2.5 × 3.5 cm^2, supported by an aluminum frame, while the analyser was an uranium foil of 2.4 × 3.5 cm^2 area and 60 μm thickness. The chosen thickness ensured both good neutron absorption efficiency and low self-absorption of the radiative capture γ-rays. The foil was attached to the same YAP employed in the standard DINS measurements discussed before.
In order to perform biparametric measurements, a dedicated data acquisition

system was specifically set up. The main elements of the signal processing and biparametric acquisition are briefly described below. The negative analog signal from the PMT was firstly integrated and inverted. The analog signal was then further amplified by a timing filter amplifier and sent to a 13 bit ADC. The ADC operated with a fixed conversion time of 500 ns and an internal LLD, set to the minimum level (about 70 keV during data acquisition) compatible with acceptable dead time values. The digital output from the ADC was fed into the modified DAE, resulting in a biparametric acquisition (TOF vs energy). A fixed energy bin was chosen for the pulse height spectrum while a variable time bin was used to cover the entire TOF region with adequate time resolution. The chosen time bins values where 0.25 μs in the time region 30-260 μs, 0.5 μs in 260-500 μs, 5 μs in 500-1500 μs and variable bins in 1500-20000 μs.

4.6.1 Energy calibration

Due to the poor resolution of the YAP as compared to that of CZT, the energy calibration was not feasible with the ^{57}Co source only. In fact, as shown in Figure 4.35(a), it was not possible to resolve the 122 keV and the 136 keV peaks. Thus, a second energy calibration point is provided by the lead biparametric measurement as described below. The γ pulse height spectrum, obtained integrating the Pb sample biparametric data in the TOF region 400-800 μs, is shown in Figure 4.35(b). The selected TOF region corresponds to incident neutron energies in the range 1-4 eV. The broad peak around channel 280 can be ascribed to the full energy absorption of γ rays of 477.8 keV energy, which are produced by neutron absorption in ^{10}B used in the walls of the experimental hall and in the beam dump to absorb neutrons. Due

Figure 4.35: Pulse height spectra from a ^{57}Co source (a) and energy projection of the biparametric measurement on the Pb sample (b). The pulse height spectrum from the ^{57}Co source is obtained integrating the biparametric data at all times, while the pulse height spectrum from the Pb sample is obtained integrating over 400-800 μs time interval.

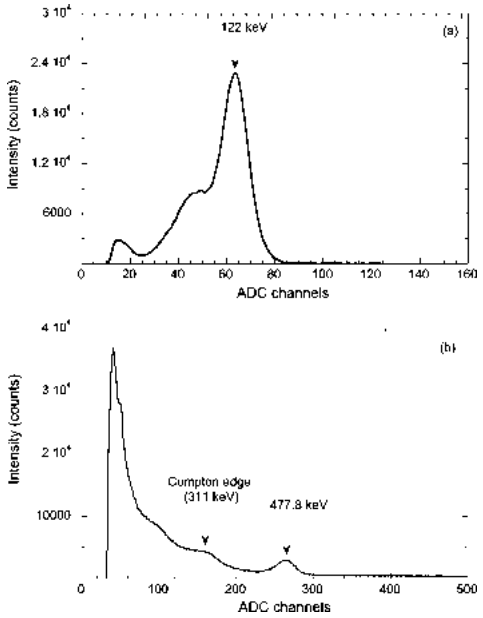

to the low absorption probability of the YAP detector at such energies the majority of 477.8 keV γ rays interact via Compton scattering. The Compton edge of the ^{10}B photopeak is located at 311 keV and shows it up with its characteristic shoulder. The two full energy peaks provided by the pulse height measurements of the ^{57}Co source (fig. 4.35(a)), and of the ^{10}B neutron capture γ (Figure 4.35(b)), respectively, have been used to assign a linear energy scale to the γ energy axis of the biparametric data acquisition system. The ^{10}B background peak at 477.8 keV also provides an absolute pulse height reference

during the Pb measurement which has been used to monitor the stability of the gain of the PMT tube and the drifts of the electronics. By analysing pulse height spectra at different TOF intervals one can check for possible shifts of the 477.8 keV peak. This was done by comparing pulse height spectra obtained integrating TOF values in 50 μs consecutive intervals. The result indicates that the ^{10}B peak shifts upward by about 4% over the whole TOF region. This shift can be attributed to an increase of the PMT tube gain. The gain value is higher at the short TOF values when the YAP records the highest count rate, and decreases until it reaches its minimum (steady state) value at about 1000 μs. The size of the effect, which is a well-known behavior of PMT subject to rapidly varying count rate conditions [121], is at an acceptable level for the purpose of these measurements.

4.6.2 Time calibration

Differently from the time calibration performed with CZT, where the analyser was placed in he sample position, here the TOF is related to the recoil scattering process. Thus the total neutron TOF is given by:

$$t_r = t_0 + \frac{L_0}{v_0} + \frac{L_1}{v_r} \tag{4.3}$$

where t_0 is a fixed time delay provided by the ISIS spallation source, while v_r is the final neutron velocity. The final and initial neutron velocities are related by the kinematics of the scattering process, which in the case of free recoil can be written as:

$$\frac{v_r}{v_0} = \frac{cos\vartheta + \sqrt{(\frac{M}{m})^2 - sin^2\vartheta}}{\frac{M}{m} + 1} \tag{4.4}$$

where ϑ is the scattering angle, M the mass of the recoiling Pb atom in the sample (M = 207.2 a.m.u.) and m the neutron mass. From the system of

equations (4.3) and (4.4), t_r can be resolved as a function of the unknown variables t_0, L_1, and ϑ. A general description of the calibration procedure in the standard configuration can be found in Ref. [115]. In this experiment we have determined the values of $L_1 = (30 \pm 2)$ cm and $\vartheta = 90° \pm 2°$ from direct measurements, and estimated the best value of t_0 with a time calibration procedure similar to that described in Section 4.3.2.

The best linear fit yields a value of $t_0 = -5.9 \pm 0.5$ μs and gives good agreement between the calculated and measured position for all the observed recoil peaks. Figure 4.36 shows the TOF spectrum from Pb with a LLD of 600 keV. The dashed vertical lines indicate the correspondence between TOF positions and scattered neutron energies. The agreement between calculated and calibrated values is good.

4.7 Results

In order to characterise the YAP response, the identification of the main signal and background components, associated to the absorption of resonant and non-resonant neutrons in the analyser foil was necessary. To this aim, TOF and γ energy projections can be used for this purpose.

The TOF spectrum from the Pb polycrystalline sample, generated with a LLD value of 600 keV, is shown in a log-log plot in Figure 4.37 in the entire TOF region. The plot shows an overall background with a characteristic power law curve. Two distinct time regions can be identified: the free recoil region ($t \leq$ 800 μs) where neutrons above 1 eV, scattering off freely recoiling masses, are detected via resonant absorption; (ii) $t \geq 800$ μs corresponding to the arrival times of lower energy neutrons $E_n \leq 1$ eV. The horizontal dashed line in fig.

Figure 4.36: TOF spectrum from the Pb sample obtained by projecting the biparametric data along the time axis for a 600 keV discrimination energy. The expected time positions of the Pb recoil peaks are indicated by dashed lined. The corresponding final neutron energy values are also labelled

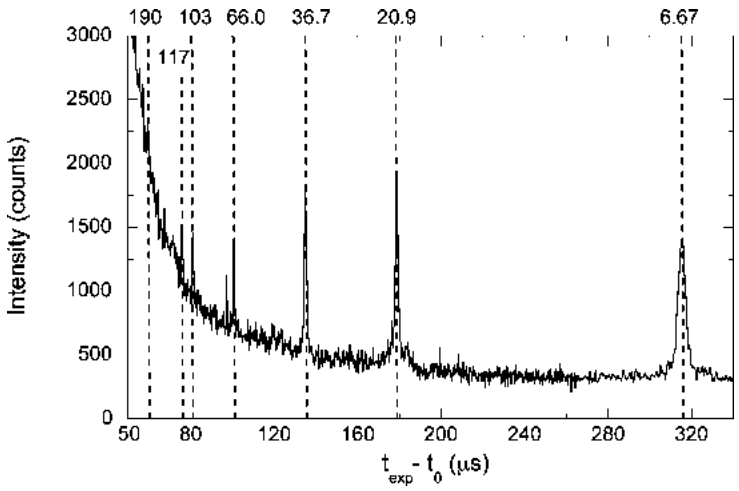

4.37 indicates the constant background level registered by the YAP, which is due to the analyser foil radioactivity. The signal in the TOF spectrum is represented by Pb recoil peaks registered via resonance absorption in the ^{238}U analyser foil at different final neutron energies. Seven peaks corresponding to neutron resonances going from 6.67 up to 189.7 eV can be distinguished from the background (fig. 4.36). The resonance at 80.7 eV is not distinguishable in the plot due to the small value of the cross section.

The background under the recoil peak can be ascribed to an environmental component, consisting of X-rays and γ-rays with a time structure related to the neutron beam, and a constant radioactivity component, which has a flat time spectrum. The environmental γ background is generated by neutrons

Figure 4.37: Same plot as fig. 4.36 plotted in a log scale in the time interval 50-20000 μs. The vertical dashed lines indicate the Pb recoil peaks. The radioactivity level induced by the uranium analyser foil is indicated by the horizontal dashed line.

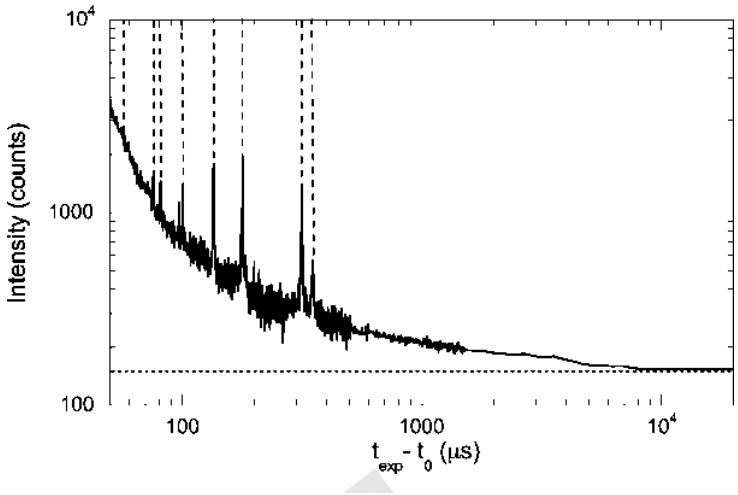

absorbed in the materials present in the experimental hall, *e.g.* in the beam dump. A significant contribution to the γ background is also represented by neutrons which scatter several times in the experimental hall before being absorbed in the ^{238}U analyser foil. Finally, a fraction of γ rays is also known to come directly from the cell and sample itself whenever they contain isotopes with a high absorbing radiative neutron cross section. This sample dependent background in the case of Pb in an Al cell is a small fraction of the total background but it can represent a significant fraction in the case of hydrogenated samples, as it will be shown in Chapter 5. The radioactivity of the analyser foil was separately measured with a high resolution coaxial germanium detector which was set to cover the energy range up to 2 MeV [122]. The germanium

crystal provided a 20% efficiency at 1.33 MeV with an energy resolution of 1.6 keV (FWHM). The pulse height measurement (Figure 4.38) shows a series of γ lines which can be ascribed to the radioactive decay chains of ^{238}U and ^{235}U isotopes of the analyser foil. Among many peaks of fig. 4.38 one can identify

Figure 4.38: Pulse height spectrum of the ^{238}U analyser foil recorded with a germanium detector. The mean energies of some of the most prominent peaks are indicated.

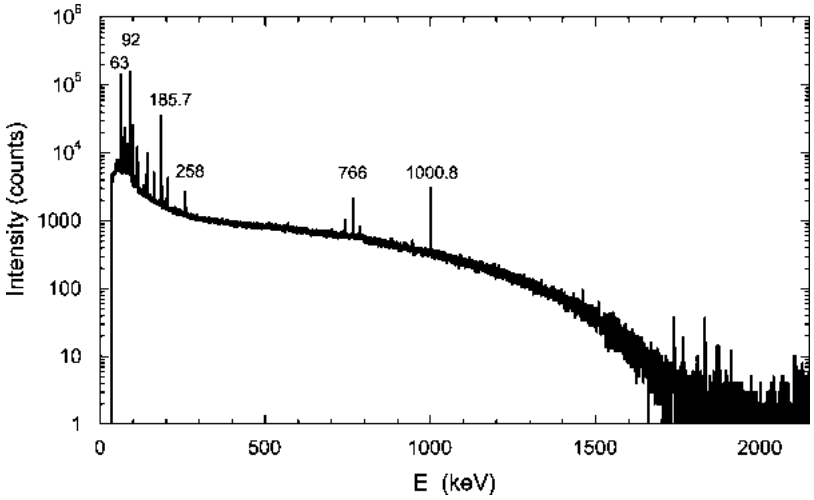

the line at 185.7 keV as a β decay line of ^{235}U and the line at 92 keV as X-ray emission from thorium isotopes. The latter are produced from the decay chains of the two uranium isotopes. The YAP background and signal features identified in the TOF spectrum can be studied by analysing the γ pulse height spectra associated to different time regions. The energy spectrum from YAP detector, corresponding to the time region 10-1000 ms is shown if Figure 4.39. The spectrum is dominated by the radioactivity of the uranium analyser foil. A direct comparison with fig. 4.39 shows that the two major peaks in the spec-

Figure 4.39: Pulse height spectrum from the Pb sample obtained by projecting the biparametric data on the energy axis in the time interval $10000 \leq t \leq 20000$ μs.

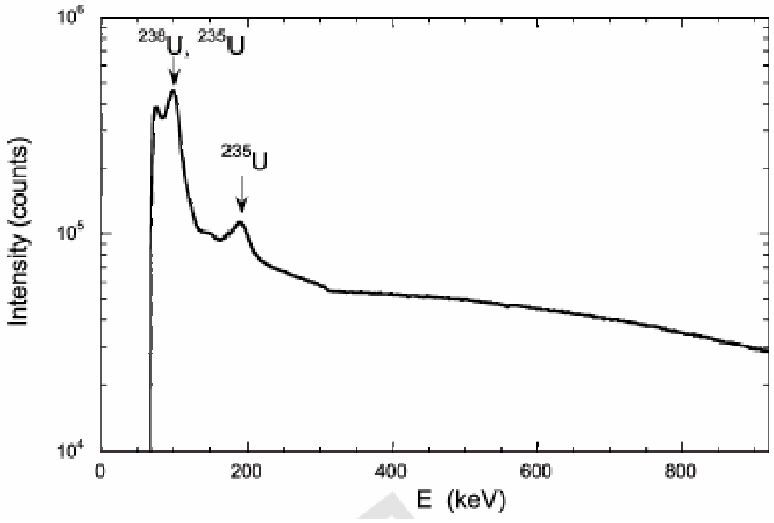

trum can be ascribed to the decay chains of ^{238}U and ^{235}U. The YAP pulse height response to neutron absorption in the ^{238}U analyser foil is shown in Figures 4.40(a)-(c) for the neutron resonances located at 6.67, 20.86, and 36.68 eV. The two spectra in each panel correspond to the resonance (continuous line) and off-resonance (dashed line) energy spectra. The pair of energy spectra of fig. 4.40(a) were generated by selecting a 4 μs wide time window centered around t=309.5 μs, *i.e.* the 6.671 eV resonance, and the region 272-299 μs, *i.e.* an off-resonance interval. In each panel the two spectra have been normalized to the height of the ^{10}B peak, which provides a convenient normalization point. For $E \leq 400$ keV the spectra show essentially the same features. The measurements performed with CZT detectors in the energy range 20-200 keV indicated that small differences exist between the resonance and off-resonance

Figure 4.40: Pulse height spectrum projection from the Pb sample. In each panel a pair of normalized spectra are shown corresponding to a narrow time window around the neutron resonance (continuous line) and an off-resonance region (dashed line).

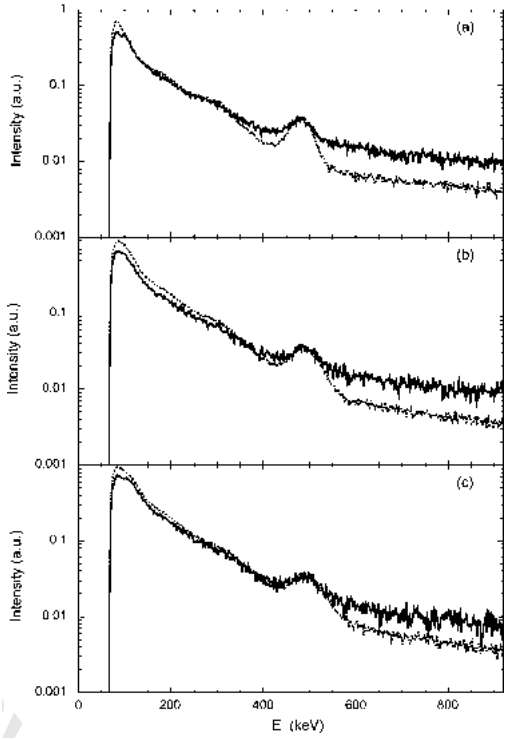

spectra but they cannot be distinguished by the YAP detector due to its poor energy resolution. Above 500 keV the on-resonance spectrum is systematically higher (about a factor two) than the off-resonance spectrum. These events are due to the Compton interactions of the radiative capture γ-rays of high energy (above 700 keV). The higher on-resonance spectrum level represents a clear signal signature which suggests that an improvement of the S/B ratio of the TOF measurement can be obtained by increasing the γ energy discrimination. This occurs at the cost of a reduced counting statistics.

In order to investigate the best tradeoff between high S/B ratio and high counting statistics, a figure of merit F can be defined. Here F is defined as the ratio of the statistical error to the number of signal counts S under the recoil peak, i.e., $F = \frac{\sigma_s}{S}$. Indicating with B the number of background counts under the peak, the total number of counts can be expressed as $\varepsilon = S + B$ and the S/B ratio as $q = \frac{S}{B}$. F can thus be expressed merely as a function of the variables ε and q as follows. The ratio of the statistical error to the number of signal counts under the recoil peak is:

$$\frac{\sigma_s}{S} = \frac{\sqrt{\sigma_\varepsilon^2 + \sigma_B^2}}{S} \tag{4.5}$$

where σ_ε and σ_B are the standard deviations of the statistical distribution of ε and B. Assuming a Poisson distribution for S and B, $\sigma_\varepsilon^2 = \varepsilon$ and $\sigma_B^2 = B$ and eq. (4.5) can be rewritten as:

$$\frac{\sigma_S}{S} = \frac{\sqrt{\varepsilon + B}}{\varepsilon - B} \tag{4.6}$$

From the definition of ε and q it is trivial to see that B can be expressed as:

$$B = \frac{\varepsilon}{1 + q} \tag{4.7}$$

while F can be written as:

$$F = q \cdot \sqrt{\frac{\varepsilon}{(1+q)(2+q)}} \tag{4.8}$$

The ε and q values of the recoil peaks in the TOF spectrum can be calculated and are used to determine F via Equation (4.8). Such data analysis procedure has been repeated for TOF spectra generated with different LLD values to obtain the three curves (i) F versus LLD, (ii) q versus LLD, and (iii) ε versus LLD. These curves are shown in Figures 4.41-4.43 for the neutron resonances

Figure 4.41: figure of merit F, S/B ratio q and counting efficiency ε versus LLD for the neutron resonance at 6.67 eV

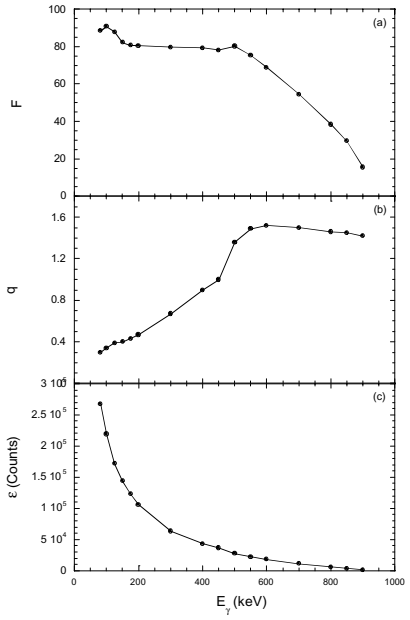

up to 36.68 eV and for 16 different LLD values, ranging from 80 to 900 keV. Increasing the LLD threshold on the pulse height enables to discriminate the background at the price of losing some signal fraction. This has been quantified in figs. 4.41-4.43 for the neutron resonances at 6.67, 20.86, and 36.68 eV respectively. All three studied neutron resonances show similar features in the S/B versus LLD curve (Figures 4.41(a)-4.43(a)). In the lower energy region 80-400 keV there is a linear increase in S/B with increasing LLD values. Such improvement can be attributed to the reduction of the background events induced by both uranium radioactivity and Compton events induced by γ from ^{10}B. The central region 400-600 keV is characterized by a steep rise in S/B (about a factor 2), primarily due to the discrimination of the ^{10}B

Figure 4.42: same as fig. 4.41 but for the 20.8 eV resonance

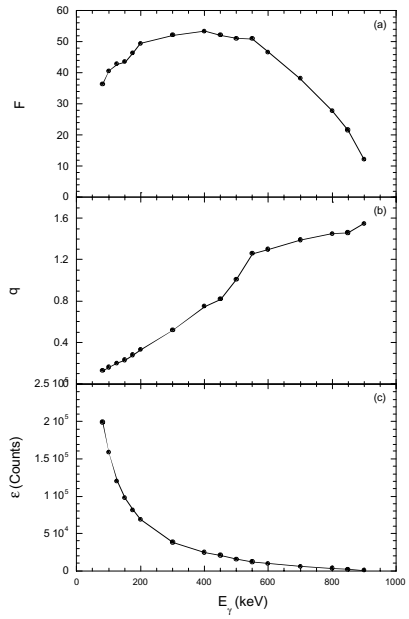

photo-peak located at 478 keV. Above 600 keV there is little improvement in S/B and the curves seem to reach a plateau. In such an energy region all ^{10}B background events and the majority of the uranium radioactivity have been rejected, which makes the background reduction that can be achieved proportional to the signal reduction, as evident in the pulse height spectra of fig.4.40. Employing γ energy discrimination there is, together with an improvement in S/B, a loss in counting statistics. This can be noticed from the plots of figs. 4.41(b)-4.43(b) where the total number of counts under the recoil peaks shows a rapid exponential decrease. The resulting statistical uncertainty in the signal as a function of LLD has been evaluated introducing the figure of merit F. The resonance at 6.67 eV shows the best figure of merit, with a rather flat distribution around the average value of F= 80 up to 500 keV [fig. 4.41(c)].

Figure 4.43: same as fig. 4.41 for the 36.6 eV resonance

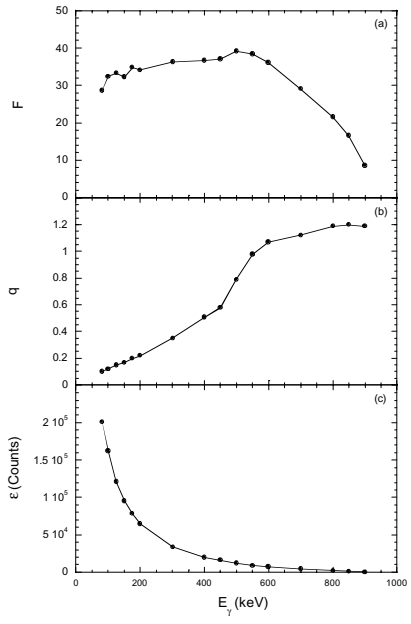

Such value translates from the definition of F into about a 1% statistical error in the signal counts under the 6.67 eV recoil peak. Increasing the LLD setting from 80 up to 500 keV has a little effect on F since the improvement in S/B is compensated from the decrease in counting statistics. The situation is partly different for the resonances at 20.86 and 36.68 eV, which are both characterized by a somewhat more peaked distribution of F, as shown in figs. 4.42(c) and 4.43(c), respectively. The two plots seem to suggest that the optimum LLD setting is around 400-600 keV. Generally the figure of merit for the three studied resonances indicates that the highest values of F are reached for a quite broad range of LLD values. This means that the LLD setting is not critical and that the gain variation of the PMT is indeed not affecting

the measurement. The curves found for q, ε and F are strictly valid only for one specific combination of sample (Pb) and detector position. The detector angular position is less important in this case since Pb is an almost isotropic scatterer. A fraction of the background is sample dependent, which means that S/B might change with different samples. The detector position plays also a role since by increasing the detector to sample distance d the signal and the sample dependent background fraction drop as $1/d^2$, while the uranium radioactivity background remains constant, which results in a reduction of S/B.

4.8 Concluding remarks

NaI

The results obtained with NaI should be regarded as a first step towards the routinely use of the RD for electron Volt neutron spectroscopy in the 1-100 eV range. The main indications achieved with NaI tests can be summarised as follows:

1. successful use of the NaI detector for RD configuration. Previous experiments had discarded NaI in favor of BGO scintillators mainly because of their lower background;

2. the NaI-^{238}U combination allows neutron spectroscopy measurements in the energy range 1-10 eV. This finding is supported from fig. 4.3 where the achieved S/B ratio for the NaI detector is comparable with that obtained from a standard ^{6}Li-glass scintillator;

3. the RD configuration overcomes the detection efficiency loss present in

the RF, allowing to reveal scattered neutrons up to 66 eV with higher intensity as compared to ^{6}Li-glass detectors;

4. demonstration of the feasibility of the Double Difference method for RD with improvement of the energy resolution.

CZT

Results from this experiment demonstrate that:

1. the CZT detector is a suitable candidate for the RD configuration for DINS measurements up to 70 eV final neutron energy;

2. an improved S/B ratio, as compared to NaI experiment, has been achieved without using any shielding around the detector;

3. the CZT is a radiation hard detector;

4. the sensitivity to both photons and neutrons is a unique property of CZT detectors. It appears that they are suitable for the development of detector arrays for space (angle)- and time (energy)-resolved neutron measurements for a broad range of applications. In particular, two possible uses of CZT$'$s as position-sensitive detectors are envisaged: at short time scale (*i.e.* high-energy neutrons) for epithermal neutron spectroscopy studies, and at long time scales (*i.e.* thermal neutrons) for application in residual stress fields in materials;

5. the effectiveness in neutron counting up to 70 eV energy allows envisaging the use of CZT for HINS measurements. The experimental access to low wavevector combined with high energy transfers would allow neutron

spectroscopy to address demanding experimental studies of the wavevector dependence of magnetic and electronic excitations, at energies usually investigated by electromagnetic probes and often not in bulk materials;

6. the biparametric measurements allowed the analysis of the pulse height spectra associated with resonant and non-resonant neutron absorption, showing that the observed signal is made-up of three main components: (i) X-ray emission, (ii) radiative capture γ-rays emission and (iii) Compton continuum in the high energy region of the spectrum. The component (i) is the most intense one and is present for both resonant and non-resonant neutron absorption, thus preventing its use for improving the S/B ratio of the measurement via energy discrimination. The component (ii) is a clear signature of the resonant neutron absorption, but it represents only a small fraction of the overall observed signal. The component (iii), induced by radiative capture prompt $\gamma^{'}$s, not fully absorbed in the detector, can contain, as in the case of ^{197}Au, a significant fraction of the overall resonance signal and could be used, in principle, for energy discrimination;

7. there is a clear experimental indication of a neutron energy independent detection efficiency in the RD configuration;

8. with an appropriate choice of energy discrimination it is possible to increase the S/B ratio of the measurements, with a reduction of the signal intensity. The improvement that can be obtained in the quality of the measurements depends on the sample under study and on the chosen analyser foil;

9. the measured neutron TOF spectra have shown that neutron resonances can be measured up to neutron energies of 200 eV;

10. the present experiment seems to suggest that an improvement can be expected by detecting higher energy $\gamma^{'}$s, say above 150-200 keV, due to the contribution of Compton scattering events;

11. the small dimension of these devices is a key characteristic for their inclusion in RD arrays, providing good spatial resolution for inclusion in RD arrays providing good spatial resolution for HINS measurements at small scattering angles;

12. a further improvement of S/B ratio can be achieved by selecting γ energy above the sensitivity threshold of CZT (above 250 keV)

YAP

The results obtained with YAP indicate that:

1. the YAP is effective for the RD configuration up to about 90 eV;

2. the use of γ energy thresholds (LLD) improves the S/B ratio;

3. above 400 keV LLD an impressive improvement of the S/B, and thus of signal counting efficiency, is achieved;

4. the YAP are good candidates for RD arrays for HINS measurements;

5. thicker crystal should increase efficiency but a detailed study of the neutron backscattering into the active medium is needed;

Chapter 5

DINS and HINS measurements on H_2O

In order to verify the performances of YAP scintillators and for a further demonstration of the reliability of these devices for the RD configuration, two different inelastic neutron scattering measurements have been performed on a H_2O molecular system: 1) a DINS experiment on VESUVIO on liquid bulk water below the critical point, 2) a HINS measurement on the VLAD prototype on Ice-Ih at T=270 K.

5.1 DINS measurements on liquid H_2O

From a physical point of view, the properties of water below and above the critical point have stimulated an increased interest relatively to the dynamical properties of this molecular system. Neutron diffraction studies [123] argued that the strong modifications undergone by the hydrogen bond network when the sub- and the supercritical conditions are approached, could be responsible

of the differences in the dynamical behaviour, and recent experimental works have been devoted to the investigation of proton dynamics in subcritical and supercritical conditions [124–127].

From an experimental point of view, the determination of the proton mean kinetic energy is directly obtained through DINS measurements within the framework of the impulse approximation (IA) (see Chapter 2), where from the experimental measurement of the double differential scattering cross section the intrinsic Compton profile $J(y)$ is obtained.

DINS measurements on a liquid H_2O sample at two different thermodynamic $[P, T]$ conditions, namely [1 bar,293 K] and [100 bar,423 K], have been performed on VESUVIO. Two different sample containers have been used: an aluminum (Al) sample container for [1 bar,293 K] measurements and a titanium-zirconium (TiZr) sample container for both [1 bar,293 K] and [100 bar,423 K] measurements.

Two different inverse geometry configurations have been employed in parallel, namely the RD and the RF.

In what follows the results obtained in the RD configuration will be presented in detail, while only the main RF results will be discussed for a comparison.

The RD measurements, despite explorative (only one YAP detector was available), are very important as they represent the first RD experiment on a water sample up to final neutron energy of about 70 eV [128]. On the other hand, the comparison of the RD results with the standard RF ones, gives a more precise indication of the real capability of this technique for a routine use on inverse geometry instrument for DINS experiments, accessing an extended region of final energies, where the standard detection techniques are not effective.

5.1.1 RD measurements

In the RD measurements a single YAP scintillator was coupled to a ^{238}U analyser foil. The YAP scintillator was a cylindrical crystal of 3.5 cm diameter and 6 mm thickness, while the analyser was a foil of (3.5 x 3.5) cm^2 area and 30 μm thickness. The electronic chain of the YAP$'$s detection system was set with a LLD threshold corresponding to about 50 keV photon energy.
In figure 5.1 a schematic layout of the whole experimental set up is shown. In

Figure 5.1: Experimental set up for the DINS experiment on liquid water on VESUVIO configured as a RF and RD spectrometer

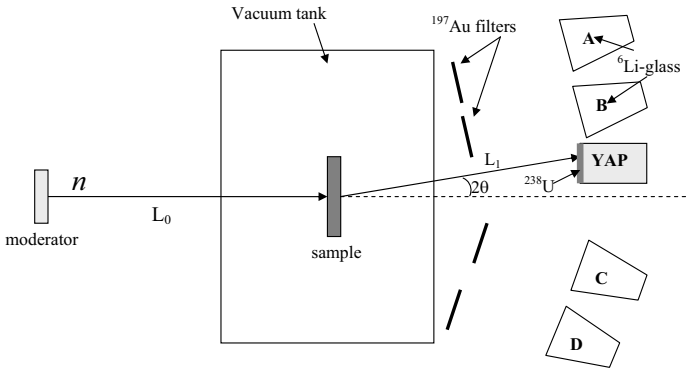

the figure n represents the incident neutron beam. The sample, placed inside the aluminum vacuum chamber, is at a distance $L_0 \simeq 11$ m from the water moderator. The ^{6}Li-glass detectors banks **A**, **B**, **C** and **D** contain in total 32 scintillating elements, each coupled to a photomultiplier tube, covering the angular interval 30°-70° circa. The average distance of the ^{6}Li-glass detectors from the sample is about 0.7 m, while the average distance of the ^{197}Au filters from the ^{6}Li-glass detectors is about 0.35 m. The YAP scintillator is placed

close to the ^{6}Li-glass detector bank at lowest scattering angle (**B** in fig. 5.1) at a distance $L_1 \simeq 0.7$ m from the sample position and at a scattering angle $\vartheta \simeq 27°$.

Figures 5.2, 5.3 and 5.4 show the normalised TOF spectra in the region 50-500 μs. Each pair of figures represents the scattering signal from sample container

Figure 5.2: DINS spectrum from empty (a) and full (b) Al sample container (T=293 K and p=1 bar)

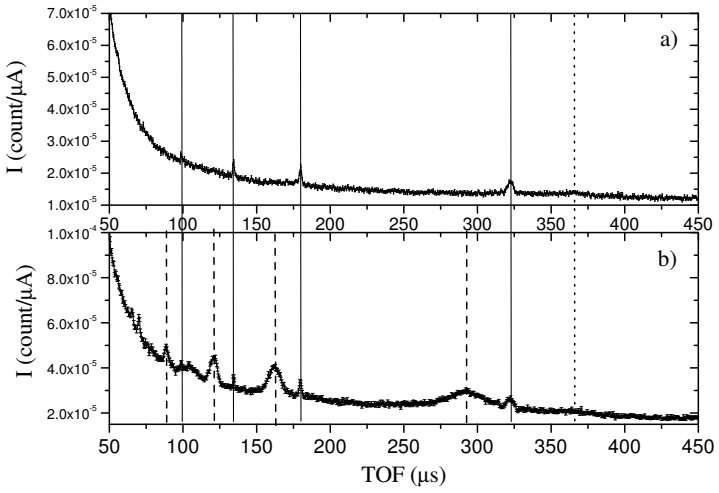

with H_2O inside (5.2(a), 5.3(a), 5.4(a)) and without (5.2(b), 5.3(b), 5.4(b)). An anomalous behavior around 70 μs can be noticed TOF spectra in figs. 5.3(b) and 5.4(b) as compared to the TOF spectrum in fig.5.2(b). This unphysical feature is most likely induced by dead time losses mechanisms, due to the enhancement of the count rate after the insertion of the H_2O sample into the TiZr sample container. In all spectra shown in figs. 5.2, 5.3 and 5.4 the structures marked by continuous lines, placed at about 320 μs, 180 μs, 120 μs and 100 μs indicate the recoil peaks of the sample container, corresponding to

Figure 5.3: DINS spectrum from empty (a) and full (b) TiZr sample container (T=293 K and p=1 bar)

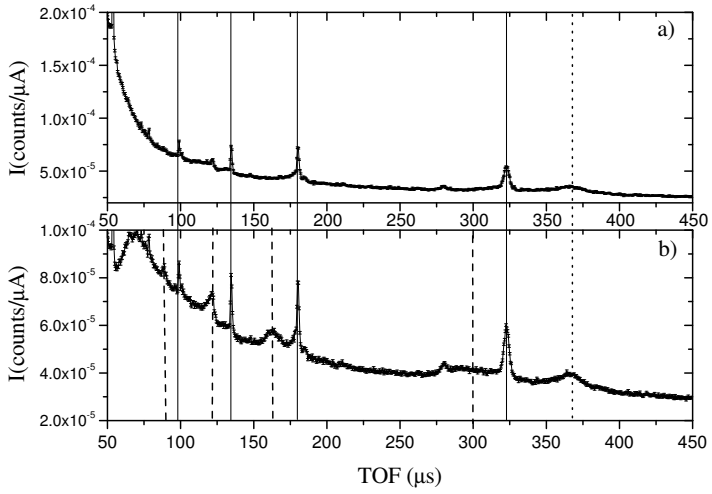

final neutron energies equal to the four ^{238}U resonances listed in tab. 3.2. The dashed lines at time positions of about 290 μs, 160 μs, 124 μs and 90 μs, are the H recoil peaks corresponding to the same final neutron energies. The dotted line indicates a broad peak, centered at about 365 μs, which is identified as the Al (TiZr) sample container recoil peak, corresponding to a final neutron energy of 4.906 eV, *i.e.* the ^{197}Au resonance (in fig. 5.2 this broad peak is less evident as compared to those in figs. 5.3 and 5.4 because of the lower scattering power of the Al sample container). This assumption is justified by the time difference, Δt, which is found between the sample container recoil peak recorded by the ^{6}Li-glass detector close to the YAP and the broad peak at 365 μs in the RD spectra. In figure 5.5 the RF (top) and RD (bottom) non-normalised spectra for the empty TiZr sample container are shown in the time region 330 μs - 400 μs. As it can be noticed, the time difference between

Figure 5.4: DINS spectrum from empty (a) and full (b) TiZr sample container (T=423 K and p=100 bar)

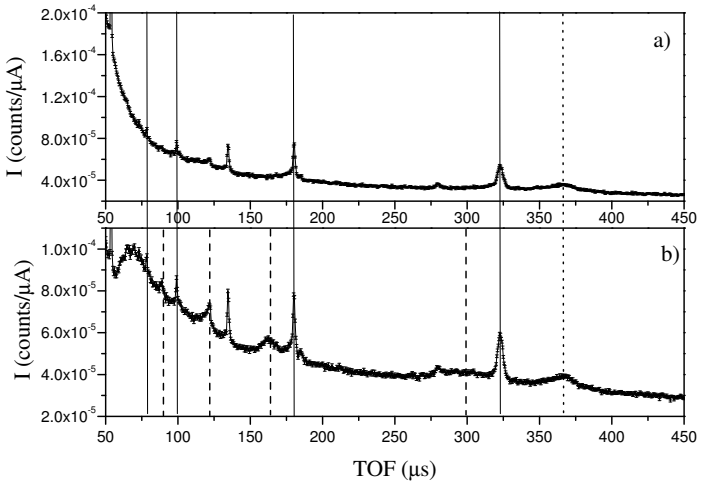

the dip and the peak (both indicated by a dashed line) is about 12 μs. This time difference corresponds to the time a 4.906 eV neutron takes to travel about 0.35 m, *i.e.* the distance between ^{197}Au filters and ^{6}Li-glass detectors. The time a photon takes to travel the distance between ^{197}Au filters and YAP (0.4 m circa) is about 1.2 ns which is not appreciable with the time bin employed for the time sampling of the signal (δt= 500 ns). Figure 5.6 shows the RF and RD non-normalised TOF spectra relative to H_2O in the Al sample container, in the time region 250 μs - 375 μs. The dip, centered at about 330 μs (fig. 5.6(b)), is related to the H recoil signal corresponding to 4.906 eV final neutron energy, while the peak at about 290 μs (fig. 5.6(a)) is the H recoil signal corresponding to 6.671 eV final neutron energy. The dashed lines indicate the time region where the two signals overlap. It can be hypothesised that the radiative capture γ's produced by neutron absorption in the ^{197}Au

Figure 5.5: TOF spectra in the 130-400 μs from empty TiZr sample container acquired by the YAP (lower) and the closest ^{6}Li-glass detector (upper).

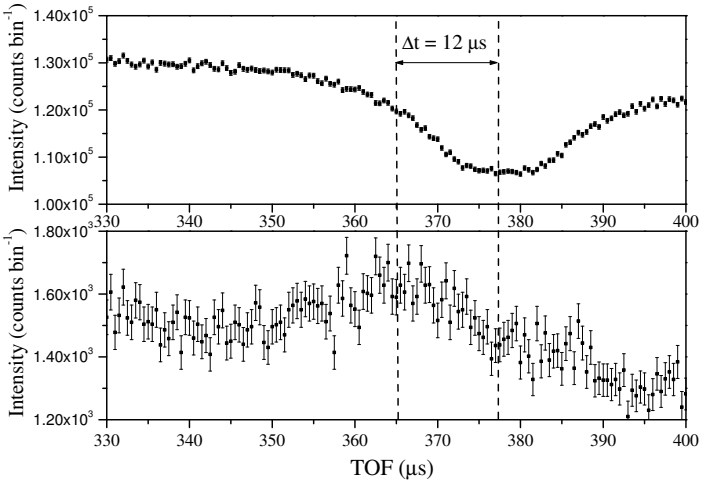

filter could contaminate the H recoil signal measurement through the RD in the overlapping TOF region.

Figure 5.7 shows the TOF spectrum obtained subtracting the two spectra in fig. 5.2. The sample dependent background in fig. 5.7 has been fitted in the whole TOF range, excluding the peak regions. Figure 5.8 shows the background corrected TOF spectrum, relative to fig. 5.7. The same procedure has been applied to the other spectra but the results are not shown. It has to be noticed that in the case of figs. 5.3 and 5.4, together with the recoil peaks of sample container and H_2O , spurious peaks due to (n,γ) resonance reactions in the sample container itself are found. Figure 5.9 represents a blow up of the TOF spectra for TiZr sample container (room temperature) in the time interval 100 μs - 350 μs. The (n,γ) peak γ_1, placed at about 285 μs, is superimposed to the H recoil peak and it is not completely subtracted in the

Figure 5.6: TOF spectra from H_2O in the Al sample container acquired by YAP (upper) and the closest ^{6}Li-glass (lower). The dashed lines mark the region where the radiative captureγ's from ^{197}Au could contaminate the H recoil spectrum acquired with YAP.

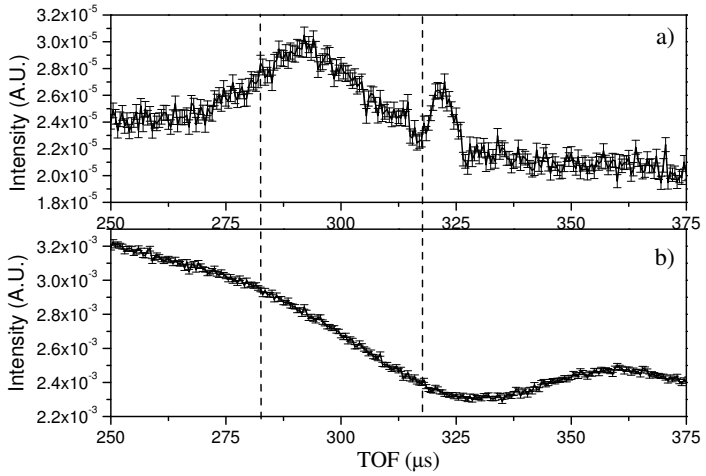

subtraction spectrum (the lowest spectrum on in fig. 5.9) spectrum. Thus it could contribute with a further unphysical broadening (together with the one discussed in fig. 5.5) to the intrinsic width of the H recoil peak. The spurious (n,γ) peaks γ_2, γ_3 and γ_4 are placed at about 170 μs, 150 μs and 125 μs respectively. As it can be noticed from fig. 5.9, the γ_2 peak is placed on the tail of the H recoil profile, the γ_3 is out of the H recoil region, while the γ_4 peak is within the width of the recoil peak. If $\rho_{\gamma,j}$ (j = 1,2,3,4) is the peak to background ratio for the j-th (n,γ) peak in the empty can spectrum, the values $\rho_{\gamma,1} = 0.13$, $\rho_{\gamma,2} = 0.04$ and $\rho_{\gamma,4} = 0.09$ are found. This means that the (n,γ) spurious contamination should be much more important for the first and third H recoil profiles rather than for the second one in the TiZr measurements.

Figure 5.7: subtraction TOF spectrum obtained with spectra in fig. 5.2

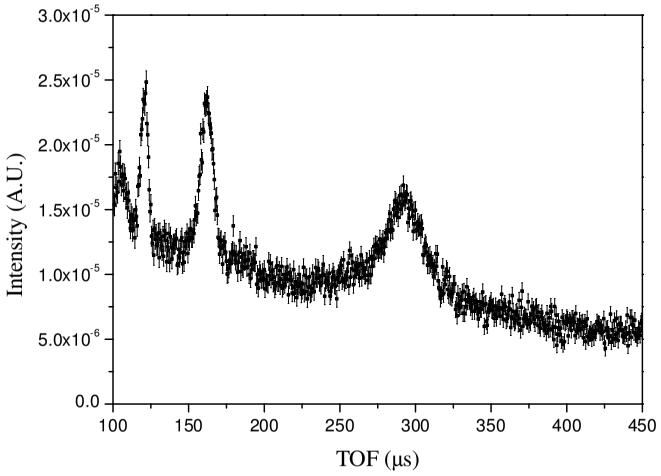

5.1.2 Calibrations

In order to extract the information on $n(p)$ and $\langle E_K \rangle$ from TOF spectra, a transformation which maps TOF into the y scaling variable has to be carried out. In order to do this, a calibration of the instrumental parameters has to be done. The only quantities which have been possible to calibrate are the secondary flight path, L_1, the time delay, t_0 and the scattering angle, ϑ, while for L_0 and E_i ($i = 1, 2, 3$ indexing the ^{238}U resonances in tab. 2.2) the values obtained by previous calibration measurements [115] have been considered. In what follows the calibration of t_0, L_1 and ϑ are briefly described, while in Table 5.1 the complete set of instrumental parameters is shown.

The total flight path $(L_0 + L_1)$ for the YAP detector can be determined form the time position of the free recoil peaks of the aluminum sample container. In facts for recoil scattering in the IA, the change in neutron velocity is deter-

Figure 5.8: Background corrected spectrum from spectrum in fig. 5.7

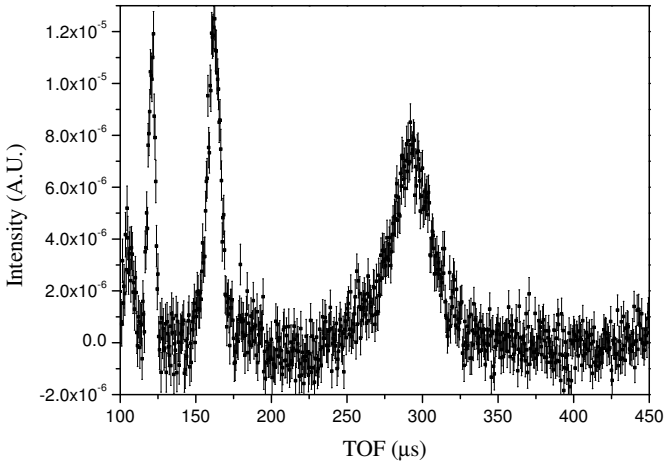

mined only by the conservation on kinetic energy and wavevector. Hence, the ratio of the final neutron velocity, v_1, to the initial neutron velocity, v_0, is a function of ϑ and of the atomic mass M and can be written as:

$$\frac{v_1}{v_0} = R(\vartheta) = \frac{\cos\vartheta + \sqrt{(\frac{M}{m})^2 - \sin^2\vartheta}}{\frac{M}{m} + 1} \tag{5.1}$$

while the time of flight equation is given by [115]:

$$t = t_0 + [L_0 R(\vartheta) + L_1]\frac{1}{v_1} \tag{5.2}$$

where t_0 is an electronic time delay.

By plotting the times of the recoil peaks of the Al sample container against $1/v_1$ and performing a least squares fit, the gradient obtained is $L_0R(\vartheta) + L_1$ while the y-intercept gives the time delay constant t_0. The fit procedure gives as final results L_1 = (68.5 ± 2.0) cm and t_0 = (-5.9 ± 0.3) μs.

The Pb diffraction pattern recorded by YAP (see fig. 5.10) with the ^{113}Cd

Figure 5.9: TOF spectra relative to H_2O in TiZr sample container (upper plot), empty TiZr sample container (middle plot) and subtraction spectrum (lower plot). Vertical lines indicate the peaks induced by the radiative capture $\gamma's$ from sample container and cryostat.

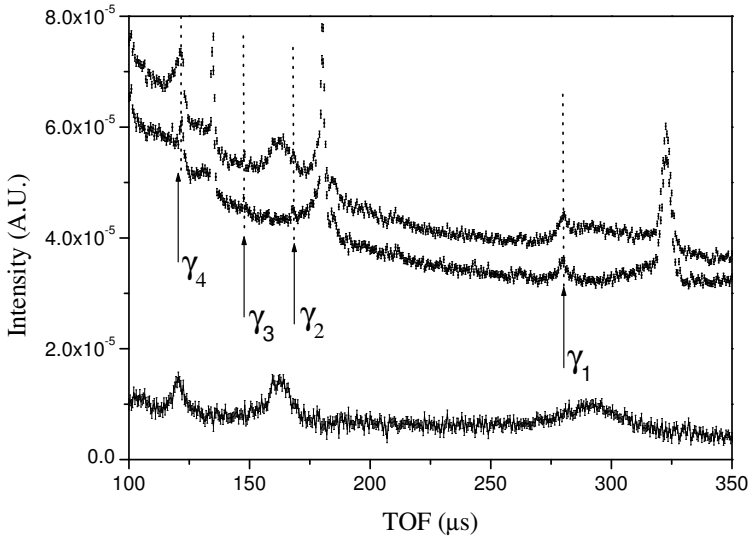

analyser foil (1 mm thickness) has been exploited for angle calibration. The ^{113}Cd has an intense radiative capture cross section for thermal neutrons up to about 400 meV and the prompt γ emission of ^{113}Cd is characterised by many lines of low relative intensity ($I_r \leq 0.01$) with the exception of the 558.5 keV line which has $I_r = 1$. Even if the absorption probability in the active medium of the YAP scintillator is of about 0.27 at this photon energy, the neutron counting is provided by the Compton continuum (at lower energies) also, due to the low LLD set for the measurements. From the time position of the diffraction peaks (see Figure 5.10) it is possible to calibrate the scattering angle, as described in the following. It is well known that the wavelength λ of

Table 5.1: List of the calibrated instrumental parameters

parameter	value
L_0	11.055 ± 0.021 m
L_1	0.685 ± 0.020 m
ϑ	26.7° ± 2.00°
t_0	-5.9 ± 0.3 μs
E_1	6.677 ± 0.053 eV
E_2	20.878 ± 0.095 eV
E_3	36.688 ± 0.142 eV

a neutron is related to its velocity by the de Broglie relation

$$\lambda = \frac{\hbar}{mv} \tag{5.3}$$

Bragg peaks are present in a spectrum recorded by a detector at a given angle ϑ if the Bragg relation is satisfied:

$$2d \sin \frac{\vartheta}{2} = n\lambda \tag{5.4}$$

Being elastic, Bragg scattering provides $v_0 = v_1 = v$ and from the time relation:

$$t - t_0 = \frac{L_0}{v_0} + \frac{L_1}{v_1} \tag{5.5}$$

we have

$$v = \frac{L_0 + L_1}{t - t_0} \tag{5.6}$$

and using equations (5.4) and (5.6), a relationship between the measured time of flight at which Bragg peaks from Pb (with known d-spacing) occur and the scattering angle can be obtained

$$2d \sin \frac{\vartheta}{2} = \frac{n\hbar(t - t_0)}{m(L_0 + L_1)} \tag{5.7}$$

Figure 5.10: Diffraction pattern of Pb acquired with YAP and a 1 mm thick cadmium analyser.

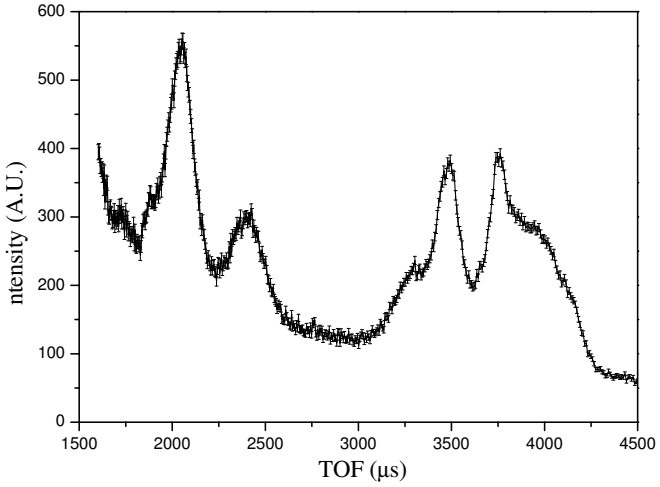

Thus by plotting the time positions of the Bragg peaks, shown in fig. 5.10, against d, and performing a least squares fit, the gradient obtained is proportional to $sin\frac{\vartheta}{2}$. The experimental points chosen for the fit are corresponding to the peaks located at 2403 μs, 2045 μs and 3491 μs as the last one, located at t=3750 μs, is heavily distorted by a possible non alinement of the analyser foil with the Debye cone. In Table 5.2 the values of time position of the Bragg peaks employed in the fit and the corresponding d-spacing are listed. This

Table 5.2: List of the time positions of the Bragg peaks of figure 5.10 and corresponding d-spacing for lead sample

t_p [μs]	d [Å]
2045	1.489
2403	1.750
3491	2.475

procedure provided a final value of ϑ=26.7° ± 2.00°. It has to be stressed that the overall calibration procedure envisages to use the determination of the L_1 from the flight path calibration as initialised parameter for angle calibration. The latter gives a determination of ϑ to be employed again in the fitting procedure for L_1. This iterative procedure has to be done until the convergence is reached. In our case the convergence was obtained after three iterations

5.1.3 Results

The transformation, mapping TOF recoil peaks onto $F(y)$ (see Chapter 2) provides a total of nine experimental response functions to analyse: six $F(y)$ for the room temperature sample and three for higher temperature one. Each group of spectra has been fitted simultaneously employing a Fortran code and a minimisation procedure based on the MINUIT package [129]. The fitting procedure envisages the use of a single $J(y)$ convoluted with the resolution functions relative to each analysed final energy. Thus the $F(y)$ can be formally written as:

$$F_i(y) = J(y) \otimes R_i(y) \ , \tag{5.8}$$

where $J(y)$ does not depend on the value of the index (i is the resonance index defined in Sect. 3.2), being the intrinsic Compton profile of the proton in the molecular system under study. The simplest form for $J(y)$ is the isotropic gaussian which can be written as:

$$J(y) = \frac{1}{\sqrt{2\pi}\sigma} \cdot \exp^{-\frac{y^2}{2\sigma^2}} \tag{5.9}$$

where σ is related to the man kinetic energy by the relation:

$$\langle E_K \rangle = \frac{3}{2m}\hbar^2\sigma^2 \tag{5.10}$$

In what follows the results obtained employing the gaussian model are presented [128].

H_2O at [1 bar, 293K]

At this thermodynamic condition there are six $F(y)$ to be fitted, three from Al and three from TiZr sample container. The simultaneous fit on the six $F(y)$, employing a simple gaussian $J(y)$, yielded the value $\sigma_y = (4.76 \pm 0.13)$ Å^{-1}, corresponding to $\langle E_K \rangle = (141 \pm 7)$ meV.

Another simultaneous fit has been done excluding two $F(y)$, namely the two $F_1(y)$ (one for Al and one for TiZr). This has been done in order to check the presence of possible spurious contamination induced, on the recoil peak considered, by the ^{197}Au radiative capture γ discussed in Section 5.1.1 (see Figure 5.6). The new fit yielded the value $\sigma_y = (4.42 \pm 0.18)$ Å^{-1}, corresponding to $\langle E_K \rangle = (122 \pm 10)$ meV. Figure 5.11(a)-(d) shows the four $F(y)$ at room temperature and the corresponding best fits obtained employing an isotropic gaussian $J(y)$.

H_2O at [100 bar, 423 K]

The fitting procedure on the three $F(y)$ at disposal for this thermodynamic condition yielded the value $\sigma_y = (5.60 \pm 0.2)$ Å^{-1}, corresponding to $\langle E_K \rangle = (195 \pm 14)$ meV.

Even in this case a new fit has been done excluding the $F_1(y)$. The final value obtained is $\sigma_y = (4.7 \pm 0.25)$ Å^{-1}, corresponding to $E_K = (137 \pm 16)$ meV. Figure 5.12(a)-(c) shows the experimental response functions and the corresponding best fits.

The higher relative uncertainty ($\frac{\Delta E_K}{E_K} = 0.12$) in the fit on [100 bar, 423 K]

data as compared to that on [1 bar, 293 K] data ($\frac{\Delta E_K}{E_K} = 0.08$) is due to the different overall number of experimental points employed in the fit in the two cases.

Figure 5.11: Experimental response functions, obtained from YAP for H_2O at room temperature and pressure, and corresponding fits obtained with an isotropic gaussian $J(y)$.

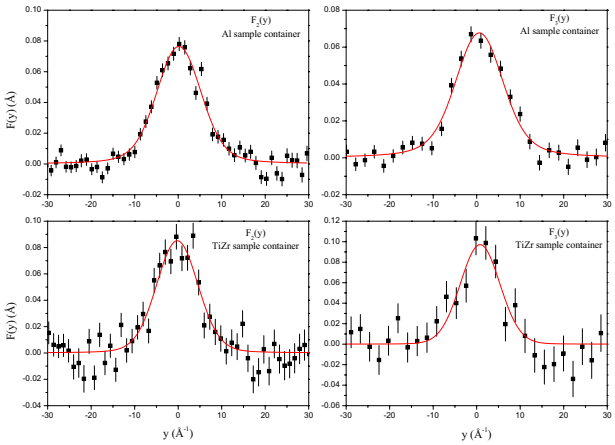

5.2 RF results

The DINS measurements in the RF configuration have been carried out employing the experimental set up shown in fig. 5.1. The data reduction and the calibration of the instrumental parameters have been performed employing the standard procedures which are well described elsewhere [115, 124, 126]. Figure 5.13 shows, as an example, the background corrected TOF spectrum acquired by means of the ^{6}Li-glass detector close to the YAP scintillator. The peak at $t \simeq 320$ μs represent the H free recoil signal for a scattered neutron energy of 4.906 eV (first ^{197}Au resonance). The TOF spectra have been trans-

Figure 5.12: Experimental response functions, obtained from YAP for H_2O at T=423 K and p=1 bar, and corresponding fits obtained with an isotropic gaussian $J(y)$.

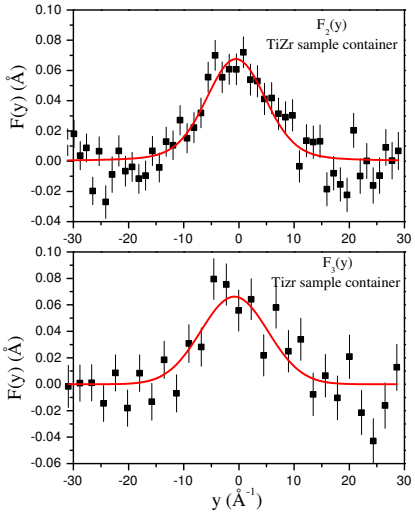

formed in the y space employing the same mapping procedure followed for the RD measurements, obtaining 32 experimental response functions (one per each detector). The ^{6}Li-glass detectors array is symmetric with respect to the neutron beam axis and hence the response functions of detectors at the same scattering angle have been summed, achieving better statistics. This procedure allowed obtaining a total of 16 $F(y)$ to be fitted employing the same code used for the RD spectra.

By employing an isotropic gaussian model, the fitting program on the RF data provided the values $\sigma_y = (4.46 \pm 0.05)$ Å^{-1}, corresponding to $\langle E_K \rangle = (124 \pm 3)$ meV, for the [1 bar, 293 K] data, and $\sigma_y = (4.55 \pm 0.08)$ Å^{-1}, corresponding to $\langle E_K \rangle = (129 \pm 5)$ meV, for the [100 bar, 423 K] ones. The smaller values of the errors associated to the RF determinations of $\langle E_K \rangle$ are due to

Figure 5.13: TOF spectrum acquired with a ^{6}Li-glass detector and ^{197}Au analyser filter at $\vartheta \simeq 31^{\circ}$ after subtraction of the background and of the sample-container signal.

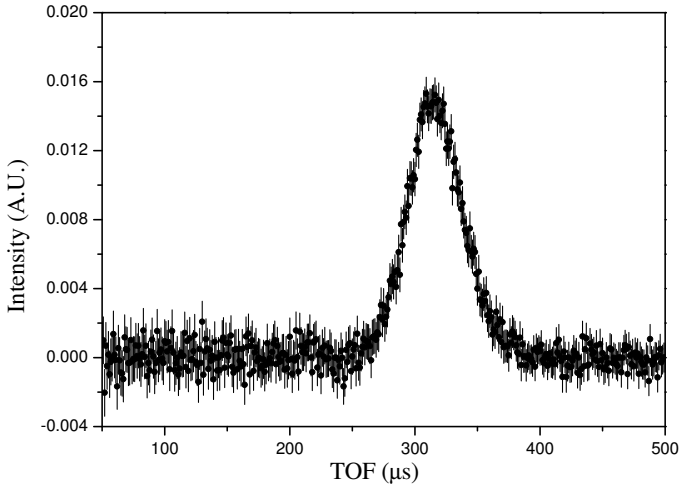

the better statistics as compared to RD measurements. In fact for the RD measurements a single YAP has been employed, while 32 ^{6}Li-glass detectors have been employed in the RF experiment. Furthermore the ^{197}Au filter foil has a peak value of radiative capture cross section which is about an order of magnitude higher than the 6.671 eV ^{238}U resonance, which is the most intense resonance considered in the RD analysis. Figure 5.14 shows the $F(y)$ and the fit are obtained employing an isotropic gaussian $J(y)$. By comparing the results obtained with the two different experimental configurations, summarised in Table 5.2, it can be seen that within the experimental errors, the $\langle E_K \rangle$ values are compatible.

Despite the noisy data, the results obtained through the RD configuration give

Figure 5.14: Experimental response function obtained summing over two ^{6}Li-glass detectors at the same scattering angle and corresponding fit obtained with an isotropic gaussian $J(y)$.

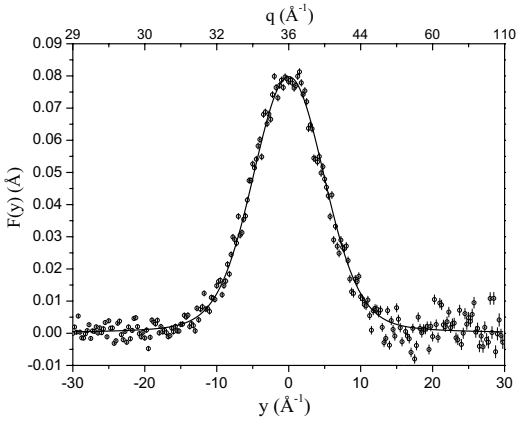

Table 5.3: Summary of the $\langle Ek \rangle$ values obtained through RD and RF measurements employing a simple gaussian fit

Sample	$\langle E_k^{\mathbf{RD}} \rangle$ [meV]	$\langle E_k^{\mathbf{RF}} \rangle$ [meV]
H_2O [1 bar, 293 K]	122 ± 10	124 ± 3
H_2O [100 bar, 423 K]	137 ± 16	129 ± 5

a further confirmation of the effectiveness of this set up for DINS experiment on light mass samples. In the perspective, the employment of RD arrays and the use of electronic thresholds on the γ energy to be revealed (see Chapter 4), would allow reaching higher efficiency, as compared to RF set up, thanks to a higher S/B ratio and no need of systematic *foil-out* measurements.

The experimental data collected in the RF configuration has been subject to a more complex analysis, employing an anisotropic and a model independent form for $J(y)$ [130]. In what follows only the final results of the analysis are

presented.

In recent papers [126, 131] it has been shown that for a free rotating quasi-symmetrical top molecule, such as H_2S in the gaseous state, the $n(p)$ can be well described, within the framework of the harmonic approximation, by an anisotropic gaussian where two different dynamics, one on the molecular plane ($x-y$ plane) with $\sigma_x = \sigma_y = \sigma(\widehat{t})$, the other one on the perpendicular direction ($\sigma_z = \sigma(\widehat{z})$), are considered. Referring to [126, 131] for a detailed description of the calculations, a spherical averaged $J(y)$ of the form:

$$J(y) = \frac{\hbar}{2} \cdot \int_{-1}^{1} d(cos\vartheta) \frac{(\frac{cos^2\vartheta}{\sigma^2(\widehat{z})} + \frac{sin^2\vartheta}{\sigma^2(\widehat{t})})^{-1}}{\sqrt{2\pi}\sigma^2(\widehat{t})\sigma^2(\widehat{z})} \exp[-\frac{y^2}{2}(\frac{cos^2\vartheta}{\sigma^2(\widehat{z})} + \frac{sin^2\vartheta}{\sigma^2(\widehat{t})})] \qquad (5.11)$$

can be written. This represent a more general form for the proton momentum distribution as compared to the simple gaussian which is the other hand, its natural limit. In this case the mean kinetic energy is given by the relation:

$$\langle E_K \rangle_H = \frac{\hbar^2}{2m_H} \left(2\sigma^2(\widehat{t}) + \sigma^2(\widehat{z})\right) \qquad (5.12)$$

Since the mass distribution in the H_2O molecule is less symmetric than in H_2S, an anisotropic momentum distribution could be expected for this system as well. This approach has already been employed in previous measurements on both supercritical liquid H_2O and H_2S (in the liquid and solid state) molecular systems [124, 126] where anisotropic proton momentum distributions were recognised. The physical motivations and the employed techniques are thoroughly reported in [126, 131].

The employment of an anisotropic gaussian model to fit the data, yielded, for the low temperature data, the values $\sigma_z = (6.72 \pm 0.2)$ Å^{-1}and $\sigma_t = (3.60 \pm 0.1)$ Å^{-1}, corresponding to $\langle E_K \rangle = (147 \pm 8)$ meV. For the higher temperature data the values $\sigma_z = (6.82 \pm 0.3)$ Å^{-1}and $\sigma_t = (5.60 \pm 0.20)$ Å^{-1}, corresponding to

$\langle E_K \rangle = (156 \pm 12)$ meV, are obtained.

A further analysis has been carried out with a model independent approach. From a theoretical point of view, it can be shown [132] that for $J(y)$ a general series expansion can be used, namely the Gram-Charlier series, involving Hermite polynomials, $H_n(x)$. In the case of a liquid, where the average wave vector distribution has not angular dependence, the general expression can be written in the form:

$$J(y) = \frac{e^{-\frac{y^2}{2\sigma^2}}}{\sqrt{2\pi\sigma^2}} \sum_n \frac{a_n}{2^{2n} n!} H_{2n}(\frac{y}{\sqrt{2}\sigma}) \tag{5.13}$$

This writing represents a general expansion of a symmetric momentum distribution. Anyway both symmetric and antisymmetric components, describing final state effects, can be incorporated by properly inserting both $H_2(\frac{y}{\sqrt{2}\sigma})$ and $H_3(\frac{y}{\sqrt{2}\sigma})$ polynomials.

In a recent paper [127] this approach has been employed for lineshape analysis of the proton momentum distribution in liquid and solid water in bulk and confined geometry, above and below the critical point.

In order to fit the experimental data employing a model independent approach, a proper Fortran code has been developed. In a first step, this code calculates the resolution function of each detector (hence for each scattering angle) in the y space, convoluting a gaussian function with a lorentzian lineshape:

$$V(y) = G(y) \otimes L(y) \ , \tag{5.14}$$

where $G(y)$ is

$$G(y) = G_{geom}(y) \otimes G_{Dop}(y) \ , \tag{5.15}$$

i.e. the convolution of the geometrical component of the spectrometer$'$s resolution function with the Doppler broadening of the nuclear resonance lineshape.

The $L(y)$ function in eq. (5.14) is the pure lorentzian lineshape of the nuclear resonance (see eq. (2.17)).

In a second step the obtained resolution functions are convoluted with the $J(y)$ quoted in eq. (5.13) and fitted to the experimental data employing a minimisation procedure which relies upon the use of the MINUIT package [129].

Employing the model independent approach, the fitting program yielded σ= (4.79 ± 0.05) Å^{-1}, corresponding to $\langle E_K \rangle$= (144 ± 3) meV for the lower temperature data. The same approach for the higher temperature data yielded the value σ= (4.98 ± 0.08) Å^{-1}, corresponding to $\langle E_K \rangle$= (156 ± 5) meV.

These results obtained with the two different approaches are in good agreement, within the errors, and well compare to those obtained by Reiter et. al [127] on liquid water at room temperature, where $\langle E_K \rangle$ = 146 is found employing a model independent approach, making use of a different fitting procedure. In Figure 5.15 the $\langle E_K \rangle$ values obtained with different forms are plotted. The results obtained analysing the RD measurements, employing the gaussian model, are also shown for a comparison. The $\langle E_K \rangle$ values for supercritical and subcritical H_2O, from two different experimental works [124, 127], are also plotted as a reference. The experimental value for the supercritical H_2O (T≃673 K and p≃360 bar) is $\langle E_K \rangle$=(178 ± 11) meV.

Data analysis on RF data should be completed, by considering the Double Difference measurements, for a more detailed and thorough interpretation of the results which, being still subject to a scientific debate, are not discussed in this dissertation.

Figure 5.15: Summary of the $\langle E_K \rangle$ values as a function of the temperature, obtained from data analysis on subcritical H_2O data employing different forms of $J(y)$ (see text for details). The dashed line is a guide for the eye for the $\langle Ek \rangle$ values calculated in the harmonic approximation

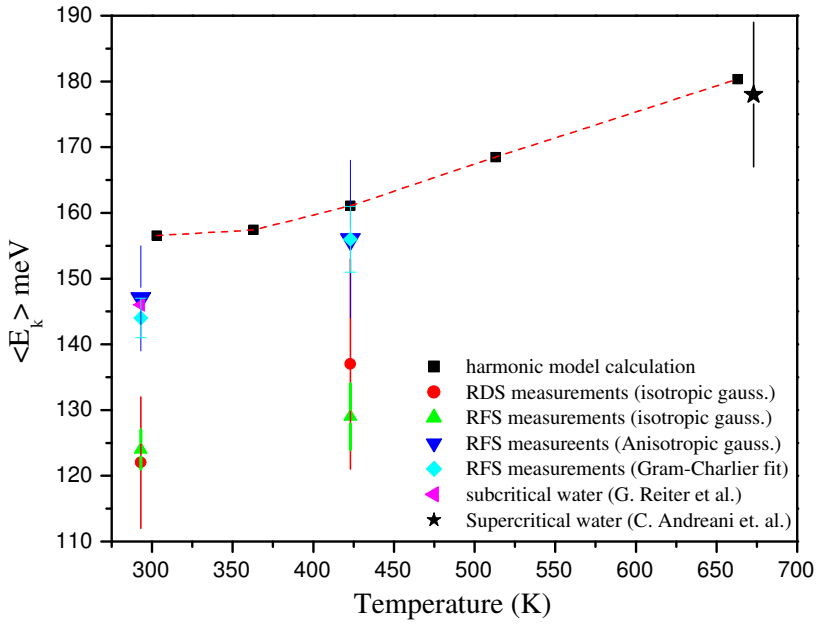

5.3 HINS measurements on polycrystalline Ice-Ih

In order to demonstrate the feasibility of HINS measurements on VESUVIO, the first experiment performed on the VLAD prototype was devoted to the measurement of the *O-H* stretching mode density of states in polycrystalline Ice-Ih at T=270 K and p=1 bar.

From a physical point of view, Ice-Ih is extremely interesting since it might be considered as a prototype for system showing ice disorder. The complex structural features could affect the internal modes of water molecules in Ice,

and in particular the O-H stretching. It is worthwhile mentioning that, from an experimental point of view, the possibility of deducing a good density of states $g(\omega)$ from neutron scattering measurements is strongly connected to the availability of the scattering function at low momentum transfers. This implies, as already stressed Chapter 2, high incoming and final neutron energies coupled to small scattering angle.

The O-H stretching mode density of states in polycrystalline Ice-Ih has already been measured, through inelastic neutron scattering, by Andreani et al. [95] on the direct geometry high resolution medium energy chopper spectrometer (HRMECS) at Argonne, while other authors measured $S(q, \omega)$ and $g(\omega)$ of Ice-Ih at different thermodynamical conditions [133, 134]. Thus Ice-Ih has been considered a suitable benchmark sample for HINS measurements by means of the VLAD equipment.

Beyond the scientific interest, this test in very important in order to demonstrate the reliability of the new equipment, and of the RD detection system, in accessing lower q values as compared to direct geometry reproducing the same findings of the previous measurements in Ref. [95] which, as a matter of fact, have been considered as a reference term for this experiment. Furthermore this measurement is another important demonstration of the effectiveness of the RD configuration in accessing unexplored kinematical regions in electron Volt neutron spectroscopy.

The main goal of this experiment is mostly related to the instrumental performances [135] and hence the main results are presented while a detailed description of data analysis can be found in a dedicated experimental paper [136].

Before discussing the experimental results a description of the experimental apparatus, namely the VLAD bank, is presented in the next section.

5.4 The Very Low Angle Detector bank (VLAD)

The Very Low Angle Detector (VLAD) bank has been designed and constructed in order to perform inelastic neutron scattering measurements at high-ω ($\omega \geq 0.3$ eV) and low-q ($q \leq 10$ Å^{-1}). This kinematical region defines the high energy inelastic neutron scattering (HINS) regime [17], which would allow experimental studies in areas such as the high energy electronic excitations in magnetic systems, rare earths ions, semiconductors and insulators, or high lying molecular rotational-vibrational states, molecular electronic excitations and the electronic level in solids [18–21] (see Sect.2.5.2)

A prototype of the VLAD equipment has been mounted in 2003 on VESUVIO spectrometer and has been tested through the HINS measurements presented in the next section.

In Table 5.4 the main instrumental parameters for VLAD are listed.

Thanks to the results obtained with YAP scintillators discussed in Sections

Table 5.4: Main instrumental parameters of VLAD

Geometry configuration	Inverse
Energy analysis	Resonance Detector
L_0	11.055
L_1	$\sim$ 2.0 m
Angular range	1°-5°
(q,ω) range accessed	$q \leq 10$ Å^{-1}, $\omega \geq 0.3$ eV

4.5-4.7 and 5.1, it has been decided the employment of these scintillators on VLAD. The use of YAP detectors at small scattering angles required the modification of the VESUVIO spectrometer.

In fact a series of calculations, taking into account the size of the neutron spot at the sample position and the beam divergence, have been done in order

to compute the angular range accessible with the original VESUVIO′s layout (see fig.2.6). These calculations indicated that in order to access the due kinematical conditions for HINS and to avoid the interception of the transmitted neutron beam with the detectors, a secondary flight path of 2 m and scattering angles in the range above 1° were to be considered. Figure 5.16 shows a contour plot of iso-angular loci, calculated with a flight path $L_1 =$ 2 m, as a function of q and ω and for a final neutron energy of 20 eV. The region of the (q, ω) space accessed is characterised by $q \leq 10$ Å^{-1}and ω up to 3 eV, with scattering angles in the range 1°-6°. A longer scattering flight path,

Figure 5.16: Region of the (q, ω) kinematical space accessible on VESUVIO for a final neutron energy of 20 eV, $L_1 = 2$ m and scattering angles below 6°. The values of q and ω attainable are typical of the HINS regime

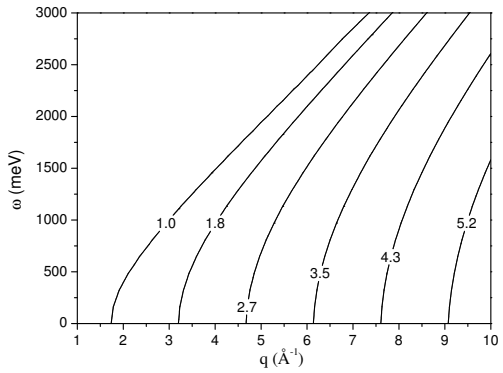

achievable only with a modification of the spectrometer′s experimental hall, despite allowing to achieve improved energy and angular resolutions, reduces the counting efficiency, due to the $1/L_1^2$ dependence of the scattered neutron beam intensity.

Thus considering the long scattering flight path and the small scattering an-

gles needed, a modification of the VESUVIO′s transmission beam pipe was envisaged. The new VESUVIO lay out is shown in Figure 5.17

Figure 5.17: Picture of the VLAD prototype equipment on VESUVIO

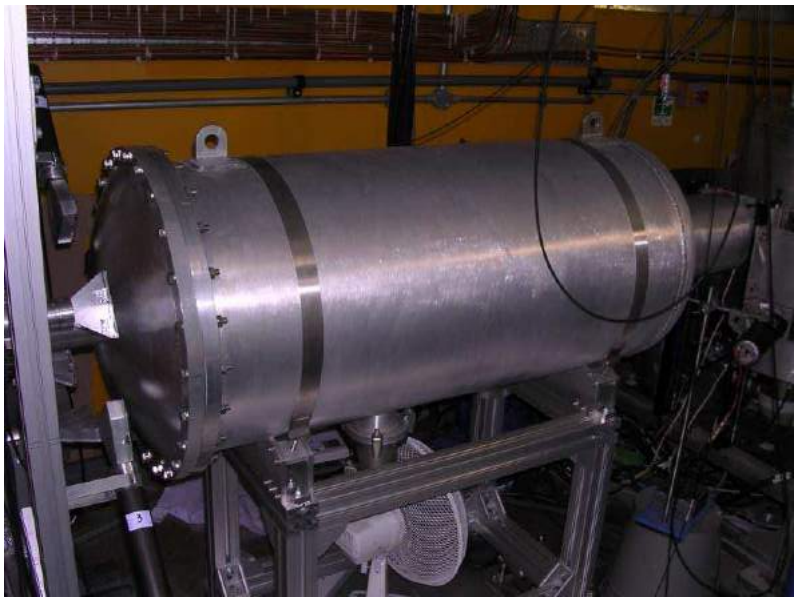

This configuration allows the scattered neutrons to travel in vacuo from the sample to the detector, thus avoiding possible scattering off light masses such as hydrogen, oxygen and nitrogen present in the air. Furthermore scattered neutrons do not traverse the beam pipe medium since the detector is reached. On the contrary, in the original lay-out neutrons scattered at small angles (about 1°) were likely to traverse long paths inside the beam pipe thickness, thus enhancing the probability of neutron scattering off aluminum. From a constructive point of view, the VLAD prototype is constituted of a cylindric aluminum vacuum chamber, connected by a bellow to the VESUVIO vacuum tank and, at the opposite side, to the transmitted beam pipe. At the end the VLAD chamber is closed by a spherical surface enforced by 6 thicker radii, this

solution allowing to have an Al window of only 2 mm thickness, still maintaining a high vacuum holding.

With the present beam collimation, the spanned angular range is $2° \leq \vartheta \leq 5°$, while the new collimation system will allow reducing the diameter of umbra+penumbra at the sample position (from the present 30 mm to about 23 mm) and the beam divergence. This will make possible placing the detectors, in the definitive equipment, at a minimum scattering angle of about 1° with the subsequent lowering of the lowest value of q attainable and improvement of the angular resolution.

The detector bank (leftmost side in fig.5.17) is composed by an aluminum frame for detector support and four Yttrium-Aluminum-Perovskite (YAP) detectors.

The YAP crystal (whose main characteristics have already been described in Chapter 4) have been designed in a trapezoidal form (see Figure 5.18) with 6 mm thickness and effective area of 1075 mm^2. The particular shape allows linking two crystal to form a single detector in order to cover a big area (thus enhancing the efficiency) in the same angular region as sketched in Figure 5.19. Beyond the scintillation medium there is a system of aluminum light guides, white painted inside, to insure good reflection for light collection onto the PMT.

A series of simulations with GEANT4 code [137] have been carried out in collaboration with the group of the university of Milano-Bicocca, in order to compute the performances of the YAP-based detection system on VLAD. These simulations aimed to compute detection efficiency and to study the effect of the cross-talk among detectors and neutron backscattering in the YAP's active medium [62]. The results of the simulations indicated a series of suitable

Figure 5.18: Picture of two YAP detectors

detectors arrangement for the final VLAD design.

Figures 5.20 and 5.21 show the possible detectors array configurations employed in the simulations. In fig.5.20 the possible configurations are: (top) four half rings lying on one plane, each covering a scattering angle interval of about 0.4°. Each half ring is made from 1.2 cm thick YAP crystals facing a 25 μm ^{238}U analyser; (middle) four complete rings arranged telescopically. The ^{238}U analysers are inserted in each ring between two layers of YAP scintillator in a sandwich arrangement. The lower drawing in fig. 5.21 represents the cross section view of the third detector ring (middle picture). A detailed discussion of the results is given in Ref. [62]

Figure 5.19: picture illustrating the angular coverage of a YAP crystal placed just beyond the VLAD vacuum chamber at two different angles

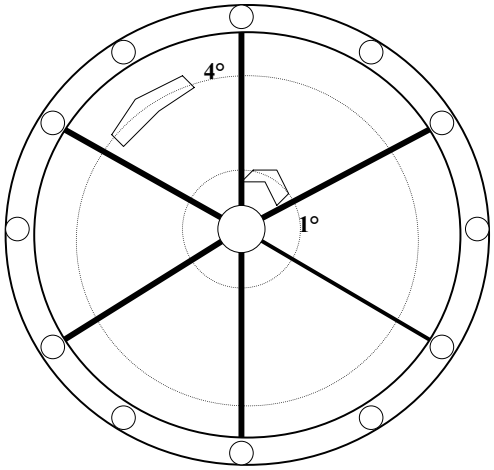

Figure 5.20: Geometry of different VLAD detectors arrays:(a) half rings, (b) telescopic arrangement of complete rings, (c) cross section view of the third detector ring in (b).

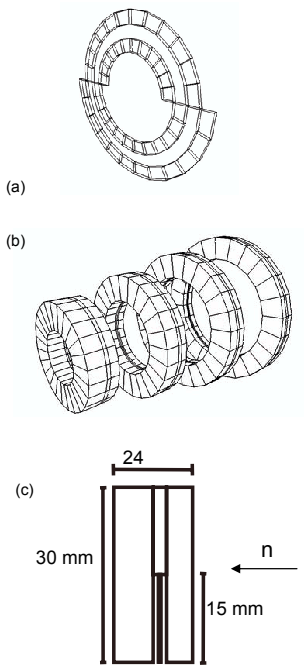

Figure 5.21: A different array′s configuration. The model is the same as in fig.5.20 but is made of half rings in order to reduce the cross-talk.

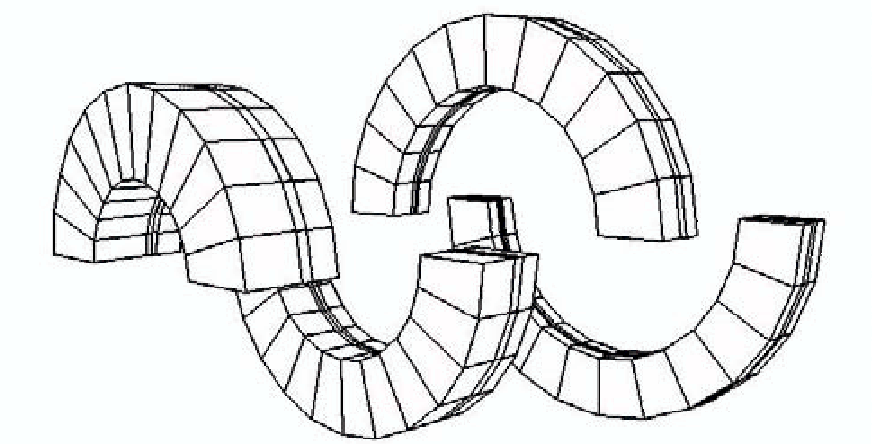

5.4.1 Experiment and results

The experimental set up for the HINS measurements on VLAD on a polycrystalline Ice-Ih sample is shown in Figure 5.22. During the tests, a suitable configuration was chosen with YAP detectors at 2°, 3.5° and 5°, in order to collect data on three different angular positions and thus different q, employing a LLD threshold of about 600 keV.

In figure 5.23 the TOF spectra from Ice-Ih in the aluminum sample container, at angular positions of 3.5° and 5°, are shown as examples. Subtracting the empty can spectra from the ones in fig.5.23 and correcting for the residual sample dependent background, the resulting signal spectra at the three scattering

Figure 5.22: Experimental set up for the HINS measurement on Ice-Ih on VLAD prototype.

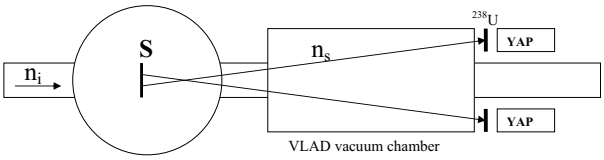

angles were transformed to obtain the absolute scattering function $S(q,\omega)$ with q varying in the range 2.5-5.5 Å^{-1}. This is shown in Figure 5.24 where the peak due to *O-H* stretching is visible on the righthand side of the main scattering peak (elastic peak). Following Ref. [95], $S(q,\omega)$ was further analysed, bearing in mind that in a polycrystalline samples it is related to the density of states $g(\omega)$ through its $q \to 0$ limit by:

$$g(\omega) = \lim_{q\to 0}[\frac{S(q,\omega)}{q^2} 2m_H\omega \frac{4\pi}{\sigma_{inc}} \frac{1}{n(\omega)+1}] \tag{5.16}$$

where $n(\omega)$ is the Bose population factor (≈ 1 for T =270 K) and σ_{inc} is the hydrogen incoherent scattering cross section. With the q values sufficiently close to zero, the shape of the $g(\omega)$ in the *O-H* stretching energy region, *i.e.* 350 meV $\leq \omega \leq$ 450 meV, was derived according to Equation (5.16). The resulting $g(\omega)$ values are shown in Figure 5.25. The integral in the stretching region under the $g(\omega)$ curve is:

$$\int_{350}^{450} g(\omega)d\omega = 9 \pm 2 \quad \frac{atoms}{cell} \tag{5.17}$$

This result well compares with previous measurements on the same system described in Ref. [95]. The peak position ($\approx$ 425 meV) is also well reproduced within the experimental error. The latter is due to both statistical uncertain-

Figure 5.23: TOF spectra from Ice-Ih obtained with YAP detectors at 3.5° and 5°

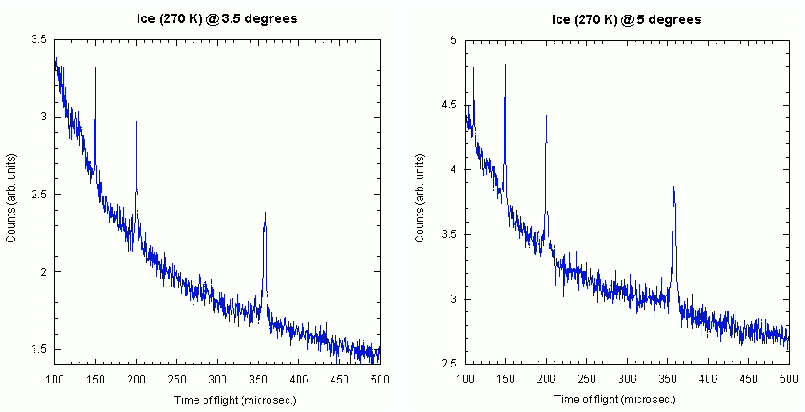

ties and to the instrumental resolution (mostly the energy component), which contributes to a large extent to the width of the $g(\omega)$ curve. The effect of the instrumental resolution can be accounted for by subtracting its contribution (full width at half maximum $\approx$ 70 meV) from a gaussian fit to the data (full line in Figure 5.25). The width of resulting gaussian function (dashed) is in good agreement with earlier measurements[20]. It should be noted that direct geometry (chopper) instruments have an energy resolution which is intrinsically better than inverse geometry instruments; however they are kinematically limited in energy loss to a maximum of about 1 eV, whereas inverse geometry instruments are kinematically unlimited. For a quantitative comparison, in Figure 5.26 the $g(\omega)$ obtained by Andreani et al. in Ref. [95] is shown. In that case the $g(\omega)$ is centered at about 417 meV, while the value of the integral in equation (5.17) is 8.1 atoms/cell, which is in good agreement with the result of the HINS experiment on VLAD. It has to be stressed that the HRMECS

Figure 5.24: $S(q, \omega)$ obtained from the TOF spectra at three different scattering angles.

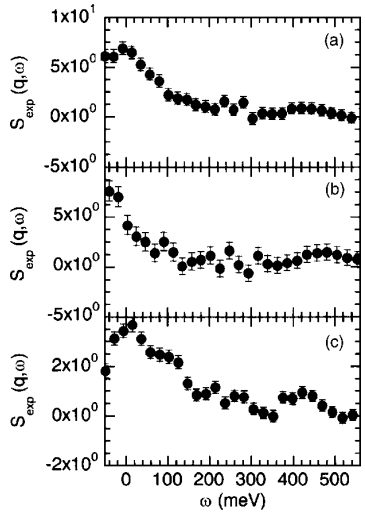

measurements accessed a lowest q value of about 4 Å^{-1}, while on VLAD the lowest value of q is about 2 Å^{-1}, thanks to the higher final (and thus initial) neutron energies accessed.

In summary, tests of the RD technique applied to HINS have demonstrated the feasibility of this kind of measurement on VESUVIO spectrometer and the good performances of the VLAD equipment despite in the prototype version. The results of the experiments on an Ice-Ih sample provide a benchmark for the HINS technique in the energy transfer range. The accessed kinematic region by HINS opens the way to a whole range of applications of the RD technique, including experimental investigations such as dispersion relations of high energy excitations in magnetic systems and rare earths ions, high lying molecular rotational-vibrational states, molecular electronic excitations, and

Figure 5.25: The $O-H$ stretching mode energy density of states in the range 300-550 meV. The peak is centered at about 425 meV. Dashed line is the $g(\omega)$ obtained deconvoluting a gaussian resolution function with 70 meV FWHM from the best fit (full line).

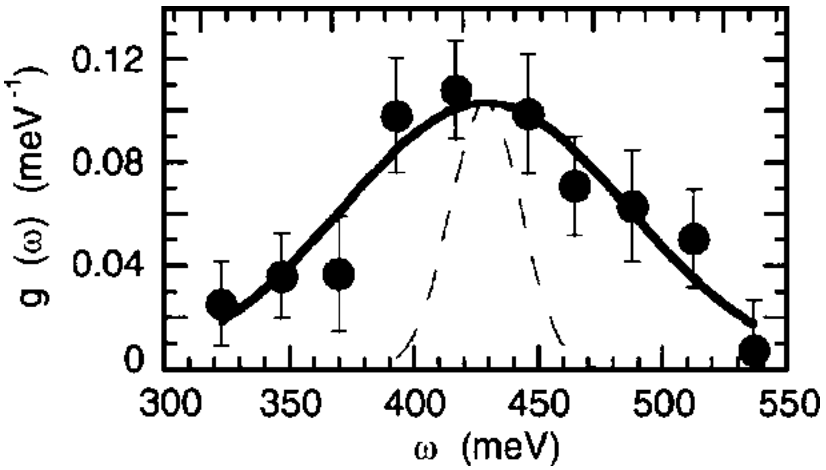

electronic levels in solids.

Figure 5.26: The $O-H$ stretching mode energy density of states from inelastic neutron scattering measurements on HRMECS at Argonne (Source: C. Andreani et al. [95]).

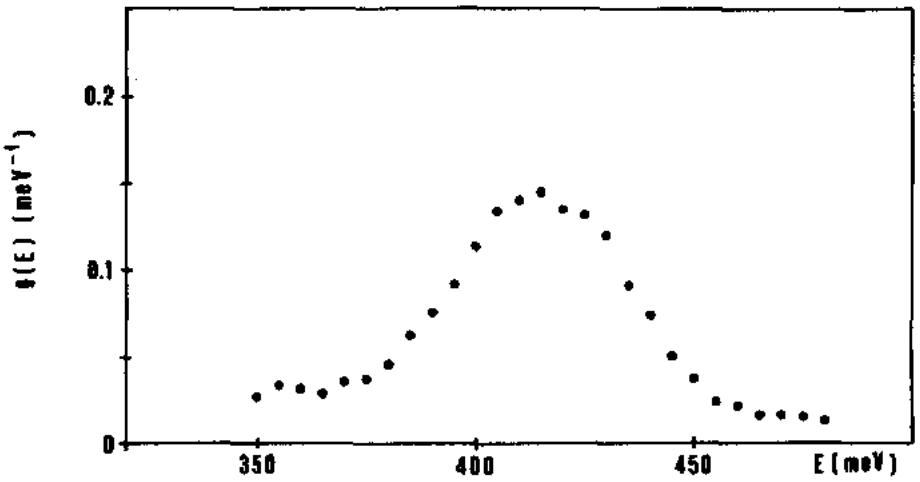

Chapter 6

Conclusions and perspectives

The experimental work presented in this dissertation has been devoted to research and development of neutron detectors capable of effectively operating in the 1-100 eV energy range on VESUVIO spectrometer, making feasible HINS measurements.
To this aim, the Resonance Detector (RD) configuration has been revised. In this configuration nuclear resonances are employed for final energy analysis and γ detectors for neutron counting.
The main results of my work can be summarised as follows:

- Selection of the best analysers for the RD configuration through a detailed study of their physical characteristics.
- Selection of the physical characteristics of different γ detectors (scintillators and semiconductors) to be employed in the RD configuration.
- First DINS experiment in the RD configuration on VESUVIO spectrometer, on a Pb sample and a $^4He - H_2$ mixture, including:

1- characterisation of the γ detector (a sodium iodide scintillator) with calibration sources;

2- characterisation and optimisation of the electronics;

3- choice of the analyser thickness for counting efficiency optimisation;

4- choice of the overall experimental set-up;

5- participation in the experiment, data analysis and upgrade of a Monte-Carlo code for simulation of DINS experiment in the RD configuration.

- Realisation of the first DINS experiment using Cadmium-Zinc-Telluride (CZT) semiconductor detectors, including:

  1- characterisation of the detectors with calibration sources;

  2- characterisation and optimisation of the electronics;

  3- participation in the experiment and data analysis;

- Realisation of biparametric measurements with CZT detectors, including:

  1- characterisation of the electronics;

  2- participation in the experiment and data analysis.

- Realisation of DINS and biparametric measurements with Yttrium-Aluminum-Perovskite (YAP) scintillators:

  1- characterisation of the electronics and of the detector;

  2- participation in the experiment and data analysis;

- Data analysis on DINS measurements on subcritical liquid H_2O performed in the RD and RF configuration:

1- development of a Fortran 77 code for data fitting employing a model independent approach;

- Design of the Very Low Angle Detector bank:
  1- study of feasibility;
  2- choice of the spectrometer$'$s configuration;
  3- choice of the proper detection system;

- Realisation of the first HINS measurement on VLAD prototype for the determination of the stretching mode energy density of states of polycrystalline Ice-Ih at 270 K.

From the obtained results, two applications of the RD can be envisaged on VESUVIO: 1) deep inelastic neutron scattering (DINS) measurements at high-q (above 20 Å^{-1}) and high-ω (above 1 eV); 2) high energy inelastic neutron scattering (HINS) at low-q (below 10 Å^{-1}) and high-ω (above 1 eV).
The demonstration of the effectiveness of the RD configuration for DINS and HINS relies upon a series of experiments on different scattering samples carried out on VESUVIO, where different analyser-γ detector combinations have been employed.
Results from the different experiments presented in this dissertation can be summarised as follows:

- The first DINS measurements on a Pb sample have been performed employing a $3" \times 3"$ sodium iodide (NaI) scintillator and ^{238}U analysers of

different thickness, detecting γ rays above 800 MeV. The large detection volume determines high background sensitivity, while the presence of neutron resonances in the active medium induces the use of heavy shielding around the detector.

From the experimental data the Compton profile $J(y)$ of lead has been measured, deriving the mean kinetic energy $\langle E_K \rangle$. This measurement has been done employing the Filter Difference and the Double Difference methods (DDM), obtaining in both cases good agreement with the expected values and demonstrating the reliability of the DDM for RD, with an appreciable reduction of the lorentzian tails of the overall spectrometer resolution function [53].

DINS measurements on a $^4He-H_2$ mixture have been performed obtaining clear indication of the effectiveness of the RD for light mass samples on VESUVIO.

- DINS experiments on Pb sample have been carried out with cadmium-zinc-telluride (CZT) semiconductor detectors and a ^{238}U analyser, detecting photon energies below 200 keV [55].

  These measurements have shown that these devices are effective up to final neutron energies of about 70 eV, insuring an improved S/B ratio as compared to previous measurements with NaI and to standard ^{6}Li-glass scintillation detectors. Furthermore the presence of ^{113}Cd in the active medium allows the detection of thermal neutrons through (n,γ) reactions in the detection active medium, so that DINS spectra and diffraction patterns can be acquired simultaneously with the same detection system.

Biparametric measurements allowed the characterisation of the detector response to prompt γ-ray emission from ^{197}Au and ^{238}U analysers, clearly recognising the signal components: 1) discrete γ-ray lines, 2) internal conversion X-ray lines, 3) Compton continuum from higher energy γ-rays which are detected with a partial release of their energy in the detector [56].

These measurements gave an experimental evidence of an almost neutron energy independent detection efficiency achieved with the RD configuration. The investigation of on- and off-resonance time of flight spectra, indicated that an appreciable improvement of the S/B ratio can be achieved employing discrimination thresholds above 250 keV.

- DINS measurements on Pb with a YAP scintillator have been performed employing standard and biparametric acquisition electronics. The first measurements shown that an impressive S/B ratio, as compared to CZT and ^{6}Li-glass detectors, is achieved employing a 600 keV discrimination threshold. The biparametric measurements allowed for the recognising that the main reason relies upon the suppression of the main background component, *i.e.* the 480 MeV γ-ray line provided by the ^{10}B shielding material of the experimental hall and of the beam dump [57].

- YAP scintillators have been employed for DINS measurements on liquid H_2O below the critical point and for HINS measurements on polycrystalline Ice-Ih on the prototype of the Very Low Angle Detector (VLAD) bank properly designed for HINS on VESUVIO spectrometer.

  DINS measurements in the RD configuration provided the first measure-

ment of proton dynamics employing this experimental set up, accessing about 70 eV final neutron energy [128]. The results compare well to those obtained with the standard RF configuration employing a gaussian momentum distribution. This experiment can be considered as a demonstration of the feasibility of DINS measurements on hydrogenated samples on VESUVIO employing the RD technique, accessing an extended final neutron energy range, where the standard RF configuration is ineffective.

HINS measurements on VLAD provided an experimental measurement of the $O-H$ stretching mode energy density of states accessing a region of the kinematical space characterised by $\omega \geq 350$ meV and $q \leq 6$ Å^{-1} [135]. The results compare well to those obtained in a previous experiment on the same sample on a direct geometry spectrometer.

Beyond the scientific interest of the measurement, the experiment aimed of demonstrating the effectiveness of the RD configuration and of the new instrumental equipment in accessing lower q values as compared to the previous measurements on direct geometry. This is a key issue because the effectiveness of the RD technique to extend the detectable final neutron energies up to 70-100 eV, will allow achieving higher ω values maintaining low q.

The obtained results on Ice-Ih motivated the purpose of new measurements which are planned for the near future:

- HINS measurements on a Praseodymium sample in order to identify the $^3H_4 \rightarrow ^4 G_1$ expected at about $\omega = 1.2$ eV.

- HINS measurements on diamond to observe the neutron induced inter-band transitions spectrum.

- HINS measurement on liquid H_2O in confined geometry, employing silica Xerogel matrices, in order to investigate the effect of the confining system on the $O-H$ stretching mode energy as compared to bulk water.

The big challenge for a breakthrough in electron Volt neutron spectroscopy is the improvement of the energy and of the angular resolutions. The first one is dominated by the width of the resonances employed for energy analysis (in the order of 80-100 meV in the best cases), while the angular resolution is mostly dominated by the detector size and neutron spot diameter at the sample position.

In the near future experimental tests will be devoted to finding a proper electronic set up for anti-coincidence measurements employing combinations of γ detectors and analysers with the aim to lower the width of the energy component of the resolution.

As far as the angular resolution is concerned, the new collimation system to be implemented on VLAD will reduce the neutron spot at the sample position, while the employment of CZT detectors in the inner annular array of VLAD bank would insure an appreciable space resolution.

Gas detectors at low pressure, such as resistive plate chambers (RPC), or at high pressures, such as compact xenon scintillators (HPXe), could provide improvement on angular resolution as well. A detailed study of the characteristics of these devices and the design of possible detector set up for future tests on VESUVIO is ongoing.

As a final comment it can be said that the large amount of experimental infor-

mation, acquired after four years of intense work on γ detectors, indicate that the RD configuration is very effective for neutron spectroscopy at electron Volt energies and that the experimental activity of high energy neutron detectors is of paramount importance for the development of high performances epithermal neutron spectrometers, which will operate on next generation spallation sources.

Bibliography

[1] S.W. Lovesey, *Theory of Neutron Scattering from Condensed Matter,* 3rd ed. (Oxford University Press) 1987.

[2] R. O. Simmons, Z. Naturforsch **48a** (1993) 415

[3] G.K. Ivanov and Y.S. Sayasov, Sov. Phys. Usp. **9** (1967) 670.

[4] P.C. Hoemberg and P.M. Platzman, Phys. Rev. **152** (1966) 198.

[5] G. Watson, J. Phys.: Condens. Matter **8** (1996) 5955; E. Pace, G. Salmè, G. West, Phys. Lett. **B273** (1991) 205.

[6] P.M. Platzman and N. Tzoar, Phys. Rev. **139** (1965), P. Eisenberger and P.M. Platzman Phys. Rev. **A2** (1970) 415; I.G. Kaplan, B. Barbiellini and A. Bansil, Phys. Rev. **B68** (2003)

[7] J.W. Dumond, Rev. Mod. Phys. **5** (1933) 1

[8] J.W. Dumond, Phys. Rev. **36** (1929) 643

[9] J-M. Gillet, P.J. Becker amd P. Cortona, Phys. Rev. **B63** (2001) 235115; R. Currat, P.D. DeCicco and R. Kaplow, Phys. Rev. **B3** (1971) 243.

[10] K.F. Berggren, F. Martino, P. Eisenberger and W.A. Reed, Phys. Rev. **B13** (1976) 2292; W.A. Reed and P. Eisenberger, Phys. Rev. **B6** (1972) 4596

[11] R. Hofstadter, H.R. Fechter and J.A. McIntyre, Phys. Rev. **91** (1953) 422;

[12] C. Ciofi degli Atti, D.B. Day, S Liuti, Phys. Rev. **C46** (1992) 1045; C. Ciofi degli Atti, E. Pace and G. Salmè, Phys. Rev. **C43** (1991) 1155; 235104.

[13] J. Heidmann, Phys. Rev. **80** (1950) 171

[14] J.M. Wilcox and B.J. Moyer, Phys. Rev. **99** (1975) 875; J.B. Cladis, W.N. Hess and B.J. Moyer, Phys. Rev. **87** (1952) 425;

[15] S.D. Drell, D.J. Levy, T.-M. Yan, Phys. Rev. **187** (1969) 2159; D.H. Perkins Rep. Prog. Phys. **40** (1977) 409; G.B. West Phys. Rep. **18c** (1975) 264;

[16] J.D. Bjorken and E.A. Paschos, Phys. Rev. **185** (1969) 1975; J.I. Friedman and H.W. Kendall, Ann. Rev. Nucl. Sci. **22** (1972) 203; R. Hofstadter, Ann. rev. Nucl. Sci. **7** (1957) 231

[17] C. Andreani, A. Pietropaolo, R. Senesi, G Gorini, M Tardocchi, N Rhodes, E M Schooneveld, A D′Angelo, *Condensed matter studies with 20-100 eV neutrons: effective detection systems for high inelastic neutron scattering and deep inelastic neutron scattering*, in **ISIS2003 Science Highlights**

[18] D. Richter Proc. of the 1984 Workshop on High Energy Excitations in Condensed Matter, Los Alamos, New Mexico Febraury 13-15 1984, pag. 559; J. Eckert *ibid.* pag 540

[19] J. Howard, *ibid* pag 548, P.A. Egelstaff *ibid* pag 626 and references therein;

[20] H.A. Mook *ibid* pag 226; M. Loewenhaupt *ibid* pag. 315 and references therein;

[21] J.F. Cooke, J.A. Blackman and T. Morgan *ibid* pag 401 and reference therein;

[22] A.D. Taylor, R.A. Robinson, P.A. Seeger, Nucl. Instr. Meth. **224** (1984) 133;

[23] S.K. Sinha, J. Appl. Phys. **50(3)** (1979) 1952

[24] J. Mayers, Phys. Rev. Lett. **84** (2000) 314;

[25] R. Senesi, C. Andreani, D. Colognesi, A. Cunsolo, M. Nardone, Phys. Rev. Lett. **86** (2001) 4584;

[26] C. Andreani, D. Colognesi, A. Filabozzi, M. Nardone, E. Pace, Physica **B234-236** (1997) 329; M. Celli, M. Zoppi, J. Mayers, Phys. Rev. **B58** (1998) 791;

[27] J. Mayers, C. Andreani, D. Colognesi, J. Phys. Cond. Matt. **9** (1997) 10639;

[28] C. Andreani, A. Filabozzi, E. Pace, Phys. Rev. **B51** (1994) 8854; L. Kosidowski, A.V. Powell, J. Mayers, Physica **B241-243** (1998) 335; D. Colognesi, A.J. Ramirez-Cuesta, M. Zoppi, R. Senesi, T. Abdul-Redah, Physica **B350** (2004) e983; E.B. Karlsson, T. Abdul-Redah, R.M.F. Streffer, B. Hjörvasson, J. Mayers, C.A. Chatzidimitriou-Dreisman, Phys. Rev. **B67** (2003) 184108

[29] G.F. Reiter, J. Mayers, J. Noreland, Phys. Rev. **B65** (2002) 104305

[30] A.C. Evans, J. Mayers,D.N. Timms and M.J. Cooper Z. Naturforsch A Phys. Sci. **A48** 425 (1993)

[31] R. Senesi, C.Andreani, Z. Bowden, D. Colognesi, E. Degiorgi. A.L. Fielding, J. Mayers, M. Nardone, J. Norris, M. Praitano, N.J. Rhodes, W.G. Stirling, J. Tomkinson, C. Uden, Physica **B276-278** (2000) 200.

[32] T. Abdul-Redah, C. Andreani, A. D'Angelo, G. Gorini, S. Imberti, J. Mayers, R.J. Newport, A. Pietropaolo, N.J. Rhodes, E.M. Schooneveld, R. Senesi, M. Tardocchi, J. Tomkinson, Physica **B350** (2004) e837

[33] L. Cser, N. Kroó, P. Pacher, V.G. Simkin and E.V. Vasilieva, Nucl. Instr. Meth. **179** (1981) 515

[34] R.N. Sinclair, M.C. Moxon and J.M. Carpenter, Bull. Am. Phys. Soc. **22** (1977) 101,

[35] D.R. Allen, E.W.J. Mitchell and R.N. Sinclair, J. Phys. E: Sci. Instr. **13** (1983) 639

[36] J.M. Carpenter, N. Watanabe, S. Ikeda, Y. Masuda, S. Sato and H. Rauh, Physica **B120**, (1983)126

[37] N. Watanabe, Proceedings of the 1984 Workshop on High Energy Excitations in Condensed Matter, Los Alamos Feb. 13-15, 1984. **LA-10227-C**, Vol 1.

[38] H. Rauh, N. Watanabe, Nucl. Instr. Meth. **228**, (1984) 147

[39] M.P. Paoli et al. ICANS VIII- Proceedings of the eighth Meeting of the International Collaboration on Advanced Neutron Sources, **RAL-85-110** Rutherford Appleton Laboratory (1985) 577

[40] R.K. Crowford CANS IX- Proceedings of the nineth Meeting of the International Collaboration on Advanced Neutron Sources, (1986) 397

[41] R.G. Johnson Nucl. Instr. Meth. **A163** (1985) 427

[42] H. Rauh and N. Watanabe, Nucl. Instr. Meth. **222** (1984) 507

[43] H. Rauh, S. Ikeda and N. Watanabe, Nucl. Instr. Meth. **224** (1984) 469

[44] C.D. Bowman and R.G. Johnson AIP Conference Proceedings N° 89 Neutron Scattering-1981 Ed. J. Faber, Jr.

[45] R.G. Johnson and C.D. Bowman Phys. Rev. Lett.**49** (1982) 797

[46] G.S. Samosvat, Y.S. Sayasov and V.T. Chuburkov, Sov. Phys. JETP **27** (1968) 15

[47] M.P. Paoli, R.S. Holt, J. Phys. C-Sol. St. Phys **21** (1988) 3633; R. S. Holt, L. M. Needham, M. P. Paoli, Phys. Lett. **A126** (1988) 373; E. Zukowski, L. Dobrzynski, M.J. Cooper, D.N. Timms, R.S. Holt, J. Latuszkievicz J. Phys. Cond. Mat. **2** (1980) 6315

[48] J. Mayers, A. Evans, A.D. Taylor, Proc. ICANS-XI, KEK report 90-25 (1991) 790; B. Rosi-Schwartz, J.A. Blackman, G.R. Mitchell, J. Mayers, Physica **B180 & 181** (1992) 729; J. Mayers, Phys. Rev. Lett **71** (1993) 1553;

[49] C. Andreani, A. Filabozzi, M.Nardone, F.P. Ricci, J. Mayers, Phys. Rev. **B50** (1994) 12744; S. Fulton, R.A. Cowley, A.C. Evans, J. Phys. Cond. Mat. **6** (1994) 2977; U. Bafile, M. Zoppi, F. Barocchi, R. Magli, J. Mayers, Phys. Rev. Lett. **75** (1995) 1957; R.T. Azuah, W.G. Stirling, J. Mayers, I.F. Bailey, P.E. Sokol, Phys. Rev. **B51** (1995) 6780

[50] F. Albergamo, M. Nardone, A. Filabozzi, Phys. Rev. **B56** (1997) 14614; J. Mayers, J. Low. Temp. Phys. **109** (1997) 153; A. Fielding, D. N. Timms, J. Mayers, Europhys. Lett. **44** (1998) 255

[51] A. Fielding, D.N. Timms, J. Mayers, Physica **B276-278** (2000) 69; C. Andreani, P. Cipriani, D. Colognesi, E. Pace, J. Phys. Cond. Matt. **12** (2000) 139; D. Nemirowski, R. Moreh, K.H. Andersen, J. Mayers, J. Phys. Cond. Matt. **12** (2000) 4293;

[52] J. Mayers, Phys. Rev. **B64** (2001) 224521; C.A.Chatzidimitriou-Dreisman, T. Abdul-Redah; R. Senesi, C. Andreani, D. Colognesi, J. Low. Temp. Phys. **126** (2002) 57; G.F Reiter, J. Mayers, P. Platzman, Phys. Rev. Lett. **89** (2002) 135505; D. Nemirovski, R.Moreh, K. Kaneko, T. Ohba, J. Mayers, Surf. Sci. **526** (2003) 282.

[53] C. Andreani, A. Pietropaolo, R. Senesi, G. Gorini, M. Tardocchi, A. Bracco, N. Rhodes, E. Schooneveld, Nucl. Instr. and Meth. **A481** (2002) 509

[54] A. Pietropaolo, C. Andreani, A. D′Angelo, R. Senesi, G. Gorini, S. Imberti, M. Tardocchi, N. Rhodes, E. M. Schooneveld, Appl. Phys. **A74** (2002) s189

[55] C. Andreani, A. D′Angelo, G. Gorini, S. Imberti, A. Pietropaolo, N. Rhodes,E. Schooneveld, R. Senesi, M. Tardocchi, Appl. Phys. **A78** (2003) 903;

[56] M. Tardocchi, A. Pietropaolo, C. Andreani, A. Bracco, A. D′Angelo, G. Gorini, S. Imberti, R. Senesi, N.J. Rhodes, E.M. Schooneveld, Nucl. Instr. Meth. **A526** (2004) 477

[57] M. Tardocchi and G. Gorini, A. Pietropaolo, C. Andreani and R. Senesi, N. Rhodes and E. M. Schooneveld, Rev. Sci. Instr. **75** (2004) 4880

[58] A. Pietropaolo, C. Andreani, A. D'Angelo, G. Gorini, S. Imberti, M. Tardocchi, N. Rhodes, E.M. Schooneveld, R. Senesi, Proceedings of the "Eleventh International Symposium on Capture Gamma-Ray spectroscopy and related Topics", World Scientific 555, (2003)

[59] A. Pietropaolo, R. Senesi, C. Andreani, G. Gorini,M. Tardocchi Proceedings of the XVI International Collaboration on Adavnced Neutron Sources, Dusserdorf-Neuss Germany, **Vol. I**, 223 (2003)

[60] M. Tardocchi , C. Andreani, O. Cremonesi, G. Gorini, E. Perelli-Cippo, A. Pietropaolo, N. Rhodes, E. Schooneveld, R. Senesi, Nucl. Phys. **B** (2004) to be published

[61] M. Tardocchi, A. Pietropaolo, R. Senesi, C. Andreani, G. Gorini, Nucl. Instr. Meth. **A518** (2004) 259

[62] E. Perelli-Cippo, G. Gorini, O. Cremonesi, M. Tadocchi, C. Andreani, A. Pietropaolo, R. Senesi, N.J. Rhodes, E.M. Schooneveld, IEEE Trans. Nucl. Sci. (2004) submitted for publication

[63] A. Pietropaolo, R. Senesi, M. Tardocchi, C. Andreani, G. Gorini, Physica **B350** (2004) e857

[64] M. Tardocchi, C. Arnaboldi, G. Gorini, S. Imberti, G. Pessina, E. Previtali, C. Andreani, A. Pietropaolo, R.Senesi, Physica **B350** (2004) e853

[65] G. Gorini, E. Perelli-Cippo, M. Tardocchi, C. Andreani, A. D'Angelo, A. Pietropaolo, R. Senesi, S. Imberti, A. Bracco, E. Previtali, G. Pessina, N.J. Rhodes, E.M. Schooneveld, Nucl. Instr. Meth. **A529** (2004) 293

[66] J.D. Jackson *"Elettrodinamica Classica"* Zanichelli Ed., 1984

[67] A.M. Weinberg and P.E. Wigner, *"The theory of neutron chain reactor"*, the Univ. of Chicago Press (1958)

[68] B.G. Harwey, *"Progress in nuclear physics"* Ed. O.R. Frisch, Pergamon Press (1959)

[69] R. Serber, Phys. Rev.**72** (1947) 1114

[70] V. Weisskopf, Phys. Rev.**52** (1937) 295

[71] L. Pienkowski et al. Phys. Letts. **B336** (1994) 147

[72] X. Ledoux et al. Phys. Rev. **C57** (1998) 2375

[73] M. Enke et al. Nucl. Phys. **A657** (1999) 317

[74] R.J. Newport, M.P. Paoli, V.T. Pugh, R.N. Sinclair, A.D. Taylor and W.G. Williams, ICANS VIII- Proceedings of the eighth Meeting of the International Collaboration on Advanced Neutron Sources, **RAL-85-110** Rutherford Appleton Laboratory (1985) 562

[75] P.A. Seeger, A.D. Taylor, R.M. Brugger, Nucl. Instr. and Meth. **A240** (1985) 98;

[76] C. Andreani, D. Colognei, E. Degiorgi, A. Filabozzi, M. Nardone, E. Pace, A. Pietropaolo, R. Senesi, Nucl. Instr. Meth. **A497** (2003) 535

[77] J. Mayers, J. Tomkinson, T. Abdul-Redah, W.G. Stirling, C. Andreani, R. Senesi, M. Nardone, D. Colognesi, E. Degiorgi, Physica **B350** (2004) e659

[78] R. Senesi, C. Andreani, A.L. Fielding, J. Mayers, W.G. Stirling, Phys. Rev. **B68** (2003) 214522;

[79] C.A. Dreismann, T. Abdul-Redah, R.M.F.Streffer, J. Mayers, Phys. Rev. Lett. **79** (1997) 2839.

[80] M. Celli, M.Zoppi, J. Mayers, Phys. Rev. **B58** (1998) 242.

[81] U. Bafile, M.Zoppi, F. Barocchi, R. Magli, J. Mayers, Phys. Rev. Lett. **75** (1995) 1957

[82] U. Bafile, M. Zoppi, F. Barocchi, R. Magli, J. Mayers, Phys. Rev. **B54** (1996) 11969.

[83] J. Mayers, C. Andreani, D. Colognesi, J. Phys.: Condens. Matter **9** (1997) 10639.

[84] P. Postorino, F. Fillaux, J. Mayers, J. Tomkinson, R.S. Holt, J. Chem. Phys. **94** (1992) 4411;

[85] F. Fillaux, M.H. Baron, J.Mayers, J. Tomkinson, Chem. Phys. Lett. **240** (1995) 114;

[86] A.C. Evans, J. Mayers, D.N. Timms, Phys. Rev. **B53** (1996) 3023.

[87] A.L. Fielding, D.N. Timms, A.C. Evans, J. Mayers,J. Phys.: Condens. Matter **8** (1996) 7205.

[88] C.J. Joachain *"Quantum collision theory"*, NORTH-HOLLAND Publishing Company, Amsterdam-New Yprk-Oxford

[89] J.M. Blatt, V.F. Weisskopf, *"Theoretical Nuclear Physics"*, Springer, New York, 1952.

[90] G. Breit and E. Wigner, Phys. Rev. **49** (1936) 519

[91] R. N. Silver and P. E. Sokol (eds) *Momentum Distributions* (Plenum Press, New York, 1989).

[92] G. F. Reiter, J. Mayers and J. Noreland, Phys. Rev. **B65**, 104305 (2002).

[93] G. B. West, Phys. Rev. **18** (1975) 263; E. Pace, G. Salme, G. West, Phys. Lett. **B273**

[94] C.G. Windsor, "*Pulsed Neutron Scattering*", Taylor Francis Ltd, 1981

[95] C. Andreani, P. Bosi, F. Sacchetti, C.K. Loong, J. Chem. Phys. **83**, 750 (1985)

[96] J.S. Scwinger, Phys. Rev. **51** (1937) 544

[97] O. Halpern and M.H. Johnson, Phys. Rev. **55** (1939) 898

[98] H. Ekstein, Phys. Rev. **76** (1949) 1328

[99] G.T. Trammel, Phys. Rev **92** (1953) 1387

[100] E. Balcar and S.W. Lovesey, J. Phys. **C19** (1986) 4605

[101] C. Stassis and H.W. Deckman, Phys. Rev. **B12** (1975) 1885

[102] L.L. Foldy, Phys. Rev. **87** (1952) 693

[103] A.D. Taylor, R. Osborn, K.A. McEwen, W.G. Stirling, Z.A. Bowden, W.G. Williams, E. Balcar, S.W. Lovesy, Phys. Rev. Lett. **61** (1988) 1309

[104] W.E. Lamb Jr., Phys. Rev. **55** (1939) 190

[105] M.S. Nelkin and D.E. Parks, Phys. Rev. **119** (1960) 1060

[106] R.E. Chrien, W.R. Kane, *Neutron Capture gamma ray spectroscopy*, Plenum Press 1979

[107] Y. Ryabov, J. Trochon, D. Schackleton and J. Frehaut, Nucl. Phys. **A216** (1973) 395;

[108] P. Poenitz, Z. Phys. **197** (1966) 262

[109] C.E. Porter and R.G. Thomas, Phys. Rev. **104** (1956) 483

[110] G.T. Ewan, J.W. Knowles and D.R. MacKenzie, Phys. Rev. **108** (1957) 1308; D. Deconninck and N. Longequeue, Phys. Rev. Lett **30** (1973) 863

[111] J.M. Cork, R.G. Shreffler and C.M. Fowler, Phys. Rev. **74** (1948) 240; C.Y. Fan, Phys. Rev. **87** (1952) 252

[112] H.I. Liou and R.E. Chrien, Nucl. Scie. Eng. **62** (1977) 463

[113] J.J. Blonstein, J. Dawidowski, J.R. Granada, Nucl. Instr. Meth. **B217** (2004) 333;

[114] S.F. Mughabghab, M. Divadeenam, N.E. Holden, *Neutron Cross Sections* Vol. I, Acedemic Press, New York (1981)

[115] A.L. Fielding, J. Mayers, Nucl. Instr. Meth. **A480**, 680 (2002)

[116] J. Mayers, A.L. Fielding, R. Senesi, Nucl. Instr. Meth. **A481** (2002) 454

[117] G.F. Knoll, *Radiation Detection and Measurements* (Wiley, New York 2000)

[118] SPIE Conf. Hard X-ray and Gamma-ray Detector Physics and Applications, July 1998 [Proc. SPIE 3446, 1 (1998)];

[119] B. Redus, *Charge Trapping in XR-100T-CZT Detectors*, Amptek Appl. Note ANCZT1, rev. 1 (2000);

[120] J.A. Bearden, Rev. Mod. Phys. **39** (1967) 78.

[121] M. Tardocchi, S. Conroy, G. Ericsson, J. Frenje, J. Kllne, and E. Traneus, Nucl. Instr. Meth. **A485**, 624 (2002);

[122] M. Tardocchi, *Background in the VESUVIO Experimental Hall: First Measurements with a Germanium Detector*, November 2002, Internal Report of Physics Department G. Occhialini, Milano-Bicocca University, Milan, Italy

[123] P. Postorino, R.H. Tromp, M.A. Ricci, A.K. Soper and G.W. Neilson, Nature (London) 366 (1993) 668

[124] C. Andreani, D. Colognesi, E. Degiorgi and M. A. Ricci, J. Chem. Phys. **115** (2001) 11243

[125] C.H. Uffindell, A.I. Kolesnikov, J-C. Li and J. Mayers, Phys. Rev. **B62** (2000) 5492; J.C. Li, A.I. Kolesnikov J. Mol. Liq. **100** (2002) 1

[126] C. Andreani, E. Degiorgi, R. Senesi, F. Cilloco, D. Colognesi, J. Mayers, M. Nardone, E. Pace, J. Chem. Phys. **114** (2001) 387

[127] G.F. Reiter, J.C. Li, J. Mayers, T. Abdul-Redah, P. Platzman, Bras. J. Phys. **34** (2004) 142.

[128] A. Pietropaolo, C. Andreani, A. Filabozzi, G. Gorini, N. Rhodes, R. Senesi, E. Schooneveld, M. Tardocchi, Nucl. Instr. Meth., submitted for publication

[129] F. James, *MINUIT minimisation package*: reference manual, CERN Program Library, Geneva, 199

[130] C. Andreani, S. Imberti, A. Pietropaolo, M.A. Ricci, R. Senesi, J. Chem. Phys., submitted for publication

[131] D. Colognesi, E. Degiorgi, E. Pace, Physica **B3-4** (2001)317

[132] V. F. Sears, Phys. Rev. **185** (1969) 200

[133] J.C. Li, J.Chem. Phys. **105** (1998) 6733

[134] D.D. Klug, C.A. Tulk, E.C. Svensson, C.K. Long, Phys. Rev. Lett. **83** (1999) 2584; A.I. Kolesnikov, J.C. Li, S.F. Parker, R.S. Eccleston, C.K. Long, Phys. Rev. **B59** (1999) 3569

[135] C. Andreani, G. Gorini, E. Perelli-Cippo, A. Pietropaolo, N.J.Rhodes, E.M. Schooneveld, R. Senesi, M. Tardocchi, Appl. Phys. Lett. **85** (2004) 5454;

[136] E. Perelli-Cippo, G. Gorini, M. Tardocchi, C. Andreani, A. Pietropaolo, R. Senesi, N.J. Rhodes, E.M. Schooneveld, Nucl. Instr. Meth. submitted for publication

[137] Agostinelli et al., Nucl. Instr. and Meth. **A506** (2003) 250